

METAL OXIDE-BASED PHOTOELECTROCHEMICAL CELLS FOR SOLAR  
ENERGY CONVERSION

Thesis by

Jordan E. Katz

In Partial Fulfillment of the Requirements

for the Degree of

Doctor of Philosophy

California Institute of Technology

Pasadena, CA

2008

(Defended October 19, 2007)

© 2008

Jordan E. Katz

All Rights Reserved

## ACKNOWLEDGMENTS

I don't think that it is possible to acknowledge fully and completely all the people I have interacted with and learned from while at Caltech or give them the thanks they truly deserve. Their contribution has simply been too great to express in a few brief paragraphs. But that is what I shall attempt to do nonetheless.

First and foremost I am very grateful for the opportunity to have worked with Professor Nathan Lewis. Nate is the person responsible for creating my interest in a subject about which I am nothing short of passionate: renewable energy. Not long after arriving at Caltech, I heard Nate's famous "energy talk." It inspired me the first time I heard it, and a dozen or so times later, it still does. It is largely in this context that I have written the following dissertation, and it has been the overarching theme of all my research at Caltech. In fact, I have no doubt that my future research in the field of chemistry will never be far from this theme. It is with the outstanding training I have received from Nate, as a scientist in general, and in the area of solar energy conversion in particular, that I hope to be able to make a meaningful contribution to solving the daunting problem of providing humanity with a clean, safe, low-cost, and abundant source of energy.

I would also like to thank another mentor, Dr. Bruce Brunshwig, who has been an instrumental part of nearly every aspect of my research here. Bruce spent countless hours working one-on-one with me, helping me to address any questions and problems I

had, and always with seemingly infinite patience. Bruce is extremely knowledgeable, easy to learn from, and he's quite simply a lot of fun to be around. He has been not only an excellent mentor to me, but also a good friend. I am deeply grateful for the considerable contribution he has made, both to my research and to my growth as a person.

Several other faculty members also deserve special mention. Professor Harry Gray is one of those people that makes me think to myself, "I want to be like *that* when I grow up!" I don't think I know anybody who is such an accomplished scientist and who is so easy and fun to be around. Every interaction with Harry I have ever had has been a pleasure. I am also grateful for the contributions from the other members of my committee, Professor Mitchio Okumura and Professor Jacqueline Barton, for their guidance and advice.

Most important in my day-to-day experience at Caltech has, of course, been the other members of the Lewis group. I owe a great deal of what I know about photoelectrochemistry to Dr. Florian Gstrein and Dr. David Michalak. All of the members of the Lewis Group have helped me with my work and contributed to me in countless ways, particularly Dr. Tom Hamann, Dr. Elizabeth Mayo, Dr. Matthew Traub, Tony Fitch, Josh Spurgeon, David Knapp, Don Walker, and Craig Wiggernhorn. Although it has only been a few months, it has also been my pleasure to get to know Elizabeth Santori, and I'm delighted that she's going to make sure my work on the mixed metal oxides project will continue after I leave. I owe a special thanks to James Maiolo who has not only been a terrific office-mate and a good friend, but who always seems to go out of his way to drop whatever he is doing to help me with whatever I ask of him.

Finally, it was with the amazing support of Sherry Feick and Nannette Pettis that I think anything worked around here at all! As far as I can tell, those two women are nothing short of saints!

I have also been lucky enough to work with several scientists not affiliated with Caltech. In particular, all of the femtosecond-resolved spectroscopy presented in Chapter 4 was done in close collaboration with Dr. Amanda Smeigh and Prof. James McCusker at Michigan State University. Also, I owe a great deal of thanks to Dr. Michael Woodhouse and Prof. Bruce Parkinson at Colorado State University, who freely shared many valuable secrets about the art of combinatorial printing and screening of metal oxides, saving us a great deal of time and effort learning the hard way.

I have also had the tremendous pleasure of being a mentor to Todd Gingrich who shares a large portion of the credit for the work described in Chapter 5. Working with Todd has been a fantastic experience in every way, and I have gotten at least ten times more out of it than I put in! We have had a lot of fun together, poking fun of each other and generally giving each other a hard time. I know the reason we get along so well is that our relationship is built on a very strong mutual respect for each other. I know that Todd is going to make a world-class scientist, and it's been my honor to contribute to him in what ways I could.

My experience at Caltech would have not been the same without the terrific staff, who consistently exceeded my expectations in every interaction I had with them. I am indebted to Dian Buchness, Anne Penney, Steven Gould, Lillian Kremar, Cora Carriedo, Joe Drew, and Laura Howe for all their help in making lots of things that *could* have been a colossal pain in the neck instead be easy and effortless. I especially thank the four

people without whose handiwork my research would not have worked at all: Mike Roy, Steve Olson, Tom Dunn, and Rick Gerhart. Mike, Steve, Rick, and Tom, aside from being incredibly talented at what they do, are just great people in every way. I've been blessed to have such competent people help me turn my naïve and shortsighted ideas into real working parts and instruments.

Of course, none of this would have been possible at all without the love and bottomless support of my family. Always there for me no matter what, my mom and dad are the best parents a kid could hope for. I couldn't have done it without you. My sister, Megan, is in no small part responsible for the person I am today — she has always been a guiding influence in my life. I would do anything for her.

Finally, I have saved the most important person for last. My wife Cécile has done as much for me as any person could ask for, and then done more. Her endless love and support has made all the difference. Whether it was making me dinner, giving me encouragement, or just being there for me, I can't imagine having done this without her. She deserves at least as much credit for this dissertation as I do, if only for having put up with me throughout the entire process! I can only say that I *do* know how lucky I am. Cécile, I love you with all my heart.

*If the Earth  
were only a few feet in  
diameter, floating a few feet above  
a field somewhere, people would come  
from everywhere to marvel at it. People would  
walk around it, marveling at its big pools of water,  
its little pools, and the water flowing between the pools.  
People would marvel at the bumps on it, and the holes in it, and  
they would marvel at the very thin layer of gas surrounding it and  
the water suspended in the gas. The people would marvel at all the  
creatures walking around the surface of the ball and at the creatures in  
the water. The people would declare it as sacred because it was the  
only one, and they would protect it so that it would not be hurt. The  
ball would be the greatest wonder known, and people would come  
to pray to it, to be healed, to gain knowledge, to know beauty,  
and to wonder how it could be. People would love it, and  
defend it with their lives because they would somehow  
know that their lives, their own roundness,  
would be nothing without it. If the  
Earth were only a few feet  
in diameter.*

*- Joe Miller*

## ABSTRACT

In order to address the need for CO<sub>2</sub>-free energy, recent trends in global CO<sub>2</sub> emissions and energy production are analyzed, and the photoelectrochemical properties of two types of metal oxide-based solar cells are presented.

The effects of potential-determining cations (Li<sup>+</sup>, H<sup>+</sup>) in the electrolyte of TiO<sub>2</sub>-based dye-sensitized solar cells, using Ru(H<sub>2</sub>L')<sub>2</sub>(NCS)<sub>2</sub>, where H<sub>2</sub>L' is 4,4'-dicarboxylic acid-2,2'-bipyridine, as a sensitizer was investigated using current density vs potential (*J-E*), spectrochronocoulometric, and spectroscopic methods. Photoelectrochemical cells with lower concentrations of the cations Li<sup>+</sup> and H<sup>+</sup> had increased open-circuit voltages (*V<sub>oc</sub>*), and decreased short-circuit current densities (*J<sub>sc</sub>*). Spectrochronocoulometric methods indicated that the energy of states in TiO<sub>2</sub> shifted by approximately -1 V when in contact with electrolytes lacking small cations. Spectral response measurements indicated that the loss of photocurrent was accompanied by a nearly monotonic drop in the external quantum yield across all wavelengths.

Transient absorption spectroscopy was used to measure the kinetics of interfacial electron transfer of the same system. No dependence was observed on the ultrafast dynamics of electron injection on cations used in ClO<sub>4</sub><sup>-</sup>-based solutions. However, in solutions of TBA<sup>+</sup> with I<sub>3</sub><sup>-</sup>/I<sup>-</sup>, femtosecond, but not picosecond, dynamics were observed. In contrast, for solutions with Li<sup>+</sup> and ClO<sub>4</sub><sup>-</sup>, I<sup>-</sup> or I/I<sub>3</sub><sup>-</sup>, both femtosecond and picosecond dynamics were observed. Nanosecond-resolved spectroscopy results show that the

absence of small cations did not affect the rate of recombination, while the regeneration rate of  $[\text{Ru}^{\text{III}}(\text{H}_2\text{L}')_2(\text{NCS})_2]^+$  was decreased. Results indicate that both the ground and excited state reduction potentials of the sensitizer shift as a function of small cations in solution, along with the energy of states in  $\text{TiO}_2$ . The efficiency of electron injection is thus largely unchanged; rather a decrease in the regeneration rate accounts for the loss of  $J_{sc}$ .

Finally, a novel, high-throughput, combinatorial approach for the synthesis and screening of mixed-metal oxides for use as water-splitting photocatalysts was developed. The methodology relies on inkjet printing to form quantitative mixtures of aqueous metal oxide precursors. After pyrolysis, the photoelectrochemical properties of metal oxides can be fully characterized in an automated high-speed system, including measurement of the  $V_{oc}$  and  $J-E$  curves.

# TABLE OF CONTENTS

Acknowledgements .....	iii
Abstract.....	viii
List of Figures .....	xvi
List of Tables .....	xx
<b>Chapter 1: Recent Trends in Global Energy Consumption and Carbon Dioxide Emissions and Implications for Future Energy Production .....</b>	<b>1</b>
1.1 Global Warming: The Impending Crisis .....	1
1.2 Historical Trends in CO <sub>2</sub> Levels .....	2
1.3 Current and Predicted CO <sub>2</sub> Emission Flux .....	3
1.3.1 Global Population and Gross World Product.....	3
1.3.2 Energy Intensity.....	4
1.3.3 Carbon Intensity .....	4
1.3.4 Projecting Carbon Emissions Based on Growth Scenarios.....	5
1.4 Current and Predicted Trends in Global Energy Consumption .....	7
1.5 The Promise and Problems of Solar Energy.....	8
1.6 Research Priorities and Future Directions .....	9
<b>References.....</b>	<b>21</b>

**Chapter 2: Operating Principles of Photoelectrochemical Cells for Solar Energy**

<b>Conversion .....</b>	<b>24</b>
2.1 Introduction .....	24
2.2 Photochemistry of Semiconductor-Liquid Junctions .....	25
2.2.1 Overview .....	25
2.2.2 Factors that Determine Overall Conversion Efficiency of a Solar Cell .....	26
2.3 Dye-Sensitized Solar Cells .....	28
2.3.1 Overview .....	28
2.3.2 Challenges to Further Improvement .....	30
2.3.3 Mechanisms and Models .....	32
2.3.3.1 Photovoltage .....	32
2.3.3.2 Electron Injection .....	34
2.3.3.2 Dye Reduction .....	36
2.3.3.4 Electron Loss or Electrolyte Recombination .....	37
2.4 Conclusions .....	37
<b>References .....</b>	<b>44</b>

<b>Chapter 3: Characterization of the Interfacial Energetics and Steady-State Current Density vs Potential Effects of Electrolyte Cations in Dye-Sensitized Solar Cells .....</b>	<b>47</b>
3.1 Introduction.....	47
3.2 Experimental.....	49
3.2.1 Materials.....	49
3.2.2 Fabrication of Photoelectrochemical Cells .....	50
3.2.3 Spectrochronocoulometry .....	51
3.2.4 Current Density vs Potential Measurements .....	52
3.2.5 Spectral Response .....	52
3.3 Results .....	53
3.3.1 Spectrochronocoulometry .....	53
3.3.2 <i>J-E</i> Behavior.....	54
3.3.3 Spectral Response .....	55
3.4 Discussion.....	57
3.4.1 Dependence of the Interfacial Energetics on the Nature of the Electrolyte Cation.....	57
3.4.2 Dependence of the <i>J-E</i> Behavior on the Nature of the Electrolyte Cation .....	59
3.4.3 Spectral Response Properties .....	61
3.5 Conclusions.....	63
3.6 Acknowledgments.....	63
<b>References.....</b>	<b>72</b>

<b>Chapter 4:</b>	<b>Time-Resolved Characterization of the Dependence of the Interfacial Electron-Transfer Rates on Electrolyte Ions in Dye-Sensitized Solar Cells.....</b>	<b>75</b>
4.1	Introduction.....	75
4.2	Experimental.....	78
4.2.1	Materials.....	78
4.2.2	Fabrication of Photoelectrochemical Cells.....	79
4.2.3	Femtosecond Transient Absorption Spectroscopy.....	80
4.2.4	Nanosecond Transient Absorption and Emission Spectroscopy... ..	81
4.3	Results.....	82
4.3.1	Femtosecond-Resolved Dynamics.....	82
4.3.1.1	Injection Dynamics in $\text{ClO}_4^-$ -Based Electrolytes.....	82
4.3.1.2	Injection Dynamics in Electrolytes Containing $\text{I}^-$ or $\text{I}_3^-$ .....	83
4.3.2	Nanosecond-Resolved Dynamics.....	84
4.3.2.1	Recombination with the Oxidized Dye.....	84
4.3.2.2	Regeneration by $\text{I}^-$ .....	85
4.3.2.3	Regeneration by $\text{I}^-$ with $\text{I}_3^-$ Present.....	85
4.3.2.4	Regeneration by Ferrocene Derivatives.....	86
4.3.2.5	Time-Resolved Emission.....	86
4.4	Discussion.....	87
4.4.1	Electron Injection into $\text{TiO}_2$ .....	87
4.4.2	Reduction of $[\text{Ru}^{\text{III}}(\text{H}_2\text{L}')_2(\text{NCS})_2]^+$ .....	92
4.5	Conclusions.....	97
<b>References.....</b>	<b>116</b>	

<b>Chapter 5: Combinatorial Synthesis of Mixed-Metal Oxides and High-Throughput Screening of Photovoltage for Water Splitting under Visible Light Illumination.....</b>	<b>119</b>
5.1 Introduction .....	119
5.1.1 The Challenge of Clean, Cheap, and Abundant Chemical Fuels	119
5.1.2 The Four Requirements for Photoelectrosynthetic Solar Cells...	120
5.1.3 Past and Current Research .....	121
5.2 Experimental.....	122
5.2.1 Material.....	122
5.2.2 Combinatorial Metal Oxide Synthesis.....	123
5.2.3 Characterization of Printed Metal Oxides.....	124
5.2.4 Photoelectrochemical Measurements .....	124
5.2.4.1 Photocurrent Measurements .....	125
5.2.4.2 Photovoltage Measurements.....	125
5.2.4.3 Current Density vs Potential Measurements.....	127
5.3 Results .....	127
5.3.1 Quantitative Mixing of Aqueous Metal Ion Solutions with an Inkjet Printer .....	127
5.3.1.1 Inkjet Printing.....	127
5.3.1.2 Determination of Metal Oxide Composition .....	129
5.3.2 Photoelectrochemical Characterization .....	129
5.3.2.1 Photocurrent Measurements .....	129
5.3.2.2 Photovoltage Measurements.....	130

5.3.2.3	Current Density vs Potential Behavior .....	134
5.4	Discussion .....	134
5.4.1	Inkjet Printing of Aqueous Metal Oxide Precursors.....	135
5.4.2	Photocurrent Measurements .....	136
5.4.3	Photovoltage Measurements .....	140
5.5	Conclusions .....	144
5.6	Acknowledgments.....	145
	<b>References .....</b>	<b>163</b>

## LIST OF FIGURES

<b>Figure 1.1</b>	Atmospheric concentration of CO <sub>2</sub> and annual temperature anomaly over the past 150 years.....	11
<b>Figure 1.2</b>	Atmospheric concentration of CO <sub>2</sub> and annual temperature anomaly over the past 420,000 years.....	12
<b>Figure 1.3</b>	Past and projected world population.....	13
<b>Figure 1.4</b>	Gross world product per capita.....	14
<b>Figure 1.5</b>	Energy use per gross world product.....	15
<b>Figure 1.6</b>	Carbon dioxide emissions per energy produced.....	16
<b>Figure 1.7</b>	Past and projected future CO <sub>2</sub> emissions.....	17
<b>Figure 1.8</b>	Past and projected concentration of atmospheric CO <sub>2</sub> .....	18
<b>Figure 1.9</b>	Cost of energy production by source.....	19
<b>Figure 1.10</b>	Distribution of electricity generation in the U. S.....	20
<b>Figure 2.1</b>	Schematic of the three known methods of converting solar energy.....	39
<b>Figure 2.2</b>	Typical <i>J-E</i> curves for a semiconductor liquid junction in the dark and under illumination.....	40
<b>Figure 2.3</b>	Solar irradiance spectrum compared with the band gaps of several common semiconductors.....	41
<b>Figure 2.4</b>	Schematic diagram of a dye-sensitized solar cell.....	42
<b>Figure 2.5</b>	Structure and absorption spectrum of the sensitizer Ru(H <sub>2</sub> L') <sub>2</sub> (NCS) <sub>2</sub> ....	43

<b>Figure 3.1</b>	Degree of capacitive charging of TiO <sub>2</sub> measured spectroelectrochemically in contact with ClO <sub>4</sub> <sup>-</sup> -based electrolyte solutions .....	66
<b>Figure 3.2</b>	Degree of capacitive charging of TiO <sub>2</sub> measured spectroelectrochemically in contact with electrolyte solutions containing I <sup>-</sup> and I <sub>3</sub> <sup>-</sup> .....	68
<b>Figure 3.3</b>	Current density vs applied potential curves in the dark and under illumination.....	69
<b>Figure 3.4</b>	External quantum yield curves for dye-sensitized solar cells as a function of electrolyte cations .....	70
<b>Figure 3.5</b>	Internal quantum yield curves for dye-sensitized solar cells as a function of electrolyte cations .....	71
<b>Figure 4.1</b>	Schematic diagram of electron transfer reaction in a DSSC .....	102
<b>Figure 4.2</b>	Femtosecond-resolved transient absorption spectra of Ru(H <sub>2</sub> L') <sub>2</sub> (NCS) <sub>2</sub> for electron injection in ClO <sub>4</sub> <sup>-</sup> -based electrolytes on TiO <sub>2</sub> .....	103
<b>Figure 4.3</b>	Femtosecond-resolved transient absorption spectra of Ru(H <sub>2</sub> L') <sub>2</sub> (NCS) <sub>2</sub> for electron injection in ClO <sub>4</sub> <sup>-</sup> -based electrolytes on ZrO <sub>2</sub> .....	104
<b>Figure 4.4</b>	Femtosecond-resolved transient absorption spectra of Ru(H <sub>2</sub> L') <sub>2</sub> (NCS) <sub>2</sub> for electron injection in I <sup>-</sup> /I <sub>2</sub> -based electrolytes on TiO <sub>2</sub> .....	105
<b>Figure 4.5</b>	Femtosecond-resolved transient absorption spectra of Ru(H <sub>2</sub> L') <sub>2</sub> (NCS) <sub>2</sub> for electron injection in I <sup>-</sup> /I <sub>2</sub> -based electrolytes on ZrO <sub>2</sub> .....	106

<b>Figure 4.6</b>	Femtosecond-resolved transient absorption spectra of Ru(H <sub>2</sub> L') <sub>2</sub> (NCS) <sub>2</sub> for electron injection in I <sup>-</sup> -based electrolytes on TiO <sub>2</sub> .....	107
<b>Figure 4.7</b>	Femtosecond-resolved transient absorption spectra of Ru(H <sub>2</sub> L') <sub>2</sub> (NCS) <sub>2</sub> for electron injection in I <sup>-</sup> -based electrolytes on ZrO <sub>2</sub> .....	108
<b>Figure 4.8</b>	Nanosecond-resolved transient absorption spectra of Ru(H <sub>2</sub> L') <sub>2</sub> (NCS) <sub>2</sub> for the recombination reaction in ClO <sub>4</sub> <sup>-</sup> -based electrolytes on TiO <sub>2</sub> .....	109
<b>Figure 4.9</b>	Nanosecond-resolved transient absorption spectra of Ru(H <sub>2</sub> L') <sub>2</sub> (NCS) <sub>2</sub> for the regeneration reaction in I <sup>-</sup> -based electrolytes on TiO <sub>2</sub> .....	110
<b>Figure 4.10</b>	Nanosecond-resolved transient absorption spectra of Ru(H <sub>2</sub> L') <sub>2</sub> (NCS) <sub>2</sub> for the regeneration reaction in I <sup>-</sup> /I <sub>2</sub> -based electrolytes on TiO <sub>2</sub> .....	111
<b>Figure 4.11</b>	Nanosecond-resolved transient absorption spectra of Ru(H <sub>2</sub> L') <sub>2</sub> (NCS) <sub>2</sub> for the regeneration reaction with ferrocenes in ClO <sub>4</sub> <sup>-</sup> -based electrolytes on TiO <sub>2</sub> .....	112
<b>Figure 4.12</b>	Time-resolved emission decay of Ru(H <sub>2</sub> L') <sub>2</sub> (NCS) <sub>2</sub> on TiO <sub>2</sub> and ZrO <sub>2</sub> .	113
<b>Figure 4.13</b>	Schematic diagram of the energetics at the TiO <sub>2</sub> -liquid interface as a function of cations in solution .....	114
<b>Figure 5.1</b>	Grayscale TIFF image used to print mixed metal oxides .....	147
<b>Figure 5.2</b>	Photographs of mixed metal oxides printed on a FTO substrate .....	148
<b>Figure 5.3</b>	Schematic of the setup for photocurrent measurements .....	150
<b>Figure 5.4</b>	Schematic of the procedure for preparing electronically isolated mixed metal oxides on a single FTO substrate .....	151
<b>Figure 5.5</b>	Schematic of the setup for photovoltage measurements .....	154

<b>Figure 5.6</b>	Typical SEM image and EDS compositional analysis.....	155
<b>Figure 5.7</b>	Three-dimensional plots of the photocurrent 252 binary mixed metal oxides.....	156
<b>Figure 5.8</b>	Photovoltages of repeating pattern of five materials printed at varying thickness .....	158
<b>Figure 5.9</b>	Semi-log plot of the photovoltage vs light intensity for five metal oxides	159
<b>Figure 5.10</b>	Plot of photovoltage and light-dark behavior for binary mixed metal oxides.....	160
<b>Figure 5.11</b>	<i>J-E</i> curves of a TiO <sub>2</sub> sample printed on an etched FTO substrate .....	162

## LIST OF TABLES

<b>Table 3.1</b>	Relative shifts of $E_{accept}$ in TiO <sub>2</sub> as a function of the cations in the contacting electrolyte .....	64
<b>Table 3.2</b>	Summary of results of $J-E$ curves as a function of the cations in the contacting electrolyte .....	65
<b>Table 4.1</b>	Femtosecond-resolved transient absorbance data: electron injection from Ru(H <sub>2</sub> L') <sub>2</sub> (NCS) <sub>2</sub> .....	99
<b>Table 4.2</b>	Nanosecond-resolved transient absorbance data: recombination and regeneration of Ru(H <sub>2</sub> L') <sub>2</sub> (NCS) <sub>2</sub> by I <sup>-</sup> .....	100
<b>Table 4.3</b>	Nanosecond-resolved transient absorbance data: regeneration of Ru(H <sub>2</sub> L') <sub>2</sub> (NCS) <sub>2</sub> by ferrocenes.....	101
<b>Table 5.1</b>	Measured and expected atomic percent composition of inkjet printed mixed metal oxides.....	146

## **CHAPTER 1**

### ***Recent Trends in Global Energy Consumption and Carbon Dioxide Emissions and Implications for Future Energy Production***

#### **1.1 GLOBAL WARMING: THE IMPENDING CRISIS**

The threat of global warming has made it increasingly imperative that energy sources be developed that do not emit carbon dioxide or other greenhouse gases. Globally, emissions of CO<sub>2</sub> are growing, and faster now than anytime in the last 20 years.<sup>1,2</sup> The mounting evidence is incontrovertible that global warming will have significant effects on the Earth in the future, both environmental and financial; the only question that remains to be seen is just how large the cost will be. It has been argued that the costs of efforts to reduce greenhouse gas emissions will simply be too large and that the future is still too uncertain to invest in making changes that may ultimately be unnecessary. However a serious flaw exists in this argument: once it is established with certainty that global warming is causing serious harm to our planet and its inhabitants, it will not only be too late to alter the situation, but the damage will have lasting consequences for a timescale comparable to modern human history. The only way to

find out the result of the experiment is to actually do the experiment itself. Once done, it cannot be undone.

## 1.2 HISTORICAL TRENDS IN CO<sub>2</sub> LEVELS

Despite the uncertainties that remain in climate modeling predictions and the consequences of higher atmospheric concentrations of CO<sub>2</sub>, certain facts speak for themselves. The concentration of CO<sub>2</sub> in the atmosphere has been rising steadily for the last 200 years (from a pre-industrial revolution level of 280 ppm to a present-day level of over 380 ppm),<sup>3,4</sup> and this growth rate has increased substantially over the last 50 years.<sup>5</sup> Similarly, the average global temperature has on average been rising for the last 100 years, with this trend accelerating over the last 40 years (see Figure 1.1).<sup>6,7</sup> The concentration of atmospheric CO<sub>2</sub> has not been as high as it is today for the last 420,000 years: the average atmospheric CO<sub>2</sub> concentration during this period is 230 ppm, and was never greater than 300 ppm or less than 180 ppm.<sup>8</sup> Furthermore, over those half million years or so, the trends in atmospheric CO<sub>2</sub> levels are nearly perfectly correlated in time with global temperature (see Figure 1.2).<sup>9</sup> Ice ages have come and gone during this time. Finally, if CO<sub>2</sub> emissions continue to grow at the same rate at which they have for the last 5–10 years,<sup>2</sup> the concentration of CO<sub>2</sub> will reach the *double* the current global levels by the year 2060. Unless changes are made to dramatically reduce the growth rate of emissions, there is no question that the concentration of CO<sub>2</sub> in the atmosphere will not stabilize, simply continuing to rise unabated throughout the 21<sup>st</sup> century. There is no way to accurately predict the consequences on the global climate of such high CO<sub>2</sub> levels.

### 1.3 CURRENT AND PREDICTED CO<sub>2</sub> EMISSION FLUX

The global CO<sub>2</sub> emission flux is determined by the product of four factors, according to the Kaya identity:<sup>10,11</sup>

$$F = P \left( \frac{G}{P} \right) \left( \frac{E}{G} \right) \left( \frac{F}{E} \right) = Pgef, \quad 1.1$$

where  $P$  is the global population,  $G$  is the gross world product (GWP),  $E$  is the global primary energy consumption, and  $F$  is the carbon flux. Historically, increasing CO<sub>2</sub> emissions have been driven by the growing world population and increasing GWP per capita ( $g$ ). In contrast, the growth rate of emissions have been offset by the decreases in the energy consumed per GWP ( $e$ ) and the decreasing carbon intensity of energy production ( $f$ ). The Kaya identity can be used to better understand the various contributions to the trend in CO<sub>2</sub> emissions over time, and projecting historical growth rates of each factor into the future, it is possible to predict future carbon emissions. While trends are qualitatively expected to continue for the foreseeable future, the growth rates of the four factors in the Kaya identity have not remained constant in the recent past.

#### 1.3.1 Global Population and Gross World Product

From 1980 to 2000, the global population,  $P$ , grew at an average rate of 1.57%, but from 2000 to 2006, the growth rate decreased slightly to 1.20%, with a current world population of 6.6 billion (as of July 2007) (see Figure 1.3).<sup>12,13</sup> In contrast, growth rates of GWP per capita,  $g$ , have gone up, although the precise analysis depends on the method in which the GWP is calculated (see Figure 1.4). The difference lies in how the gross domestic products (GDP) of individual nations are calculated and compared with each other. GDPs can be compared either using the market exchange rate or purchasing power

parity (the per capita values are denoted as  $g_m$  and  $g_p$  respectively). Using the value of  $g_p$  gives more weight to developing economies, and is more appropriate when comparing countries' relative well-being and their energy intensity.<sup>10,14</sup> The growth rate of GWP per capita has gone up by both measures, although  $g_p$  more dramatically than  $g_m$ . Average growth rates of  $g_p$  and  $g_m$ , for the period 1980–2000, were 1.80% and 1.29%, while during 2000–2006 they grew at 2.98% and 1.66% respectively (an increase of 65% for  $g_p$  compared with 28% for  $g_m$ ).<sup>10,15</sup>

### 1.3.2 Energy Intensity

Meanwhile, the global energy intensity,  $e$ , or amount of primary energy consumed per GWP, continues to drop, although the rate of decrease has leveled off in the last several years (see Figure 1.5). Again, as the exact value of  $e$  is sensitive to how  $G$  is calculated (denoted  $e_p$  and  $e_m$ ), the numbers vary, but the trend is the same. From 1980 to 2000, energy intensity decreased at a rate of 1.56% and 1.06% for  $e_p$  and  $e_m$  respectively, while from 2000 to 2006, this rate of decrease dropped to 1.33% and 0.01% respectively, essentially leveling off as measured by  $e_m$ .<sup>10,15,16</sup>

### 1.3.3 Carbon Intensity

Finally, the trend in the global carbon intensity of energy production,  $f$ , has also recently shifted. For over a century,  $f$  has dropped as humans have shifted from burning wood, to coal, and more recently to oil and natural gas (as well as the addition of nuclear fission and hydroelectric generation to the energy mix) (see Figure 1.6). From 1980 to 2000,  $f$  decreased at a rate of 0.27%, but from 2000 to 2004, the trend was reversed and  $f$  actually *increased* at a rate of 0.56%.<sup>17,1</sup> While the carbon intensity of most individual nations has not changed significantly in the last 25 years,<sup>10</sup> the recent reversal in the trend

in dropping carbon intensity is instead due to the changing relative contributions of developed vs developing nations. In particular, China is a driving force: in 1990 China produced less than 7% of the world's energy, but by 2004, this had more than doubled.<sup>10</sup> Throughout this time, China's carbon intensity was on average 32% larger than the world average.<sup>10</sup> In contrast, the United States, which produced nearly 28% of the world's energy in 1990, contributed slightly less (23%) to the total in 2004, while its carbon intensity was slightly lower than the world average.<sup>10</sup> The tremendous surge in especially carbon-intensive energy production by China (along with other rapidly developing nations) has resulted in the recent increases in world-average carbon intensity. In other words, while the large majority of the current build-up of CO<sub>2</sub> in the atmosphere is due to emissions from developed nations over the last 100 years or so, due to their rapid economic growth, many developing nations are now emitting per year as much as or more than developed nations. In fact, in 2007 China surpassed the United States as the leading emitter of CO<sub>2</sub> worldwide; in 1990, China produced less than half the emissions of the U.S.<sup>2</sup>

#### **1.3.4 Projecting Carbon Emission based on Growth Scenarios**

Projecting trends in  $P$ ,  $g_p$ ,  $e_p$ , and  $f$  into the future, it is possible to estimate future carbon emissions by simply adding their individual rates of change. Using the Kaya identity and the individual average growth rates of  $P$ ,  $g_p$ ,  $e$ , and  $f$  from 1980 to 2000, the calculated growth rate of CO<sub>2</sub> emissions was 1.54% (compared to 1.39% as measured directly).<sup>1</sup> However, for 2000–2006 the calculated growth rate of CO<sub>2</sub> emissions was 3.40% (compared with 3.32% measured directly).<sup>2</sup> This disparity in growth rates of nearly 2% leads to vastly different predictions of scenarios for future carbon emissions

and the necessary steps to mitigate those emissions, as seen in Figure 1.7. In 1998, Hoffert et al. used the Kaya identity to create a series of scenarios of carbon emissions for stabilization at various concentrations of CO<sub>2</sub>.<sup>11</sup> The so-called “business as usual” scenario from the IS92a scenario in the 1992 IPCC report,<sup>18</sup> in which no new climate change policies are assumed, was taken as the worst-case scenario in which CO<sub>2</sub> levels never stabilize, while other projections were created for stabilization from 350 ppm to 750 ppm atmospheric CO<sub>2</sub>. The global CO<sub>2</sub> emissions necessary to reach these stabilization targets, as well as those predicted by the IS92a course of action, are plotted in Figure 1.8, and compared with the recent growth rates of 3.4%. This plot shows clearly that if the current growth rate of CO<sub>2</sub> emissions continues unabated, levels of CO<sub>2</sub> will rise far beyond double or even triple their current value of 380 ppm, and will certainly not stabilize on any reasonable timescale.

It could certainly be argued that it is not reasonable to assume a growth rate of carbon emissions of over 3% will occur in the long-term. As the world population nearly doubles over the next 100 or so years, the growth rate will almost certainly decrease. It is unlikely that the current growth of the GWP will remain above 3% indefinitely. For comparison, let us make the following more conservative assumptions: a growth rate of 1.0% for the population, 1.5% for the GWP per capita, a drop of 1.5% in energy intensity, and no decrease in carbon intensity. This results in a net 1.0% growth rate of carbon emissions, as plotted in Figure 1.8, and is essentially indistinguishable from the IS92a scenario.

## 1.4 CURRENT AND PREDICTED TRENDS IN GLOBAL ENERGY CONSUMPTION

Based on the projections for the various 21<sup>st</sup> century scenarios, Hoffert et al. calculated the amount of primary power generation that would be necessary worldwide to meet demand—and the amount that would be required without the production of any CO<sub>2</sub> emissions. The projections for carbon-free power generation for the various scenarios are shown in Figure 1.9. Following the business-as-usual IS92a scenario, which—given the 2000–2006 carbon emission data—may in fact be optimistic, by the year 2050 some 10 terrawatts of primary power are required completely carbon free. To stabilize atmospheric concentrations at 450 ppm, this number grows to more than 20 TW. The current total rate of energy production in the world today is 14.5 TW; less than 1.2 TW of that is produced carbon-free (mostly by nuclear fission and hydroelectric generation).<sup>16</sup> This means that within 40 years, the world's production of carbon-free energy must increase tenfold its present value, and if CO<sub>2</sub> levels can be expected to stabilize at twice their pre-industrial levels, this number grows to twenty- or thirtyfold. The following fact gives a good sense of the scale of such an undertaking: in order to produce 10 TW of carbon-free energy using nuclear fission, the only established technology that could possibly scale up to such a level, it would require a new 2 GW nuclear power plant coming online every 3.7 days for the next 50 years. Such unprecedented growth would raise a host of political, safety, and security issues with no obvious solutions.

Because of the current abundance and low-cost of fossil fuels, such as coal, oil, and natural gas,<sup>19</sup> any large-scale changeover to a carbon-neutral alternative energy

source must not only be viable technologically, but financially competitive. Not only must this potential energy source be able to provide the nearly 20 TW of power consumption globally, but also it must do so at cost competitive with coal (currently the lowest-cost and most-abundant energy source) if any alternative to fossil fuels is to be adopted universally. Currently, the cost of electricity generated from fossil fuels is 5–10 times cheaper than that from carbon-free sources (with the exception of hydroelectric generation), as shown in Figure 1.10.<sup>20,21</sup> This cost disparity is to some extent reflected in how electricity is produced in the U.S., as shown in Figure 1.11, where nearly 50% of electricity is generated from coal, the lowest-cost fuel, but the one with the highest carbon intensity.<sup>21</sup> Therefore, any carbon-free energy source must not only have sufficient capacity to meet the rapidly growing global demand, but must be able to meet the economic constraints of a free market.

## **1.5 THE PROMISE AND PROBLEMS OF SOLAR ENERGY**

Solar energy is able to meet global demand for power by several orders of magnitude: the solar flux on the surface of the Earth is some 120,000 TW. Given that the amount of solar energy striking the earth in one year is nearly 10,000 times greater than all energy used by humans in that same year, why then does it account for less than 0.05%<sup>19</sup> of the world's total energy production? This insignificant contribution is due to two principal problems with solar power: first and foremost is its price and secondly its form. In fact, these two issues compound each other.

The most efficient method of harvesting solar power is with solid-state photovoltaic (PV) devices, which have just recently reached a new record maximum

overall conversion efficiency of 42.8%.<sup>22</sup> While very efficient, an inherent limitation of PV devices is they can only produce electricity. As a form of energy, electricity is not the most practical for many applications because it is difficult to store efficiently. The inescapable fact that any terrestrial solar energy harvesting must deal with is that the sun rises and sets each day. Therefore the energy produced during the day must be stored for nighttime usage. While numerous methods are available for storing electricity, all incur significant efficiency losses during the charging and discharging processes, and furthermore, many are simply not able to accommodate diurnal cycling or have unacceptably short operating lifetimes. While storage technology is continually improving, the additional steps required to store the electricity generated will necessarily diminish the overall efficiency of the energy production process.

The second problem with PV is the cost of raw materials, fabrication, and installation of modules. This is not an inherent problem and one that can be (and is being) addressed by both technological advances and the cost reductions that come with large-scale production of any commodity. In California, in 2003, the cost of electricity from PV is \$40–120 per GJ, whereas the cost of electricity from conventional methods is only \$7–20 per GJ (Figure 1.10).<sup>20</sup>

## **1.6 RESEARCH PRIORITIES AND FUTURE DIRECTIONS**

Therefore, a current priority in solar energy research is to generate energy in the form of chemical fuels rather than electricity, and to do so efficiently at a greatly reduced cost. It is within this context that the research presented herein was performed, and the

projects described in the following chapters were conceived and executed with the motivation to solve these two problems.

In particular, my work has centered on metal oxide semiconductors and how these materials can be either chemically altered or synthesized for use as photoelectrodes. Most metal oxides are wide band gap semiconductors, and are thus not generally suitable for terrestrial solar energy conversion due to the fact that they only absorb ultraviolet (UV) light, which is almost entirely filtered out by ozone in the earth's atmosphere. The low cost and chemical stability of metal oxides and their semiconducting properties nonetheless makes them very attractive solar cell materials. How then can these materials be used as efficient light-harvesting materials? How can the electrochemical properties of metal oxides be controlled by simple chemical means for improved solar cell performance? How can a large number of new metal oxides be synthesized and their key properties tested using a fast, high-throughput combinatorial approach?

These questions are addressed herein in the context of two fairly different systems. In the first case, titanium dioxide,  $\text{TiO}_2$ , was sensitized so as to absorb sunlight using a molecular dye, thereby generating electricity in a photoelectrochemical cell. The thermodynamics and kinetics of the electron transfer processes occurring at the  $\text{TiO}_2$  surface are described in detail. In the second case, new metal oxides were synthesized and characterized. A high-throughput method was developed to generate libraries of new metal oxide materials and measure their properties. First, in the following chapter, key concepts in photoelectrochemistry, as pertains to metal-oxide based solar cells, are introduced followed by a detailed discussion of experimental results obtained for these photoelectrochemical systems in the three subsequent chapters.

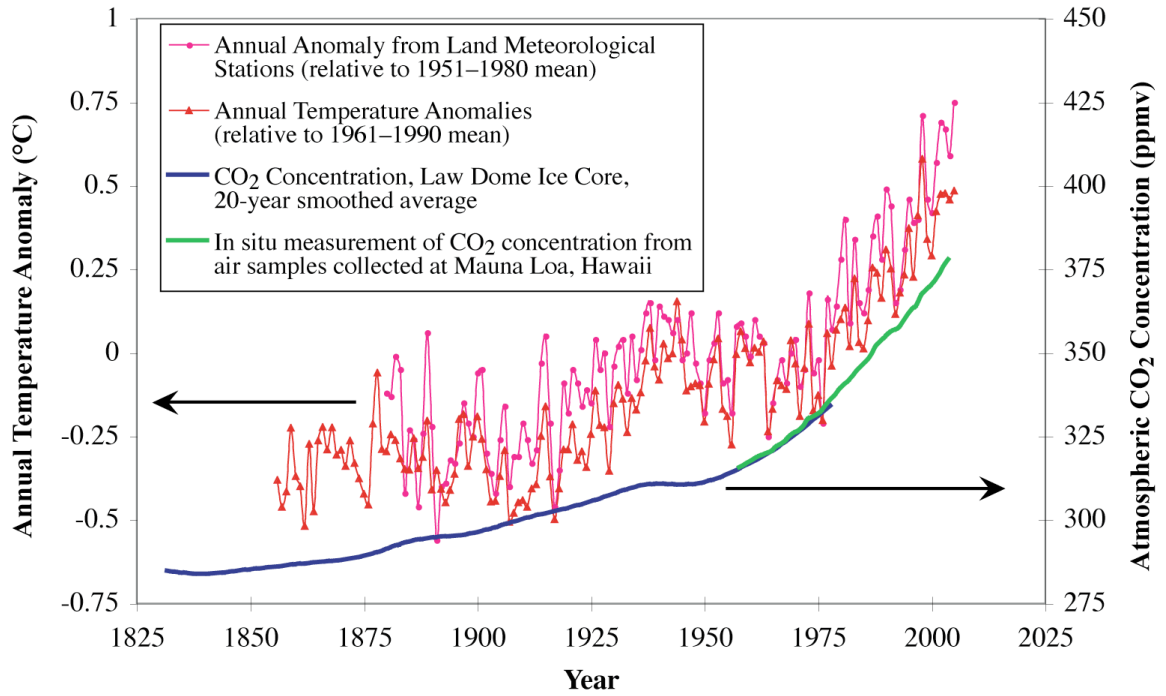


**Figure 1.1** Atmospheric concentration of CO<sub>2</sub>, from in situ measurements collected from Mauna Loa, Hawaii, and from the Law Dome ice core compared to the average temperature anomaly over the last 150 years<sup>3,5-7</sup>

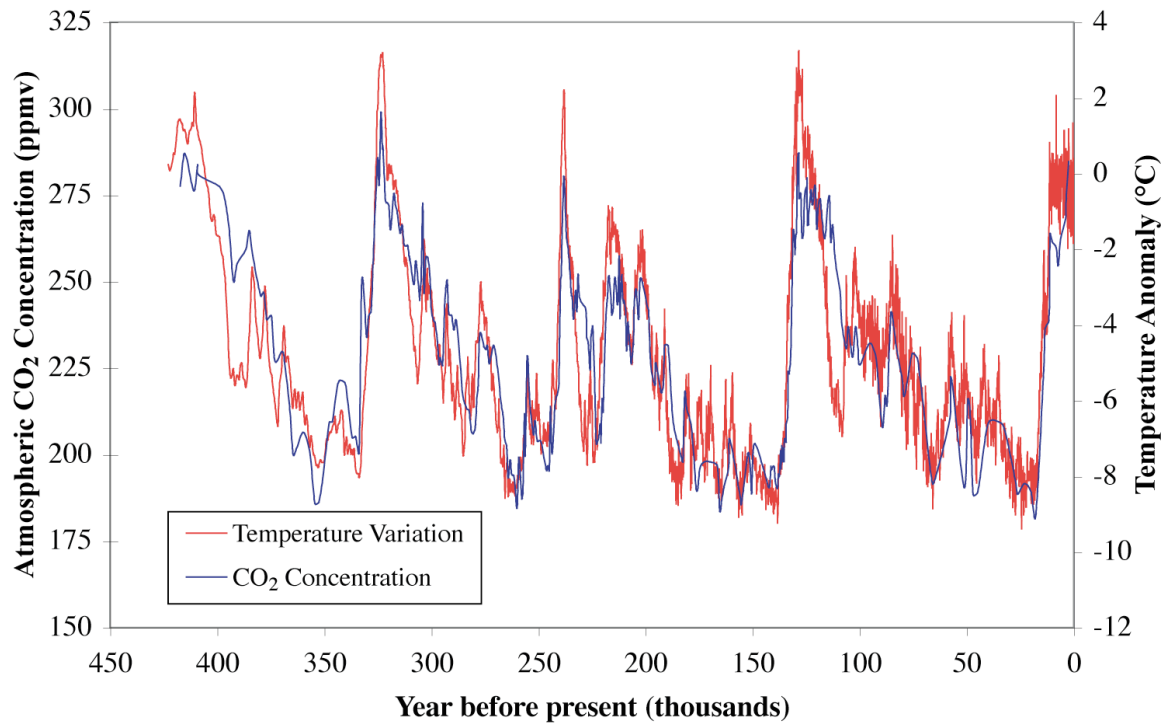


**Figure 1.2** Concentrations of atmospheric CO<sub>2</sub> (parts per million by volume) and the temperature anomaly in degrees Celsius over the last four hundred and twenty thousand years, as determined from the Vostok ice core<sup>8,9</sup>

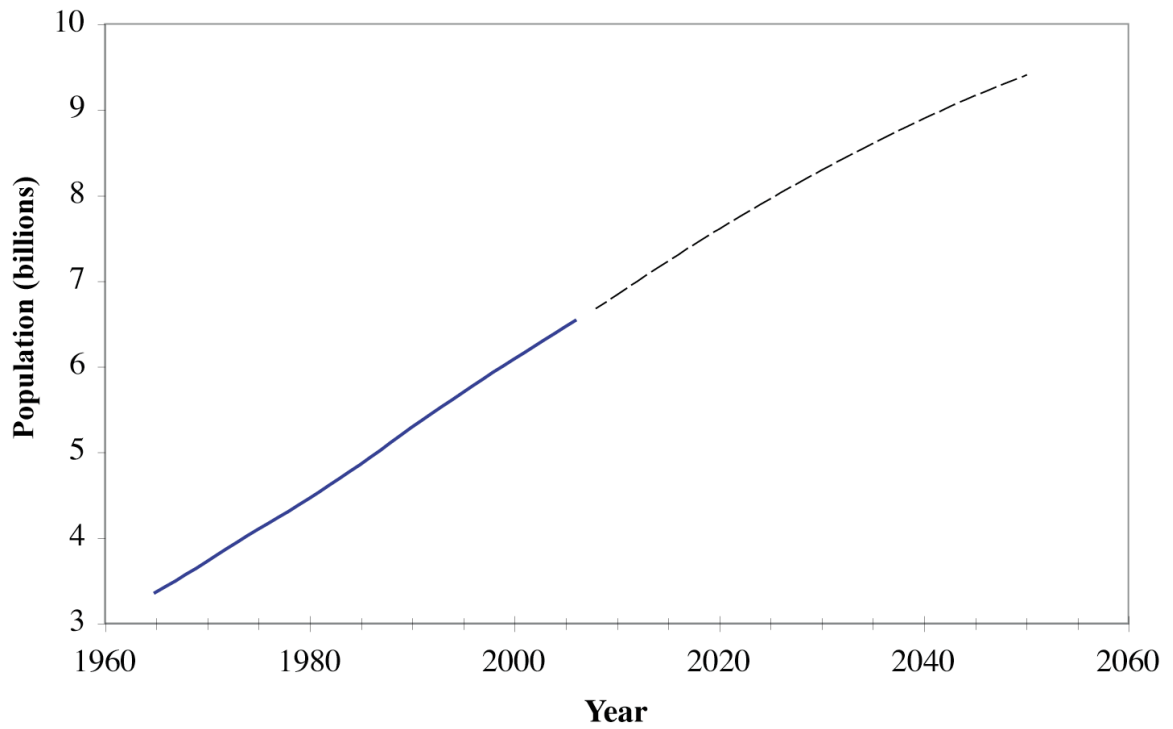


**Figure 1.3** Global population in billions over the last 40 years and projected into the future, showing a steady rise of approximately 1% per annum<sup>12</sup>

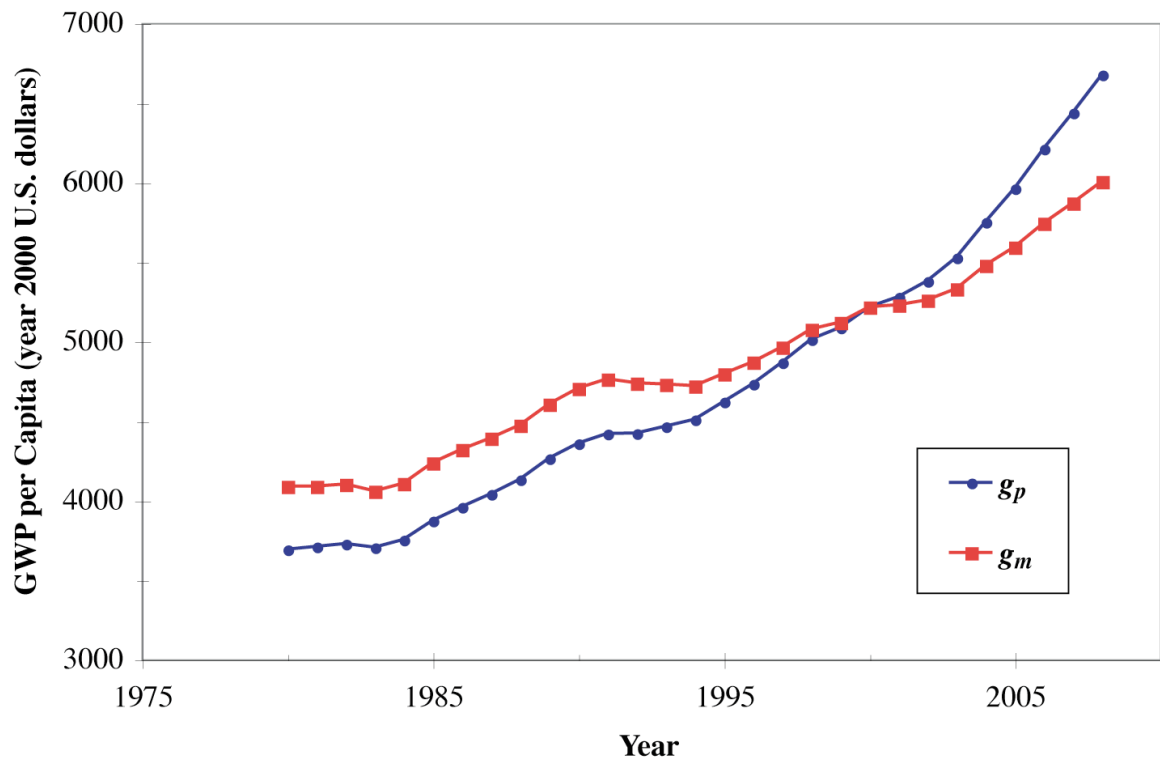


**Figure 1.4** Gross world product per capita, in year 2000 U. S. dollars, showing calculations using two methods to calculate the GWP. The value of GWP using purchasing power parity (PPP) gives more weight to the economies of developing countries. The growth of the GWP per capita calculated using the market exchange rate (MER) does not show as strong growth over the last 25 or so years.<sup>10,15</sup>

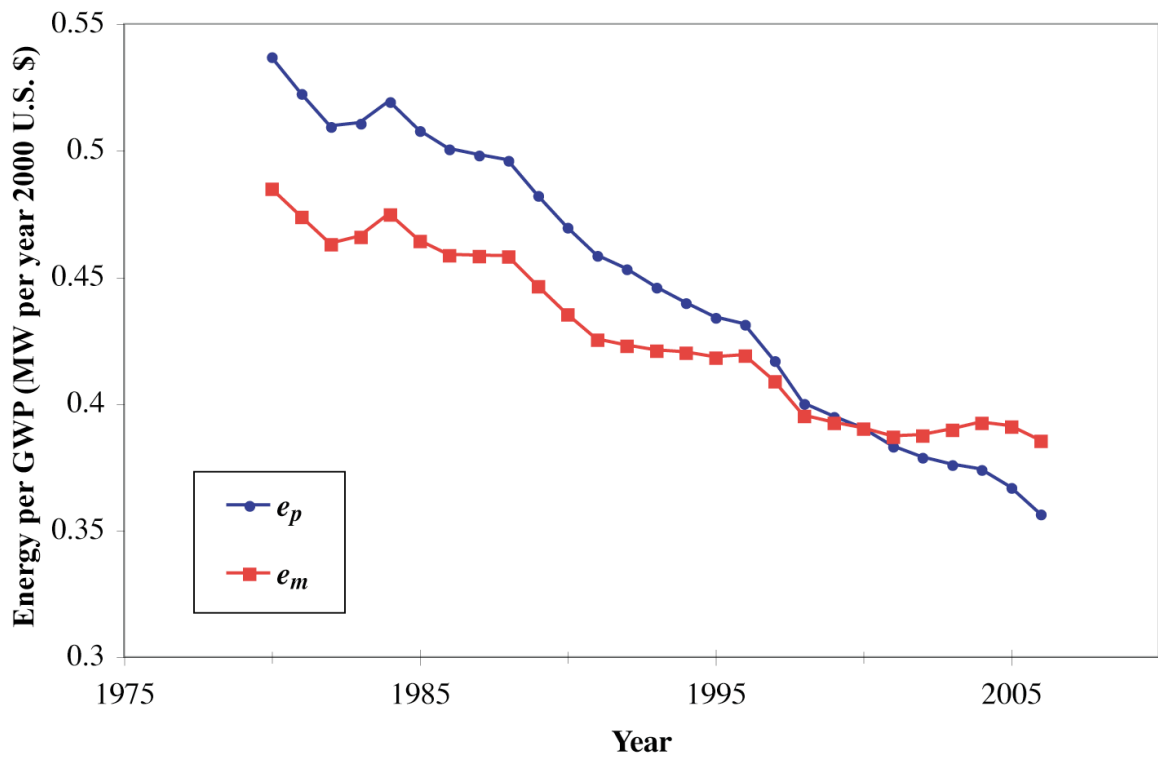


**Figure 1.5** The amount of energy per unit economic activity, which depends somewhat on how the value of the GWP is calculated. Because of the larger growth rates in the GWP as calculated using PPP, the plot of energy intensity is nearly flat for the last 5–10 years. In contrast, calculated using MER, the plot of energy intensity shows a continuing decrease.<sup>10,15,23</sup>

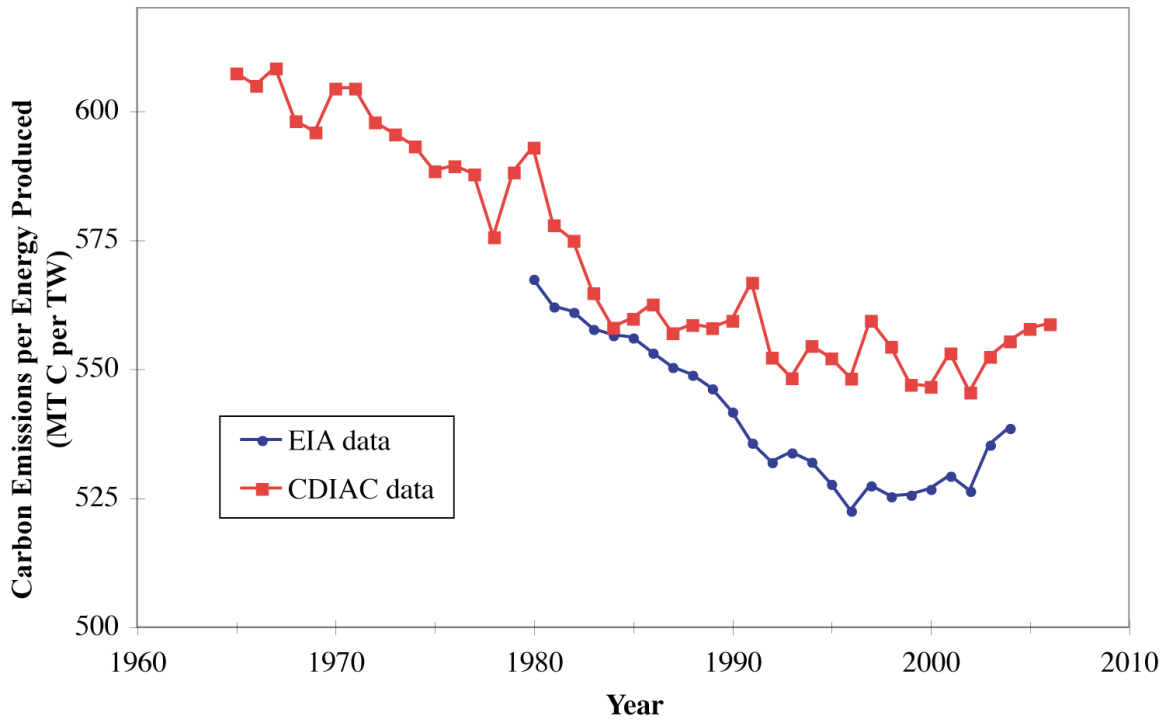


**Figure 1.6** Total carbon emissions per power produced globally according to two different U. S. Department of Energy databases, the Carbon Dioxide Information Analysis Center (CDIAC) and the Energy Information Administration (EIA). Although the actual value of the carbon intensity varies by  $\sim 5\%$  depending on the values of the global carbon emissions, the trend in the last 5–10 years is clear in both cases. Although the global carbon intensity had been decreasing for some 30 years or more, this trend has recently been reversed and the carbon intensity has risen. This reversal has apparently occurred despite growing awareness of the risks of global warming.<sup>1,24</sup>

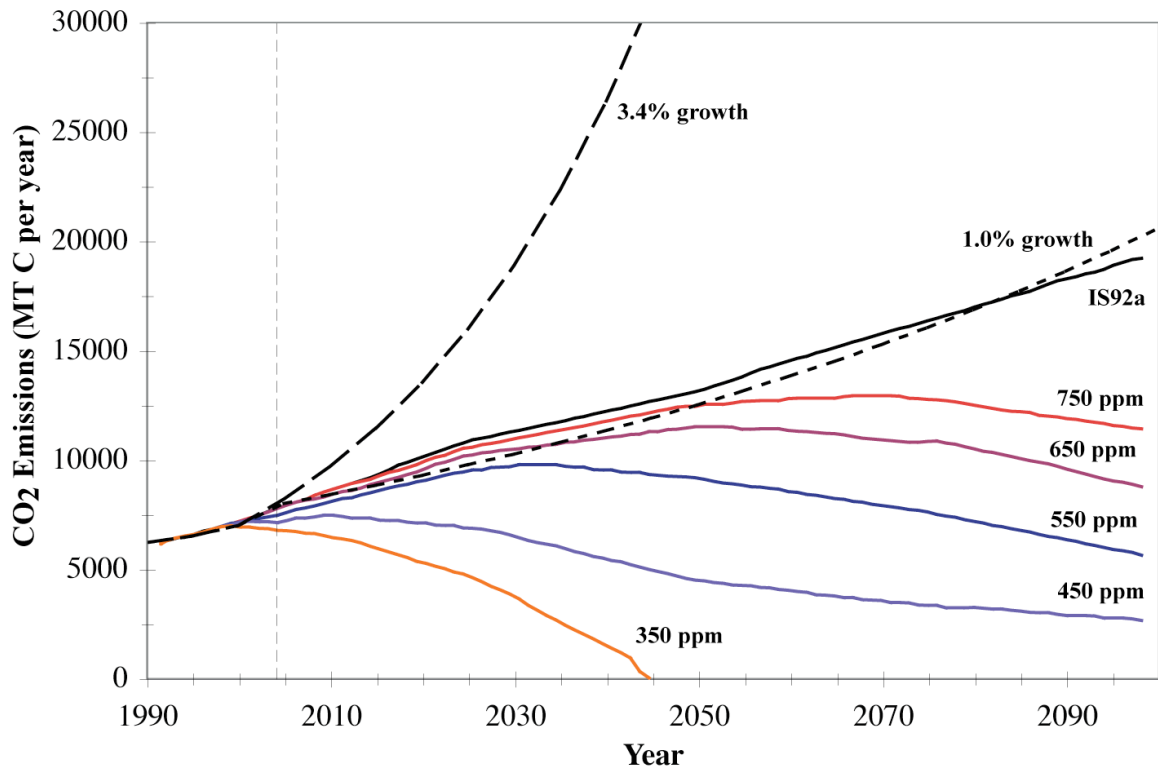


**Figure 1.7** Past and projected future CO<sub>2</sub> emissions as predicted by various growth scenarios. The various stabilization projections from Hoffert et al.<sup>11</sup> are shown as a reference to compare with 1.0% and 3.4% constant growth rates (shown as dashed lines). The labels refer to the level at which the atmospheric concentration will eventually stabilize under that scenario. The IS92a is the IPCC “business as usual” scenario, under which the concentration of CO<sub>2</sub> continues to rise throughout this century and the next.

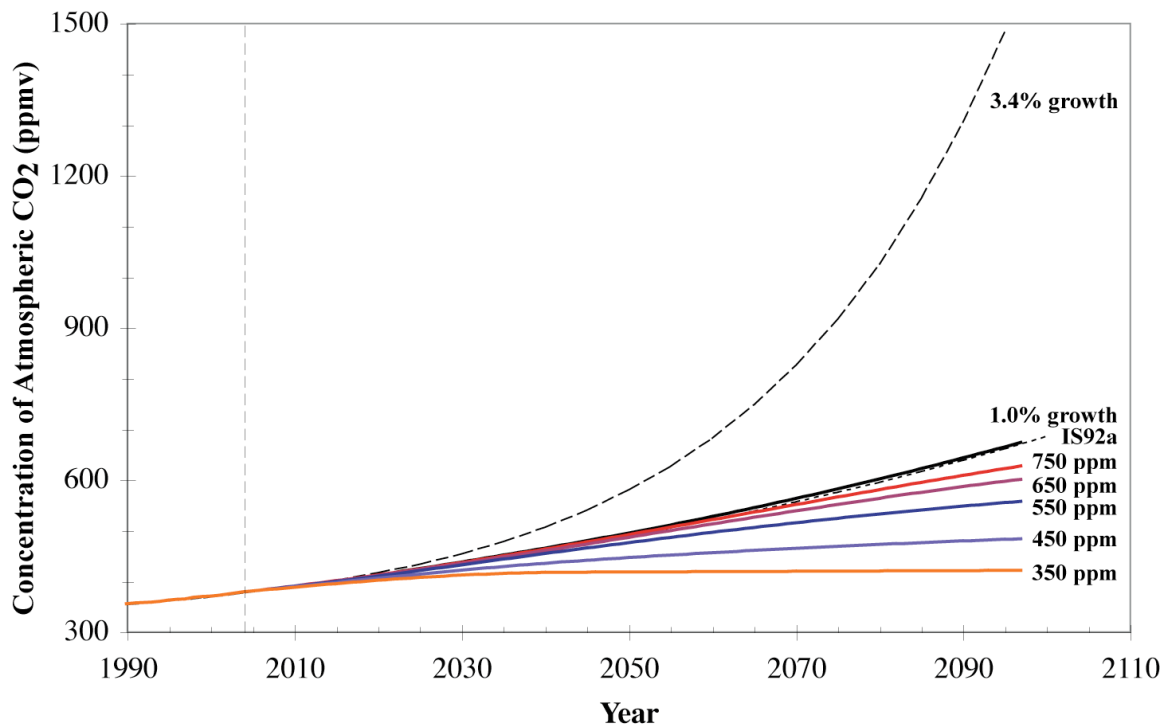


**Figure 1.8** The projected effects of CO<sub>2</sub> emissions on the atmospheric concentration of CO<sub>2</sub> for different growth scenarios.<sup>11</sup> This plot shows that before the end of the 21<sup>st</sup> century, if CO<sub>2</sub> emissions continue to grow at current rates, the concentration of CO<sub>2</sub> will be nearly five times the already record-breaking current levels. Even if the growth rate is reduced to 1%, the concentration of CO<sub>2</sub> is predicted to approximately double current levels by the year 2100. The labels refer to the level at which the atmospheric concentration will eventually stabilize under that scenario. The IS92a is the IPCC “business as usual” scenario, under which the concentration of CO<sub>2</sub> continues to rise throughout this century and the next.

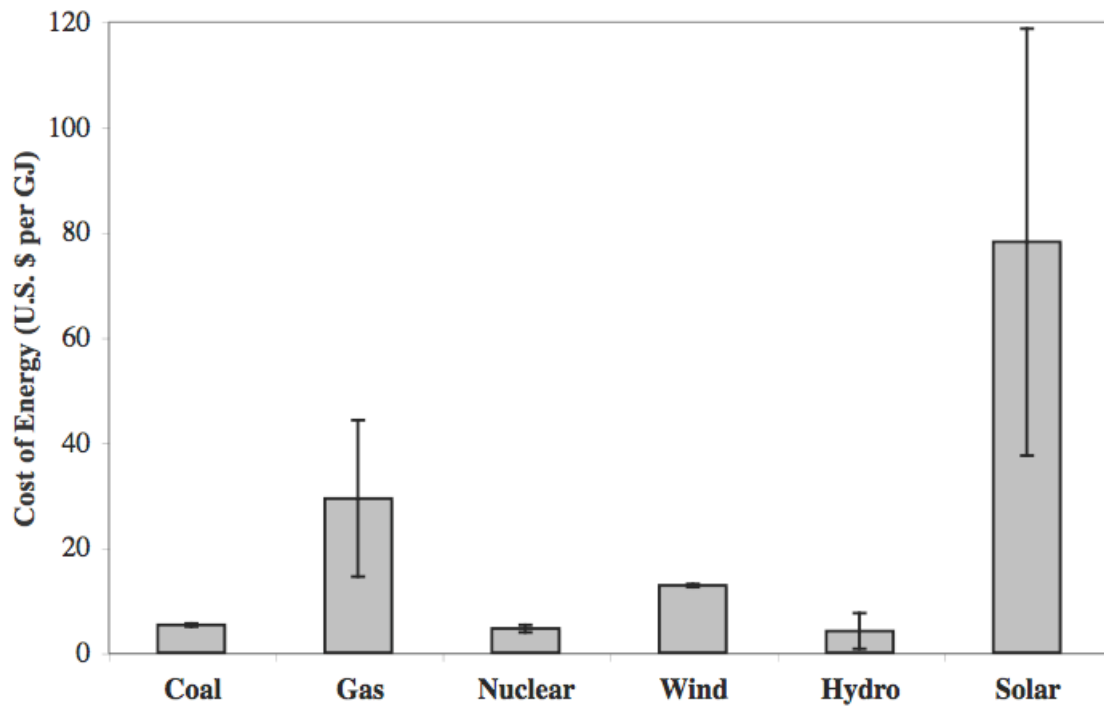


**Figure 1.9** Cost of various forms of energy in U. S dollars per gigajoule. The bars are not error bars, but rather indicate the range of values possible, which depend on a number of factors.<sup>20</sup>

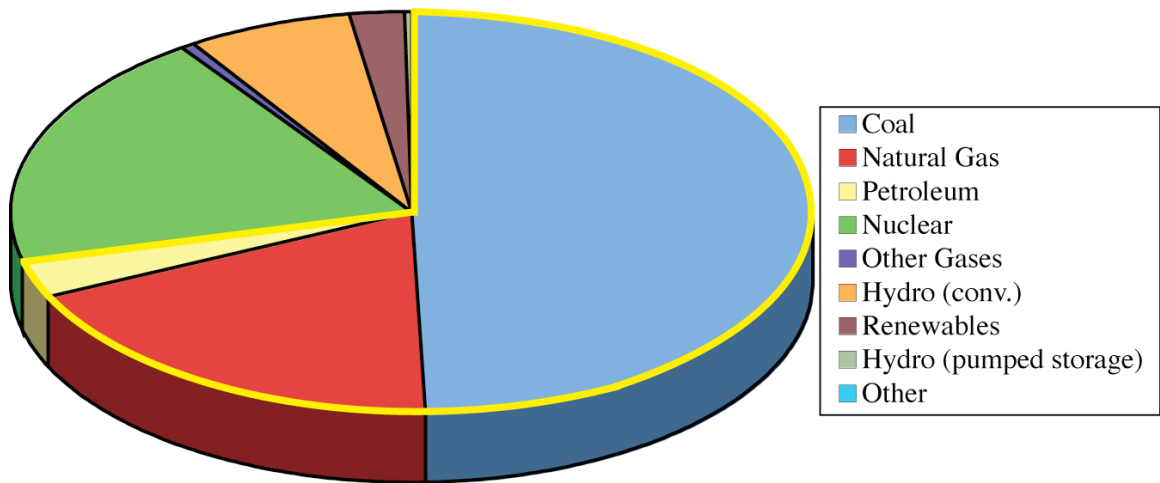


**Figure 1.10** Distribution of how electricity is generated in the U. S. (2005). Coal is used to generate nearly 50% of all electricity, with natural gas and nuclear fission accounting for the majority of the remainder. The area outlined in yellow corresponds to the total contribution of fossil fuels. Only a small fraction is generated renewably from sources such as hydroelectric, wind, and solar power.<sup>21</sup>

**REFERENCES**

- (1) Department of Energy, Energy Information Administration, *International Carbon Dioxide Emissions from the Consumption of Energy*. <http://www.eia.doe.gov/emeu/international/carbondioxide.html> (7-22-07).
- (2) Netherlands Environmental Assessment Agency, *China now no. 1 in CO<sub>2</sub> emissions; USA in second position*. <http://www.mnp.nl/en/dossiers/Climatechange/moreinfo/Chinanowno1inCO2emissionsUSAinsecondposition.html> (7-22-07).
- (3) Etheridge, D. M.; Steele, L. P.; Langendelds, R. L.; Francey, R. J. *Historical CO<sub>2</sub> record from the Law Dome DE08, DE08-2, and DSS ice cores*. <http://cdiac.ornl.gov/ftp/trends/co2/lawdome.combined.dat> (7-25-07).
- (4) Neftel, A.; Friedli, H.; Moor, E.; Lotscher, H.; Oeschger, H.; Siegenthaler, U.; Stauffer, B. *Historical CO<sub>2</sub> Record from the Siple Station Ice Core*. <http://cdiac.ornl.gov/ftp/trends/co2/siple2.013> (7-25-07).
- (5) Keeling, C. D. *Atmospheric CO<sub>2</sub> Concentrations (ppmv) derived from in situ air samples collected at Mauna Loa Observatory, Hawaii, 2005*. <http://cdiac.esd.ornl.gov/ftp/trends/co2/maunaloa.co2> (7-23-07).
- (6) Hansen, J. E.; Ruedy, R.; Lo, K. *Global Annual Temperature Anomalies (Land Meteorological Stations): 1880-2005*. [http://cdiac.esd.ornl.gov/ftp/trends/temp/hansen/gl\\_land.dat](http://cdiac.esd.ornl.gov/ftp/trends/temp/hansen/gl_land.dat) (7-23-07).
- (7) Jones, P. D.; Parker, D. E.; Osborn, T. J.; Briffa, K. R. *Global Monthly and Annual Temperature Anomalies (degrees C), 1856-2005*. <http://cdiac.ornl.gov/ftp/trends/temp/jonescru/global.dat> (7-27-07).

- (8) Barnola, J. M.; Raynaud, D.; Lorius, C.; Barkov, N. I. *Historical CO<sub>2</sub> Record from the Vostok Ice Core*, <http://cdiac.esd.ornl.gov/ftp/trends/co2/vostok.icecore.co2> (7-23-07).
- (9) Petit, J. R.; Raynaud, D.; Lorius, C.; Jouzel, J.; Delaygue, G.; Barkov, N. I.; Kotlyakov, V. M. *Historical Isotopic Temperature Record from the Vostok Ice Core*. <http://cdiac.esd.ornl.gov/ftp/trends/temp/vostok/vostok.1999.temp.dat> (7-23-07).
- (10) Raupach, M. R.; Marland, G.; Ciais, P.; Le Quere, C.; Canadell, J. G.; Klepper, G.; Field, C. B. *Proceedings of the National Academy of Sciences of the United States of America* **2007**, *104*, 10288.
- (11) Hoffert, M. I.; Caldeira, K.; Jain, A. K.; Haites, E. F.; Harvey, L. D. D.; Potter, S. D.; Schlesinger, M. E.; Schneider, S. H.; Watts, R. G.; Wigley, T. M. L.; Wuebbles, D. J. *Nature* **1998**, *395*, 881.
- (12) U.S. Census Bureau, *International Data Base (IDB)—World Population*. <http://www.census.gov/ipc/www/worldpop.html> (7-22-07).
- (13) Central Intelligence Agency. *The World Factbook: World*, <https://www.cia.gov/library/publications/the-world-factbook/print/xx.html> (7-23-07).
- (14) Green, C., (private communication).
- (15) International Monetary Fund, *World Economic Outlook Database (April 2007 Edition)*. <http://www.imf.org/external/pubs/ft/weo/2007/01/data/index.aspx> (7-22-07).
- (16) BP, *BP Statistical Review Historical Data*. <http://www.bp.com/multipleimagesection.do?categoryId=9017892&contentId=7033503> (7-22-07).

(17) No self-consistent data sets are available from 1980 through 2006. The most recent data set, through 2006, only goes back to 1990. From 2000-2006, this data shows f increasing at a rate of 0.48%.

(18) Houghton, J. T.; Callander, B. A.; Varney, S. K., Eds. *Climate change 1992 : the supplementary report to the IPCC scientific assessment 1992*, Cambridge University Press.

(19) Goldemberg, J.; Johansson, T. B., Eds. *World Energy Assessment: Overview 2004 Update 1992*, United Nations Development Programme, 2004.

(20) California Energy Commission, *Comparative Costs of Electricity Generation by Resource Type*. [http://www.energy.ca.gov/electricity/comparative\\_costs.html](http://www.energy.ca.gov/electricity/comparative_costs.html) (8-5-07).

(21) Department of Energy, Energy Information Administration. *Electric Power Annual 2005 2006*.

(22) Physorg.com *Team sets solar cell record*. <http://www.physorg.com/news104501218.html> (8-5-07).

(23) BP, *BP Statistical Review Historical Data*. <http://www.bp.com/multipleimagesection.do?categoryId=9017892&contentId=7033503> (7-22-07).

(24) Department of Energy, Carbon Dioxide Information Analysis Center, *Global, Regional, and National Fossil Fuel CO<sub>2</sub> Emissions, 2004*; Carbon Dioxide Information Analysis Center, Environmental Sciences Division, Oak Ridge National Laboratory, U.S. Department of Energy.

## CHAPTER 2

### *Operating Principles of Photoelectrochemical Cells for Solar Energy Conversion*

#### 2.1 INTRODUCTION

Photoelectrochemical cells are the most efficient method known for converting solar energy into chemical fuel. They are simple to assemble, and typically involve nothing more than two electrodes—one a semiconductor and the other a metal—immersed in an electrolyte solution and exposed to light. Furthermore, these cells are flexible in how they can be used: a regenerative photoelectrochemical cell absorbs light to generate electricity with no net chemical change; a photoelectrosynthetic cell uses light to drive a reaction and produce a chemical fuel with greater energy content than the reactants. Such systems are very effective at converting sunlight into electrical and/or chemical energy. Finally, the greatest advantage of photoelectrochemical cells may well be their relatively low cost. As discussed in Chapter 1, one of the greatest impediments to the widespread implementation of solar power is their comparatively high cost, in particular when compared with established and abundant fuels such as coal and oil. It is in this context that photoelectrochemical cells have recently regained much attention in the scientific community.

## 2.2 PHOTOCHEMISTRY OF SEMICONDUCTOR-LIQUID JUNCTIONS

### 2.2.1 Overview

Before addressing the specific mechanisms that allow photoelectrochemical cells to convert into usable energy, it is instructive to first differentiate these cells from the two other known ways that light can be used to produce energy, shown schematically in Figure 2.1. By far the largest production of energy on Earth from any source is photosynthesis, which is nature's method of solar energy conversion. This series of chemical reactions occurring in plants is ultimately responsible for the production of nearly all of the chemical fuels that support life on this planet. Globally, the energy produced by plants through photosynthesis dwarfs the already colossal amount of energy produced by humans by nearly a factor of ten. However, photosynthesis is only capable of forming fuels, and it does this at relatively low efficiency (a comparison of the amount of total incident solar energy that is stored as Gibbs free energy).

In contrast, photovoltaic cells are solid-state devices that convert light into electricity only. Photovoltaic cells can be extremely efficient, converting up to nearly 50% of all incident sunlight into electrical energy in state-of-the-art systems.<sup>1</sup> In their simplest form, these devices consist of two materials that are connected at a well-defined junction. As with photoelectrochemical cells, it is the formation of a junction that provides the directionality necessary to move net charges in a single direction through an external circuit. For photovoltaic cells, this junction is most often between either two semiconductor materials or a semiconductor and a metal.

Photoelectrochemical cells lie somewhere between photosynthesis and photovoltaics in many respects. Photosynthesis is not particularly efficient, but its cost is very low; photovoltaics are exceedingly efficient, and in many cases prohibitively expensive. Photoelectrochemical cells are far more efficient at energy conversion than photosynthesis, and much cheaper than photovoltaics. While photosynthesis is limited to production of fuels and photovoltaics to electricity, photoelectrochemical cells can produce either. Like photovoltaic cells, they rely on the formation of a junction of a semiconductor with another material, but in this case a liquid.

In any system capable of converting light into chemical or electrical energy, four essential processes must occur: 1) absorption of light; 2) creation of free charge carriers; 3) separation of charges; and finally 4) collection of charges, either in the form of electrical current or to drive a desired endothermic chemical reaction.

### 2.2.2 Factors that Determine Overall Conversion Efficiency of a Solar Cell

The overall conversion efficiency of a solar cell,  $\eta$ , is determined by the maximum amount of electrical power produced,  $P_{max}$ , divided by the amount of incident solar power per unit area,  $P_{in}$ :

$$\eta = \frac{P_{max}}{P_{in}} \cdot 100 = \frac{J_{sc} V_{oc} ff}{P_{in}} \cdot 100 . \quad 2.1$$

This is also commonly written in terms of the short-circuit current density,  $J_{sc}$ , the open-circuit voltage,  $V_{oc}$ , and  $ff$ , the so-called fill factor, which is simply defined as  $P_{max}/(J_{sc}V_{oc})$ . The overall performance of solar cells is typically determined by measurement of the current density vs potential ( $J$ - $E$ ) characteristics of the device. The  $J$ - $E$  behavior of a generic photoanodic semiconductor-liquid junction is shown in Figure 2.2, indicating the positions of  $P_{max}$ ,  $J_{sc}$ , and  $V_{oc}$ .

The magnitude of  $J_{sc}$  is determined by the product of the efficiency of optical absorption and of charge collection and the solar irradiance, integrated over all wavelengths of the spectrum of the incident light:

$$J_{sc} = \int (1 - 10^{-Abs(\lambda)}) \cdot IQY(\lambda) \cdot \Phi(\lambda) d\lambda, \quad 2.2$$

where  $Abs(\lambda)$  is the absorbance of the light-collecting species as a function of the wavelength,  $\lambda$ ,  $IQY(\lambda)$  is the internal quantum yield for charge collection, and  $\Phi(\lambda)$  is the irradiance spectrum. This explains why wide-band semiconductors such as  $TiO_2$ , when used alone in a photoelectrochemical cell, produce very low photocurrents: there is simply too little overlap between the absorption spectrum of  $TiO_2$  and the solar spectrum.

For a typical photoelectrochemical cell,  $V_{oc}$  is determined by the difference in energy of the electron at the working electrode (the semiconductor) and the counter electrode (a metal). More precisely, this is the difference in energy of the quasi-Fermi level of the  $TiO_2$  under illumination and the Nernst potential of the electrolyte solution,  $E(A/A^-)$ . For a real working photoelectrochemical cell, the  $ff$  is determined by a complex combination of factors, including the internal resistance of the cell and diffusion rates through the electrolyte solution. Therefore, to optimize the overall conversion efficiency of any solar cell, all of these parameters must be simultaneously considered.

Any highly efficient single-absorber solar cell must be able to absorb a maximum amount of incident sunlight and convert all absorbed photons to collected electrons. For a semiconducting absorber, optimally, all light above a certain energy threshold, corresponding to the band gap energy,  $E_g$ , is absorbed. However, while a lower value of  $E_g$  permits a larger number of photons to be absorbed (see Figure 2.3), the excess energy of all photons with energy above this threshold is lost to heat. There is therefore a trade-

off between materials capable of producing large voltages, but which cannot generate much current, and those that absorb nearly all incident sunlight but only produce a small photovoltage. Based on calculations by C. H. Henry,<sup>2</sup> the optimal band-gap for a single-junction device on the surface of the Earth is thus 1.35 eV, resulting in a maximum possible efficiency for a single junction device of 31%.

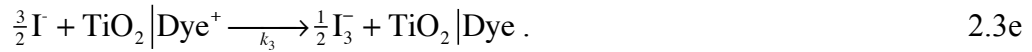
One method by which semiconductors with band gaps too large for absorption of terrestrial sunlight can be used is dye sensitization. This approach allows for the use of a variety of materials not otherwise suitable for use in photoelectrochemical cells by extending their light-absorption properties to lower energies. The key features and operating principles of dye-sensitized solar cells are described in the following section.

## **2.3 DYE-SENSITIZED SOLAR CELLS**

### **2.3.1 Overview**

Dye-sensitized solar cells (DSSCs) offer particular promise as an efficient, low-cost alternative to single-crystal semiconductor photovoltaic devices and represent a specific type of photoelectrochemical cell. The advantages of DSSCs are that they do not rely on expensive or energy-intensive processing methods and can be printed on flexible substrates using roll-to-roll methods. Rather than using a single crystal semiconductor, DSSCs rely on a thin mesoporous film (10–15  $\mu\text{m}$  thick) of nanocrystals of a metal oxide, most often  $\text{TiO}_2$ , which is sensitized to visible light with a molecular light absorber. The sensitized nanoparticles are immersed in a redox-active electrolyte solution to produce a regenerative photoelectrochemical cell (see Figure 2.4). Overall energy conversion efficiencies of over 11% have been demonstrated under Air Mass

(AM) 1.5 conditions.<sup>3</sup> The large surface area of the nanoparticles, which is as much as a factor of 1000 greater than the geometric area of the film, allows a monolayer of surface-bound dye to absorb nearly all of the incident sunlight in the region of the spectrum where the dye absorbs. The structure and absorption spectrum of a typical dye are shown in Figure 2.5. The sensitized TiO<sub>2</sub> nanoparticles are immersed in an electrolyte solution, typically containing the iodide-triiodide redox couple. The basic sequence of events in a DSSC is as follows:



Upon absorption of light, an electron is injected from a metal-to-ligand charge transfer (MLCT) excited state of the dye into the conduction band of the metal oxide. The rate of this electron injection reaction is ultrafast, typically occurring on the order of hundreds of femtoseconds to tens of picoseconds. The injected electron percolates through the TiO<sub>2</sub> film, and is thought to move by a “hopping” mechanism and is driven by a chemical diffusion gradient (rather than an electric field), and is collected at a transparent conductive substrate of fluorine-doped tin oxide glass (SnO<sub>2</sub>:F), on which the TiO<sub>2</sub> film is printed. After passing through an external circuit, the electron is reintroduced into the solar cell at the platinum counter electrode, where triiodide is reduced to iodide. The

iodide then regenerates the oxidized dye, thereby completing the circuit with no net chemical change.

Additionally, deleterious back reactions compete with these forward reactions:



Once the electron is injected into  $\text{TiO}_2$ , it can recombine with the oxidized form of the dye with rate constant  $k_4$  (Equation 2.4a). The injected electron can also recombine with the oxidized form of the redox couple in solution with rate constant  $k_5$  (Equation 2.4b). This back reaction currently represents a significant limitation to the overall conversion efficiency of the cell.<sup>4</sup> Other pathways, such as deactivation of the excited of the dye by species in solution<sup>5,6</sup> have been shown to occur.

### 2.3.2 Challenges to Further Improvement

Unlike the photoelectrochemical cells described in Section 2.2.2, in which absorption of light is due to band gap excitation of electrons in the semiconductor itself, for a DSSC light absorption corresponds to a more localized molecular transition because of the lower density of states of the molecular sensitizer. The energy of this transition corresponds to the difference in the energy of the highest occupied molecular orbital (HOMO) and the lowest unoccupied molecular orbital (LUMO) of the sensitizer. For maximum current generation in a DSSC, it is thus essential that the sensitizer absorb over as wide a range of wavelengths as possible, with an absorption coefficient as large as possible, with a HOMO-LUMO gap optimized to best overlap with the solar irradiation spectrum.

However, even the most efficient DSSCs do not absorb a significant number of photons at energies less than 1.7 eV (750 nm), and do not reach maximum conversion efficiencies for photons less than 2.1 eV (600 nm). Furthermore, the  $V_{oc}$  of even the most efficient devices is under 900 mV, and so on the order of one volt of energy is lost to heat. To increase the overall conversion efficiency, this problem has been attacked from both ends: the absorption spectrum of the dye has been extended to longer wavelengths while still maintaining efficient electron transfer, and  $V_{oc}$  has been maximized by minimizing the thermodynamic driving force for both electron injection into the  $TiO_2$  conduction band and dye regeneration by the redox couple in solution.

Another significant limitation of DSSCs to date has been the relatively low number of choices for the contacting phase. For one, the redox couple  $I^-/I_3^-$  has proven to be quite unique: no other redox couples have been found to date that result in higher cell performance, and only one gives even comparable overall conversion efficiencies.<sup>7</sup> Secondly, the use of liquid electrolyte is not ideal for commercial applications (especially the common use of acetonitrile derivatives as the solvent), due to problems with sealing, volatility, and toxicity. A solid-state device has several advantages, but short of that, a gel, polymeric, or aqueous electrolyte would present a substantial improvement. However, no viable alternative to the use of a volatile organic solvent has been found to date.

Another important question in the study of DSSCs is how to maximize the photovoltage of the cell without any loss in photocurrent. To fully understand the thermodynamics of this aspect of the solar cell, four quantities must be known: the redox potential of the electrolyte solution, the ground state and the excited state reduction

potentials of the dye, and the conduction band edge energy. While the solution potential is easily measured, the other three values are, in fact, not straightforward to measure directly or calculate. Furthermore, the operation of DSSCs depends on favorable kinetics, such that forward current-generating mechanisms occur much faster than their reverse deleterious processes. Characterizing the interplay of photocurrent and photovoltage in working solar cells requires a number of both steady-state and time-resolved experimental methods.

### **2.3.3 Mechanisms and Models**

#### *2.3.3.1 Photovoltage*

The maximum theoretic photovoltage of the cell is given by the difference in energy of the solution potential of the redox couple in the electrolyte and the quasi-Fermi level of TiO<sub>2</sub> under illumination. While this is simple in theory, in practice maximizing the photovoltage and photocurrent simultaneously is extremely complex, with numerous interrelated and sometimes contradictory requirements that all must be individually optimized. To understand this interplay, each step in series of events that produce photocurrent must be considered.

As mentioned above, based on the solar irradiation spectrum on the surface of the earth and thermodynamic constraints on any single-absorber device, the optimum band gap for a single band-gap photovoltaic device is 1.35 eV, or 920 nm. This presents the first limitation on the attainable photovoltage of any optimized DSSC: the absorption spectrum of the dye should ideally absorb strongly in the near-IR. Once the dye absorbs a photon, two electron transfer reactions must occur in order to convert the photon into a free electron: 1) the electron must be injected into the conduction band of TiO<sub>2</sub>; and 2)

following this oxidation of the dye, the ground state of the dye must be regenerated by reduction by a reducing agent in the contacting phase. Both of these electron transfer reactions require some non-zero driving force for them to proceed with any appreciable rate. Therefore the potential of the contacting phase must be more negative (above) than the ground state potential of the dye, and the energy of the conduction band edge must be more positive (below) than that of the excited state of the dye. Necessarily then, the maximum photovoltage of the cell will be less than the HOMO-LUMO gap of the dye by at least the sum of the driving forces for each of these reactions. Unlike conventional photovoltaic devices however, DSSCs do not rely on a built-in electric field at the interface for charge separation, and so such a drop does not need to be considered when calculating the maximum attainable  $V_{oc}$ . Instead, the actual measured photovoltage will be limited by several other factors: deleterious recombination reactions, such as electron loss from either FTO or  $TiO_2$  to either the oxidized dye or any electron acceptors in the electrolyte; any potential drop at the FTO- $TiO_2$  interface; and any over-potential required for electron transfer reactions at either the  $TiO_2$  working electrode or Pt counter electrode.

As can be seen from this list of factors, both thermodynamic as well as kinetic constraints determine the actual photovoltage of a working DSSC. Ideally, one would be able to optimize each of these parameters independently, but in practice this is essentially impossible. Nonetheless, much progress has been made in understanding how to control the key parameters underlying each of the electron transfer reactions in DSSCs. In the following sections, we will focus these parameters in greater detail.

### 2.3.3.2 *Electron Injection*

The factors that determine the rate of electron injection from the excited state of the sensitizer have been studied in detail and for a variety of systems. Although some discrepancies exist in the experimental data reported by different authors, it is universally acknowledged that electron injection from the excited state of the sensitizer into the conduction band of TiO<sub>2</sub> occurs on the ultrafast timescale.<sup>8-21</sup> For the most commonly used Ru-based sensitizers, following optical excitation of approximately 2.3 eV (535 nm) an MLCT state is formed essentially instantaneously with singlet character (<sup>1</sup>MLCT), and this Franck-Condon state will most likely have some degree of vibrational excitation. Several de-excitation pathways are available to this <sup>1</sup>MLCT state, presumably in kinetic competition with one another: 1) the non-thermalized or vibrationally hot excited state injects an electron into an acceptor state in TiO<sub>2</sub> (a conduction band state or trap state) in what is thought to be an isoenergetic reaction; 2) intersystem crossing (ISC) forms a vibrationally excited triplet state (<sup>3</sup>MLCT), which either injects an electron or thermalizes through internal vibrational relaxation (IVR); 3) the thermalized <sup>3</sup>MLCT state injects an electron into TiO<sub>2</sub>; or finally 4) the <sup>3</sup>MLCT state is deactivated to the ground state if electron injection is not competitive with radiative decay or other quenching processes. Ultrafast transient absorption measurements indicated that injection from the initially formed <sup>1</sup>MLCT state occurs within ~ 20 fs, and that ISC is very efficient and occurs within ~ 30 fs, with the rise of the signal associated with the thermalized <sup>3</sup>MLCT state occurring in ~ 100 fs.<sup>17</sup> The thermalized <sup>3</sup>MLCT state has been observed to inject from

anywhere from 1 to 100 ps.<sup>14</sup> These results indicate that electron injection can occur from the initially formed state, and so it is possible for a dye with a excited state reduction potential below the conduction band edge to still inject electrons if excited by sufficiently high-energy photons. This feature is of key importance as it implies that a high photocurrent could still be maintained in a system in which the conduction band edge energy was more negative than the thermalized excited state of the dye. This will be discussed in greater detail in Chapter 4.

Another aspect of electron injection in DSSCs that is not fully understood is the exact nature of the acceptor state(s) in TiO<sub>2</sub>. This again has important implications for understanding the energy requirements of the dye excited state relative to the TiO<sub>2</sub> conduction band. When considering injection into the conduction band itself, the density of states near the band edge is in fact significantly lower than at more negative energies. If the injection process itself is isoenergetic, and thus driven entropically, the larger density of states at higher energies will result in faster injection rates at higher energies—and this is exactly what is observed. Injection rates measured after excitation at 455-nm light were found to be significantly faster than those following excitation at 530 nm.<sup>17</sup> It is also possible that the electron is injected into trap states in the TiO<sub>2</sub>. If a sufficient density of traps states is found below the conduction band edge, injection may still be possible, even if the band edge energy is more negative than the excited state energy. It is less clear if these injected electrons would result in photocurrent when under steady-state illumination, however. In order to be collected at the back substrate, these electrons would either have to move through the TiO<sub>2</sub> film by a “hopping” mechanism from trap

state to trap state, or else they would need to be promoted by thermal energy to the conduction band.

### 2.3.3.3 *Dye Reduction*

After injection, the oxidized metal center of the dye must be generated back to the reduced ground state to complete the circuit with no net chemical change. The rate of this reaction must exceed that of the recombination reaction with injected electrons from TiO<sub>2</sub>, so as to maintain a high photocurrent and prevent decomposition of the dye. Using a series of dyes with varying ground state reduction potentials, Kuciauskas et al. found that the sensitizer with the least positive potential was not efficiently reduced by iodide, due to insufficient driving force for the reaction,<sup>22</sup> and that this led to overall poor conversion efficiencies in working solar cells.<sup>23</sup> A difference of 0.23 V in the ground state redox potential was thus correlated with a factor-of-five drop in photocurrent. This illustrates the delicate balance that must be achieved between minimizing the thermodynamic driving force for the forward electron transfer reactions and maintaining favorable kinetics for photocurrent generation.

The reaction rate for the reduction reaction can be written as:

$$\text{rate} = k_3 [\text{Dye}^+] [\text{I}^-]^x. \quad 2.5$$

The value of  $x$ , the order of the reaction in I<sup>-</sup>, has been found to be one, despite the possibility of a higher-order reaction implied by Equation 2.3e, with rate constants on the order of 10<sup>5</sup> dm<sup>3</sup> mol<sup>-1</sup> sec<sup>-1</sup>.<sup>22,24,25</sup> Furthermore, it was found that under high concentrations of iodide such that [Dye<sup>+</sup>] << [I<sup>-</sup>], the overall reaction order is pseudo-first order, independent of the reaction order with respect to iodide.

#### 2.3.3.4 *Electron Loss or Electrolyte Recombination*

One of the least well-understood aspects of DSSCs is the slow rate of electron transfer from  $\text{TiO}_2$  to hole carriers in solution. Unlike single-crystal semiconductor-liquid junctions in which a space-charge region is formed at the interface due to equilibration of the Fermi level of the two phases,<sup>26</sup> in nanocrystalline DSSCs no space-charge region exists.<sup>27,28</sup> Therefore, no electric field exists at the interface to reduce the rate of this back reaction. Given the extremely high surface area of the  $\text{TiO}_2$  nanocrystals and the lack of interfacial electric field, it is essential that the reaction kinetics of the reduction of redox species in solution be slow compared to the rate of electron percolation through the  $\text{TiO}_2$  film. To a large extent, this stringent kinetic requirement has frustrated efforts to replace the  $\text{I}^-/\text{I}_3^-$  redox couple with an alternative. For instance, replacement of  $\text{I}^-/\text{I}_3^-$  with the ferrocene/ferrocenium ( $\text{Fc}/\text{Fc}^+$ ) couple, which has a similar formal potential, results in a completely non-functioning DSSC, because every injected electron in  $\text{TiO}_2$  is lost to the reduction of ferrocenium before it can be collected at the back contact. This effectively short-circuits the DSSC internally. The exact nature of the reaction of electrons in  $\text{TiO}_2$  with  $\text{I}^-/\text{I}_3^-$  is not fully understood, and this has made finding a suitable replacement all the more difficult.

## 2.4 CONCLUSIONS

Photoelectrochemical cells are an extremely promising technology for solar energy conversion on a large scale. Their low cost and ability to generate chemical fuels makes them a very attractive alternative to photovoltaics. However, there remain a

number of challenges to overcome before such systems can be implemented on the scale required to provide a viable alternative to fossil fuels.

Dye-sensitized solar cells are a unique type of photoelectrical cell with great promise as an efficient, low-cost solar energy conversion device. Despite a great deal of research on these systems, numerous fundamental questions are as yet unanswered about the basic physical and chemical principles responsible for their operation. The following two chapters, one using steady-state techniques and the second using time-resolved methods, represent an effort to understand on a very fundamental level how these cells work in a systematic way, such that further improvements in conversion efficiency can be designed. The delicate balance between optimal kinetics for forward electron transfer and maximizing the open-circuit voltage is elucidated by variation of the energy of states in the TiO<sub>2</sub> and probed using a variety of photoelectrochemical techniques.

In the final chapter, a different approach to the field of solar energy research is described. Here, new materials are synthesized and tested in a photoelectrosynthetic cell. A combinatorial method is developed to explore as many new metal oxides as possible to identify materials that can split water to form H<sub>2</sub> and O<sub>2</sub> gas with sunlight. As there is currently not even a remotely accurate predictive theoretical understanding of what determines the photoelectrochemical properties of mixed-metal oxides or why a given material should or should not be an effective electrode for the photoelectrolysis of water, the goal was to develop a robust system for generating and testing new materials. The proof-of-concept experiments presented in this final chapter demonstrate the additional information and insight gained by measuring the photovoltage of the synthesized mixed metal oxides.

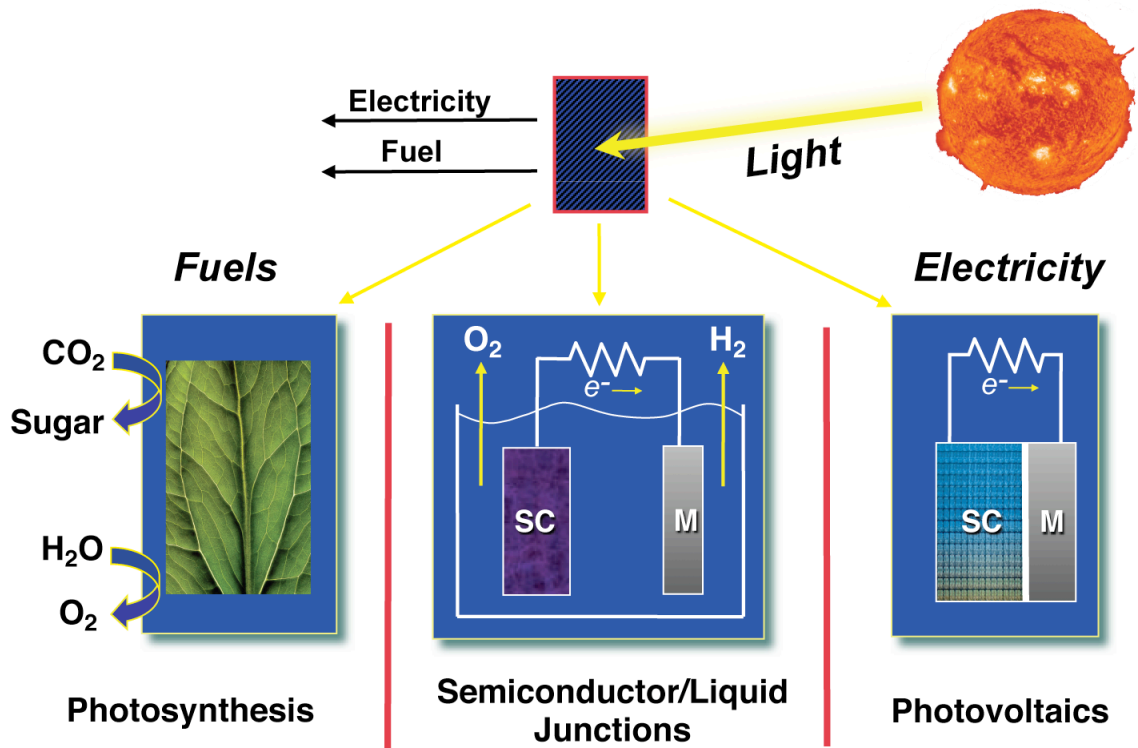


**Figure 2.1** The three known methods by which solar energy can be converted into usable chemical and/or electrical energy

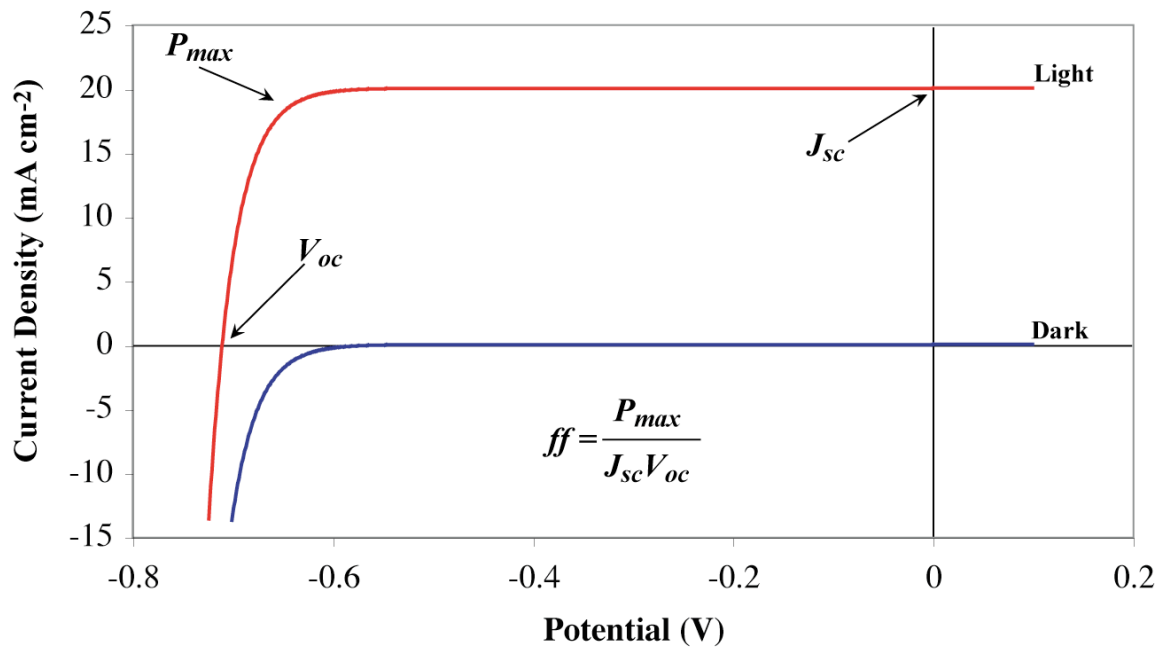


**Figure 2.2** Typical  $J$ - $E$  behavior of a solar cell, generated by measuring the current as an applied potential is scanned between the working and counter electrodes

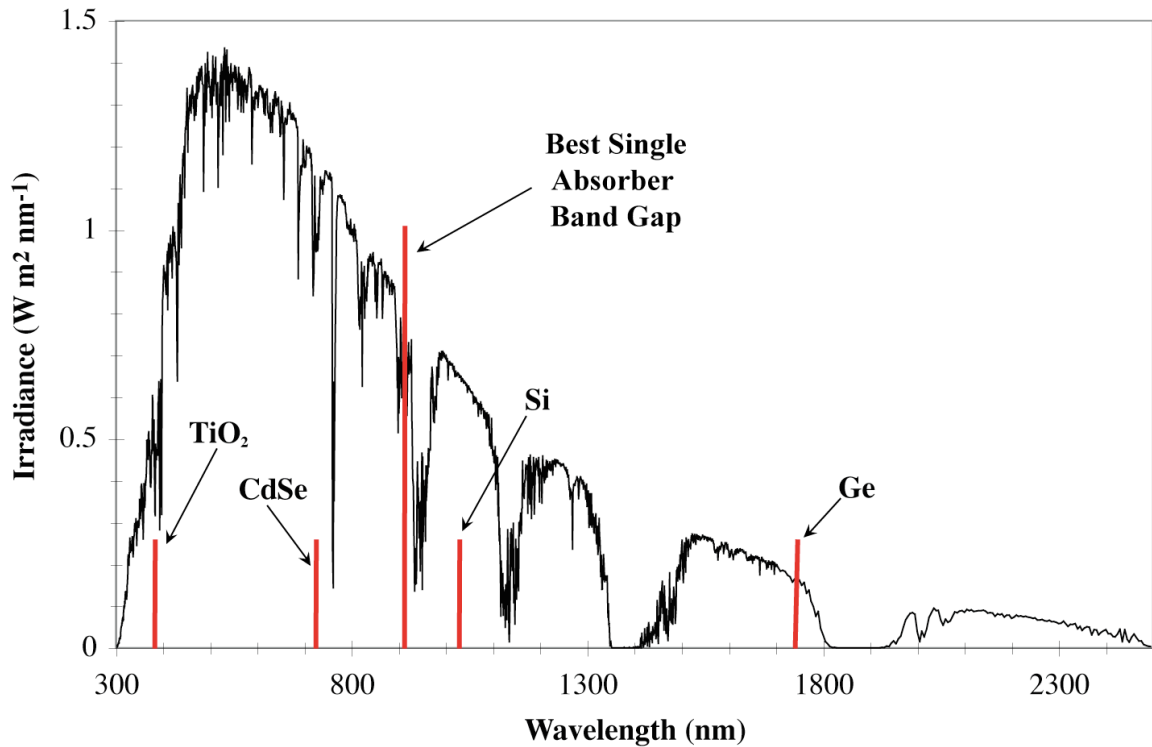


**Figure 2.3** Solar irradiance spectrum on the surface of the earth under standard Air Mass (AM) 1.5 conditions, or when the sun is 48° above the horizon. The energy of the band gap,  $E_g$ , of several common semiconductors are shown for comparison. Because of the threshold behavior of optical absorption, light will only be absorbed at energies higher than, or to the left, of the indicated band gap. Thus, a semiconductor such as Ge will absorb the large majority of incident sunlight, while a wide band gap semiconductor such as TiO<sub>2</sub> will absorb the very small percentage because of the near-absence of UV light in terrestrial sunlight. The optimal band gap of 1.35 eV for a single semiconducting absorber is indicated.

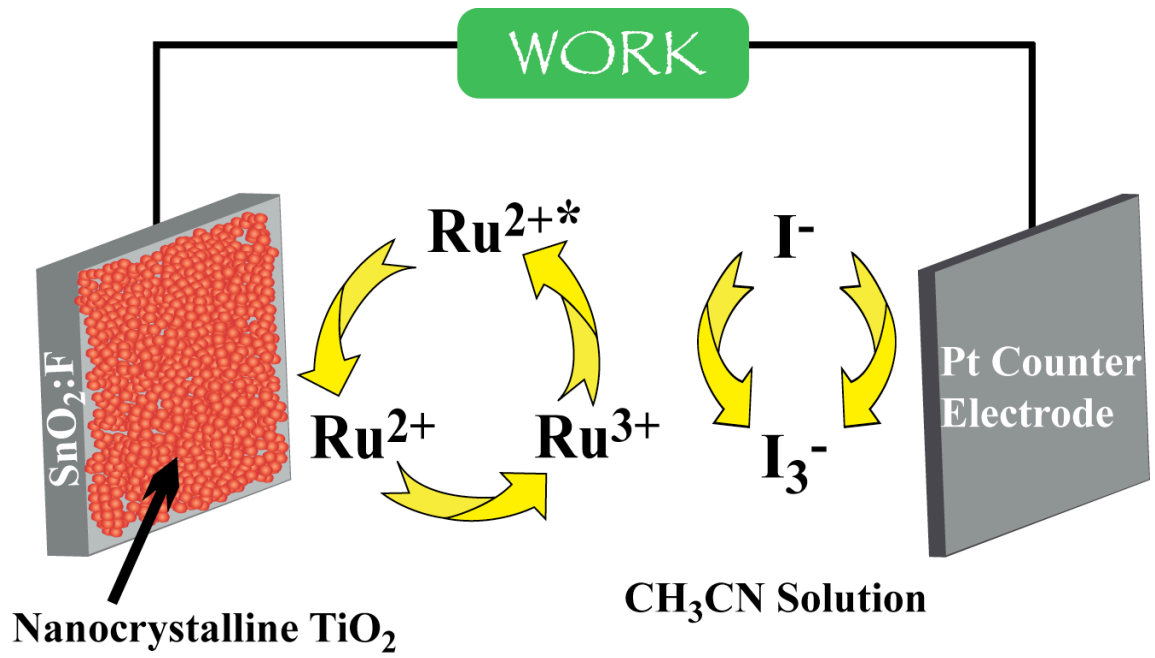


**Figure 2.4** Schematic diagram of a typical  $\text{TiO}_2$ -based dye-sensitized solar cell

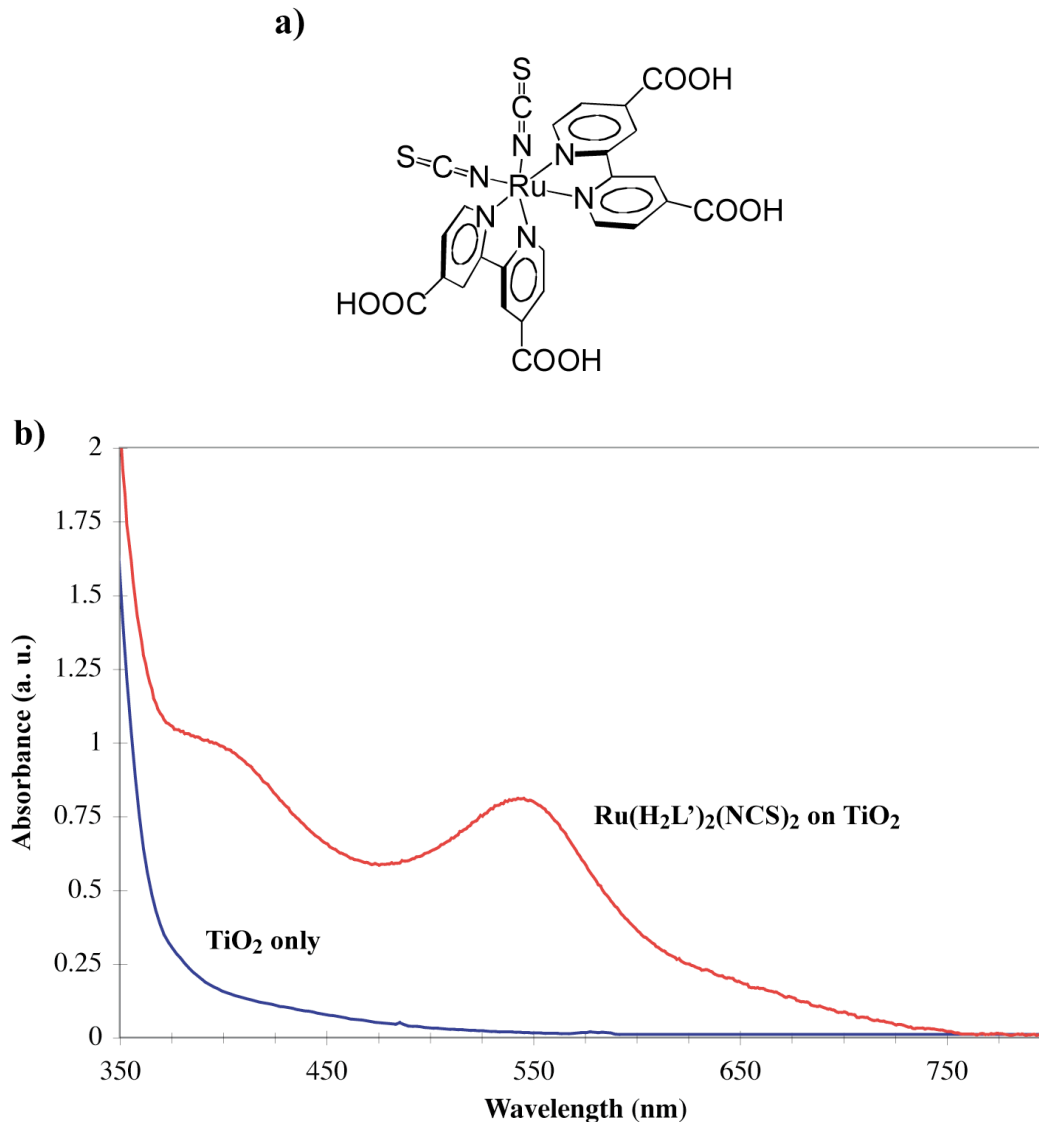


**Figure 2.5** (a) Structure of a commonly used ruthenium-based sensitizer,  $\text{Ru}(\text{H}_2\text{L}')_2(\text{NCS})_2$ , where  $\text{H}_2\text{L}'$  is 4,4'-dicarboxylic acid-2,2'-bipyridine, commonly known as the N3 dye. (b) Absorption spectrum of  $\text{Ru}(\text{H}_2\text{L}')_2(\text{NCS})_2$  bound to a nanocrystalline  $\text{TiO}_2$  film, compared to the bare un-sensitized film. The onset absorption of the bare film corresponds to the band gap of 3.2 eV, while lower energy tail is due to light scattering off the porous film.

## REFERENCES

- (1) Team sets solar cell record. Physorg.com **2007**.
- (2) Henry, C. H. *J. Appl. Phys.* **1980**, *51*, 4494.
- (3) Gratzel, M. *Inorg. Chem.* **2005**, *44*, 6841.
- (4) Green, A. N. M.; Chandler, R. E.; Haque, S. A.; Nelson, J.; Durrant, J. R. *J. Phys. Chem. B* **2005**, *109*, 142.
- (5) Clark, C. C.; Marton, A.; Srinivasan, R.; Sarjeant, A. A. N.; Meyer, G. J. *Inorg. Chem.* **2006**, *45*, 4728.
- (6) Marton, A.; Clark, C. C.; Srinivasan, R.; Freundlich, R. E.; Sarjeant, A. A. N.; Meyer, G. J. *Inorg. Chem.* **2006**, *45*, 362.
- (7) Nusbaumer, H.; Moser, J. E.; Zakeeruddin, S. M.; Nazeeruddin, M. K.; Gratzel, M. *J. Phys. Chem. B* **2001**, *105*, 10461.
- (8) Hannappel, T.; Burfeindt, B.; Storck, W.; Willig, F. *J. Phys. Chem. B* **1997**, *101*, 6799.
- (9) Takeshita, K.; Sasaki, Y.; Kobashi, M.; Tanaka, Y.; Maeda, S. *J. Phys. Chem. B* **2003**, *107*, 4156.
- (10) Kuciauskas, D.; Monat, J. E.; Villahermosa, R.; Gray, H. B.; Lewis, N. S.; McCusker, J. K. *J. Phys. Chem. B* **2002**, *106*, 9347.
- (11) Kallioinen, J.; Benko, G.; Sundstrom, V.; Korppi-Tommola, J. E. I.; Yartsev, A. P. *J. Phys. Chem. B* **2002**, *106*, 4396.

- (12) Asbury, J. B.; Ellingson, R. J.; Ghosh, H. N.; Ferrere, S.; Nozik, A. J.; Lian, T. Q. *J. Phys. Chem. B* **1999**, *103*, 3110.
- (13) Heimer, T. A.; Heilweil, E. J.; Bignozzi, C. A.; Meyer, G. J. *J. Phys. Chem. A* **2000**, *104*, 4256.
- (14) Benko, G.; Kallioinen, J.; Myllyperkio, P.; Trif, F.; Korppi-Tommola, J. E. I.; Yartsev, A. P.; Sundstrom, V. *J. Phys. Chem. B* **2004**, *108*, 2862.
- (15) Asbury, J. B.; Anderson, N. A.; Hao, E. C.; Ai, X.; Lian, T. Q. *J. Phys. Chem. B* **2003**, *107*, 7376.
- (16) Kallioinen, J.; Benko, G.; Myllyperkio, P.; Khriachtchev, L.; Skarman, B.; Wallenberg, R.; Tuomikoski, M.; Korppi-Tommola, J.; Sundstrom, V.; Yartsev, A. P. *J. Phys. Chem. B* **2004**, *108*, 6365.
- (17) Benko, G.; Kallioinen, J.; Korppi-Tommola, J. E. I.; Yartsev, A. P.; Sundstrom, V. *J. Am. Chem. Soc.* **2002**, *124*, 489.
- (18) Tachibana, Y.; Haque, S. A.; Mercer, I. P.; Moser, J. E.; Klug, D. R.; Durrant, J. R. *J. Phys. Chem. B* **2001**, *105*, 7424.
- (19) Tachibana, Y.; Haque, S. A.; Mercer, I. P.; Durrant, J. R.; Klug, D. R. *J. Phys. Chem. B* **2000**, *104*, 1198.
- (20) Asbury, J. B.; Hao, E.; Wang, Y. Q.; Ghosh, H. N.; Lian, T. Q. *J. Phys. Chem. B* **2001**, *105*, 4545.
- (21) Kallioinen, J.; Lehtovuori, V.; Myllyperkio, P.; Korppi-Tommola, J. *Chem. Phys. Lett.* **2001**, *340*, 217.
- (22) Kuciauskas, D.; Freund, M. S.; Gray, H. B.; Winkler, J. R.; Lewis, N. S. *J. Phys. Chem. B* **2001**, *105*, 392.

- (23) Sauve, G.; Cass, M. E.; Coia, G.; Doig, S. J.; Lauermann, I.; Pomykal, K. E.; Lewis, N. S. *J. Phys. Chem. B* **2000**, *104*, 6821.
- (24) Pelet, S.; Moser, J. E.; Gratzel, M. *J. Phys. Chem. B* **2000**, *104*, 1791.
- (25) Montanari, I.; Nelson, J.; Durrant, J. R. *J. Phys. Chem. B* **2002**, *106*, 12203.
- (26) Tan, M. X.; Laibinis, P. E.; Nguyen, S. T.; Kesselman, J. M.; Stanton, C. E.; Lewis, N. S. Principles and Applications of Semiconductor Photoelectrochemistry. In *Progress in Inorganic Chemistry, Vol 41* **1994**, 21.
- (27) Zaban, A.; Meier, A.; Gregg, B. A. *J. Phys. Chem. B* **1997**, *101*, 7985.
- (28) Cahen, D.; Hodes, G.; Gratzel, M.; Guillemoles, J. F.; Riess, I. *J. Phys. Chem. B* **2000**, *104*, 2053.

## CHAPTER 3

### *Characterization of the Interfacial Energetics and Steady-State Current Density vs Potential Effects of Electrolyte Cations in Dye-Sensitized Solar Cells*

#### 3.1 INTRODUCTION

Dye-sensitized solar cells (DSSCs) are of interest because they can be fabricated using low-energy techniques and can be made on a variety of supports.<sup>1-9</sup> The large number of chemical events that occur in a functioning DSSC, combined with the individual complexity, as well as the interrelatedness of these chemical processes, requires systematic study to isolate and elucidate the key factors that determine the overall conversion efficiency of such cells. Of specific interest are methods to change the properties of such cells systematically, such as manipulating the interfacial energetics in a controlled fashion. We present here the results of an investigation of the effect of the electrolyte cations on the thermodynamics of the electron-transfer reactions at dye-sensitized nanocrystalline TiO<sub>2</sub> electrodes. The goal of this work was to assess to what extent such methods led to an improved photovoltage, and to assess whether such changes were accompanied by deleterious effects on the photocurrent, or other performance properties, of such cells.

In a typical DSSC, a monolayer of a Ru-based sensitizer or dye is adsorbed onto the surface of a film of nanocrystalline TiO<sub>2</sub>. The sensitizer-coated photoelectrode is then immersed into an electrolyte solution. The surface-bound sensitizer absorbs visible light, producing an excited state generally due to a metal-to-ligand charge-transfer (MLCT) absorption. For Ru(H<sub>2</sub>L')<sub>2</sub>(NCS)<sub>2</sub> as the sensitizer, due to facile electronic coupling between the sensitizer ligand (where the excited state is localized) and the

acceptor states in the TiO<sub>2</sub>, a significant fraction of the photoexcited electrons are injected into the TiO<sub>2</sub> on a femtosecond timescale.<sup>6,10</sup> After percolating through the sintered film of nanoparticles, the injected electrons are collected at a back contact that consists of a transparent layer of conductive, fluorine-doped, SnO<sub>2</sub>. To complete the circuit, I<sub>3</sub><sup>-</sup> in solution is reduced at the Pt counter electrode to form I<sup>-</sup>, which then reacts with the oxidized form of the dye to regenerate the reduced, ground state of the dye.

The maximum energy-conversion efficiency,  $\eta$ , of a semiconductor/liquid junction solar cell is given by the quotient of the maximum electrical power produced relative to the incident solar power:<sup>11</sup>

$$\eta = \frac{(JV)_{\max}}{P_{in}} \cdot 100 = \frac{J_{sc} V_{oc} ff}{P_{in}} \cdot 100, \quad 3.1$$

with  $P_{in}$  the solar power per unit area of incident light, and  $(JV)_{\max}$  the point of maximum power density.  $(JV)_{\max}$  is commonly written as the product of the short-circuit current density ( $J_{sc}$ ), the open-circuit voltage ( $V_{oc}$ ), and the fill factor ( $ff$ ), where  $ff$  is defined as  $J_{sc}V_{oc}/(JV)_{\max}$ . Design of highly efficient devices thus requires that the photovoltage, photocurrent and fill factor all be optimized simultaneously.

For a semiconductor/liquid junction solar cell, the theoretical upper bound on the open-circuit voltage is related to the difference between the Nernst potential of the solution,  $E(A/A^-)$ , and the potential of the bottom of the conduction band of the semiconductor (positive energies).<sup>12,13</sup> By shifting the conduction-band edge to more negative potentials, the  $V_{oc}$  of a DSSC can, in principle, be increased.<sup>4,5</sup> However, the photocurrent in a DSSC is a function of the ability of the dye to absorb incident sunlight and to have favorable relative kinetics for: 1) electron injection compared to excited-state deactivation; 2) dye regeneration compared to dye decomposition or recombination with injected electrons; and 3) electron collection compared to interfacial reduction of hole carriers in solution. Attempts to increase the photovoltage of a DSSC by changing the position of the conduction-band edge must thus maintain sufficient driving force for

both electron injection and regeneration of the oxidized dye, without significantly affecting the relative rates of electron collection and recombination.

We elucidate herein how thermodynamic constraints affect the photovoltage and photocurrent of a class of functional DSSCs. Decreasing the concentration of the cations  $H^+$  and  $Li^+$  in the contacting electrolyte solution produces significant increases the photovoltage, but is accompanied by a concomitant decrease in the photocurrent. Other studies have shown similar effects, sometimes attributing the increase in photovoltage to band-edge movement,<sup>8,14,15</sup> to surface passivation,<sup>16</sup> to other effects due to dye protonation state,<sup>17</sup> or to surface charging.<sup>18</sup> Accordingly, spectrochronocoulometry was used to measure the band-edge shift under the same conditions used in working solar cells, and this shift has been used to correlate the changes in interfacial energetics to the changes in photovoltages and photocurrents in the DSSCs of concern.

## 3.2 EXPERIMENTAL

### 3.2.1 Materials

Acetonitrile (BakerDRY,  $\geq 99.5\%$  min), acetic acid (AcH) (Aldrich, 99.99%), silver nitrate (Aldrich), lithium iodide (Aldrich, 99.99% beads), and  $Ru(H_2L')_2(NCS)_2$  (Ruthenium 535, Solaronix) were used as received. Lithium perchlorate (Aldrich,  $\geq 95\%$ ) was dried by fusing at 240 °C under vacuum. Tetra(n-butyl)ammonium perchlorate (TBAP) (Aldrich,  $\geq 98\%$ ) was recrystallized from hot ethanol with diethylether, and was dried under vacuum at 130 °C. Tetra(n-butyl)-ammonium iodide (TBAI) (Aldrich, reagent grade) was recrystallized from acetone with ether, and was dried under vacuum at room temperature. Iodine (Aldrich, ReagentPlus) was sublimed at 40 °C. Water was  $> 18\text{ M}\Omega\text{ cm}$  in resistivity, obtained from a Barnsted Nanopure system. All materials were stored in the dark under  $N_2(g)$ , with the exception of  $I_2$ , acetic acid, and  $Ru(H_2L')_2(NCS)_2$ . All electrolytes were prepared under  $N_2(g)$ . The purity of all

electrolyte solutions was confirmed by cyclic voltammetry, with the water content measured by gas chromatography to be  $< 10$  ppm.

### 3.2.2 Fabrication of Photoelectrochemical Cells

Fluorine-doped SnO<sub>2</sub>-coated glass (FTO) (TEC 15, Hartford Glass Co.) was cleaned by first washing with soapy water, then sequentially sonicating and rinsing in organic solvents (hexanes, acetone, methanol, and then isopropanol), and finally blowing dry with N<sub>2</sub>(g). TiO<sub>2</sub> nanoparticles in the form of a screen-printable paste (Ti-nanoxide HTSP) were purchased from Solaronix, and were used as received. Thin films of this nanocrystalline TiO<sub>2</sub> were screen printed (AMI Inc, model HC-53) with a 156 mesh polyester screen, with 10.2 μm of MX emulsion (Sefar Printing). The printed films were dried at 80 °C for several h before sintering at 450 °C for 30 min in air. Profilometry measurements (Dektak 3030) indicated that the final films were  $\approx 5$  μm thick.

Before use, TiO<sub>2</sub> electrodes were pre-treated by immersion overnight into a solution of freshly prepared 0.2 M TiCl<sub>4</sub>(aq). The films were subsequently rinsed with  $> 18$  MΩ cm resistivity H<sub>2</sub>O, and dried with N<sub>2</sub>(g). TiO<sub>2</sub> films were then baked at 450 °C for 30 min, cooled to 120 °C, and immediately immersed in a solution of  $\approx 1 \times 10^{-4}$  M Ru(H<sub>2</sub>L')<sub>2</sub>(NCS)<sub>2</sub> in ethanol (Aaper, 100%). The films were then soaked in the ethanolic dye solution for 12–24 h in the dark.

A 3-electrode configuration, with a Pt mesh counter-electrode, was used for all electrochemical measurements. For cells with a well-defined redox couple (i.e., I/I<sub>3</sub><sup>-</sup>), a Pt wire poised at the Nernstian potential of the cell,  $E(A/A^-)$ , served as the reference electrode. The cell design allowed for replacement of the electrolyte solution without exposing the interior of the cell to air. The surface area of the TiO<sub>2</sub> exposed to the electrolyte was the same as the illuminated area of the cell, which was 0.25 cm<sup>2</sup>. Illumination was through the FTO back contact. UV/visible absorption spectra of sensitized and bare TiO<sub>2</sub> films were measured with an Agilent 8453 spectrometer.

### 3.2.3 Spectrochronocoulometry

Simultaneous chronocoulometry and time-resolved UV/Visible absorption spectroscopy were used to measure the capacitive charging of unsensitized TiO<sub>2</sub> films as a function of the electrode potential. Measurements were performed in a three-electrode photoelectrochemical cell with a Pt-gauze counter electrode. The reference electrode consisted of a Ag wire that was immersed in a CH<sub>3</sub>CN solution that contained  $\approx 50$  mM AgNO<sub>3</sub> and the supporting electrolyte of interest. After each experiment, the potential of the reference electrode was measured vs a methanolic saturated calomel electrode (MSCE). The cell was assembled in a dry box under N<sub>2</sub> atmosphere, sealed, and left to equilibrate in the dark. The cell design allowed for collection of the absorption spectrum of the TiO<sub>2</sub> film while a potential was being applied to the photoelectrode.

A series of potential steps, separated by 100 mV and 30 s each in duration, was applied by a PAR Model 173 potentiostat equipped with a PAR Model 179 digital coulometer. After each step, the photoelectrode was maintained for several min at a potential of 0.4 V vs MSCE. Throughout the potential step sequence, UV/visible absorbance spectra were collected at 2 Hz over a spectral range that spanned 200 to 1100 nm. Optical excitation of TiO<sub>2</sub> due the spectrometer lamp was found to be negligible by comparison with data collected using a 385-nm-long pass filter.

The capacitive charging was determined as a function of electrode potential in both redox-active and redox-inactive electrolytes (I<sup>-</sup>/I<sub>3</sub><sup>-</sup> and ClO<sub>4</sub><sup>-</sup>, respectively) at varying concentrations of TBA<sup>+</sup>, Li<sup>+</sup>, and AcH. For all of measurements, the ionic strength was kept constant at 500 mM. While some Faradaic background processes were observed in all electrolytes, only non-Faradaic (fully reversible) charging was used in the analysis of the data. For the spectrochronocoulometry data, the amount of non-Faradaic charge was deduced by taking the difference of the charge passed at the end of the potential step and the charge remaining after allowing several min for the TiO<sub>2</sub> film to discharge at 0.4 V vs

MSCE. The absorbance change,  $\Delta A$ , was measured by taking the difference of the maximum absorbance and the initial absorbance at wavelengths of 800 nm and 360 nm.

### 3.2.4 Current Density vs Potential Measurements

Current density vs potential data were collected at a scan rate of  $20 \text{ mV s}^{-1}$  under simulated Air Mass (AM) 1.5 solar illumination and in the dark. A 385-nm cutoff filter was used to avoid band-gap excitation of  $\text{TiO}_2$ . The electrolyte was 500 mM  $\text{I}^-$ , 40 mM  $\text{I}_2$  in  $\text{CH}_3\text{CN}$ , with the cation of the  $\text{I}^-$  salt either being  $\text{Li}^+$  or  $\text{TBA}^+$ . In certain cases, 50 mM of acetic acid (AcH) was added as a source of protons.

$J$ - $E$  data were measured over the course of several hours, to evaluate the stability of the photoelectrochemical cells. Reported values were always measured after cells reached stable  $J$ - $E$  values. Under illumination,  $\text{LiI/I}_2$  and  $\text{TBAI/I}_2$  cells required 2–3 h of equilibration before reaching stable values.  $J$ - $E$  curves taken immediately after assembling the cell showed higher  $J_{sc}$  and lower  $V_{oc}$  values (comparable to cells with AcH present), but over the course of several hours,  $J_{sc}$  decreased and  $V_{oc}$  and  $ff$  increased.

An arc lamp (Oriel 66902) with an AM1.5 filter was used at  $100 \text{ mW cm}^{-2}$ , as determined using a calibrated silicon photodiode (Solarex), for quantitative characterization of the performance of the solar cells.

### 3.2.5 Spectral Response

The external quantum yield ( $EQY$ ) was measured from 300 to 800 nm under low-intensity, monochromatic illumination provided by a 50 W Xe arc lamp. The light was passed through a spectrometer (Spex, 1681B) equipped with 5-mm diameter slits. Quartz optics were used to collimate and focus the divergent output beam out of the spectrometer. Illumination was through the FTO back contact. Approximately 10% of the output beam was split off to a reference Si photodiode, and the remainder was directed to the photoelectrochemical cell. The DSSC and diode photocurrents were measured using two Princeton Applied Research (PAR) Model 173 potentiostats. For

calibration, the photoelectrochemical cell was replaced by a calibrated Si photodiode (UDT Sensors, model UV-50). The  $EQY$ s of the DSSC were calculated as follows:

$$EQY_{DSSC}(\lambda) = \frac{I_{DSSC}(\lambda)}{I_{calib}(\lambda)} \frac{I_{ref\ calib}(\lambda)}{I_{ref\ DSSC}(\lambda)} EQY_{calib}(\lambda), \quad 3.2$$

where  $I_{DSSC}(\lambda)$  and  $I_{calib}(\lambda)$  are the short-circuit currents as a function of wavelength of the DSSC and the calibrated photodiodes, respectively, and  $EQY_{calib}(\lambda)$  is the  $EQY$  of the calibrated photodiode.  $I_{ref\ DSSC}(\lambda)$  and  $I_{ref\ calib}(\lambda)$  are the short-circuit currents of the reference photodiode recorded during each measurement for the DSSC and calibrated diode respectively.  $J-E$  data were measured before and after each spectral response measurement, to evaluate changes in photocurrent produced during the spectral response measurements.

### 3.3 RESULTS

#### 3.3.1 Spectrochronocoulometry

The amount of charge electrochemically injected into a  $TiO_2$  film in contact with electrolyte, as a function of applied potential, was determined by chronocoulometry in combination with spectroscopic methods. Faradaic processes contributed a significant amount of charge under all conditions, even when highly purified and anhydrous electrolytes (in the presence of  $TBA^+$ ,  $Li^+$ , or  $H^+$ ) were used. To account for any Faradaic processes during the capacitive charging of the  $TiO_2$  film, all irreversibly passed charge was subtracted from the total charge. Measurement at a series of individual potential steps allowed for this correction to be performed. The degree of capacitive charging calculated by this method,  $Q_{rev}$ , was reproducible and independent of the order in which the series of potential step sequences were applied. Furthermore, measurement of  $Q_{rev}$  at each potential step value allowed this method to also be used in the presence of a redox-active electrolyte.

The number of injected electrons was measured spectroscopically by the increase in absorbance in the near-IR at 800 nm,  $\Delta A_{800\text{nm}}$  (see Figures 3.1a & 3.2a), and also by a negative feature at 360 nm,  $\Delta A_{360\text{nm}}$ , ascribable to a Burstein-Moss shift<sup>19</sup> (Figure 3.1c), simultaneously with collection of the chronocoulometric data (Figures 3.1b & 3.2b). In rigorously purified electrolytes, all changes observed in the absorption spectra were fully reversible as a function of electrode potential.

The band-edge shifts, as measured by both chronocoulometry and by the spectroscopic features at 800 nm and 360 nm, showed that the onset of charging shifted to significantly more negative potentials in the absence of small cations (Figures 3.1 & 3.2). For each measurement method, the charging curves for the series of electrolytes were globally fit to a series of exponential decays of the form  $y_i = a \cdot \exp(-b \cdot (E_{\text{step}} + c_i))$ , where  $y_i$  was  $Q_{\text{rev}}$ ,  $\Delta A_{800\text{nm}}$ , or  $\Delta A_{360\text{nm}}$  for each electrolyte,  $E_{\text{step}}$  was the size of the applied potential step,  $a$  and  $b$  were parameters independent of electrolyte composition and the value of  $c_i$  was taken to be the relative shift in the energy of acceptor states in TiO<sub>2</sub> for a particular electrolyte. The values of  $c_i$  were the same, within experimental error, for all measurement methods (Table 3.1). The shift was also the same within error, regardless of whether the electrolyte contained the redox-inactive ClO<sub>4</sub><sup>-</sup> salt or the I<sup>-</sup>/I<sub>3</sub><sup>-</sup> redox couple.

### 3.3.2 *J-E* Behavior

Figure 3.3 compares the *J-E* behavior of DSSCs with Ru(H<sub>2</sub>L')<sub>2</sub>(NCS)<sub>2</sub> vs the composition of the electrolyte. Cells that contained 500 mM LiI–40 mM I<sub>2</sub>–50 mM AcH produced the highest short-circuit photocurrent densities, and exhibited *J-E* behavior that was stable over the course of several hours. In contrast, cells that contained either 500 mM TBAI–40 mM I<sub>2</sub> or 500 mM LiI–40 mM I<sub>2</sub> (without 50 mM AcH) showed significantly larger values of  $V_{oc}$  and  $ff$ , albeit with lower values of  $J_{sc}$  (Figure 3.3a). This behavior was primarily related to the introduction of acid into the electrolyte, because cells that contained 500 mM TBAI–40 mM I<sub>2</sub>–50 mM AcH exhibited *J-E* behavior that

was essentially identical to that of 500 mM LiI–40 mM I<sub>2</sub>–50 mM AcH cells (data not shown). In contrast, cells with 500 mM Li–40 mM I<sub>2</sub> (without AcH) were more similar to those that contained 500 mM TBAI–40 mM I<sub>2</sub> than Li<sup>+</sup>-based cells that contained AcH. The *J-E* behavior of these various electrolyte combinations is summarized in Table 3.2.

Similar trends were observed in the dark under forward bias (Figure 3.3b). The stabilized cells that did not contain 50 mM AcH exhibited currents at  $E = -600$  mV vs  $E(A/A^-)$  that were as much as a factor of ten less than the currents observed at  $E = -600$  mV vs  $E(A/A^-)$  in cells that also contained 50 mM of AcH (Table 3.2).

The observed changes in the *J-E* behavior were fully reversed upon changing electrolytes from 500 mM TBAI–40 mM I<sub>2</sub> to 500 mM LiI–40 mM I<sub>2</sub>–50 mM AcH. *J-E* data were measured first using 500 mM TBAI–40 mM I<sub>2</sub> (after equilibration), and then a solution of 500 mM LiI–40 mM I<sub>2</sub>–50 mM AcH was flushed through the cell, replacing the initial electrolyte. When the 500 mM LiI–40 mM I<sub>2</sub>–50 mM AcH electrolyte was flushed out with more of the same electrolyte, no change in the *J-E* curves was observed, so any changes observed were related to the composition of the electrolyte. When the electrolytes were replaced in the opposite order (i.e., when 500 mM LiI–40 mM I<sub>2</sub>–50 mM AcH was followed by 500 mM TBAI–40 mM I<sub>2</sub>) the effects were only partially reversed, with the  $V_{oc}$  never reaching the values obtained with 500 mM TBAI–40 mM I<sub>2</sub>.

With 50 mM AcH in the electrolyte, the *J-E* data was unchanged after several hours, whereas cells that contained only 500 mM TBAI–40 mM I<sub>2</sub> or 500 mM LiI–40 mM I<sub>2</sub> required 30–60 min to exhibit constant *J-E* behavior in the dark. For 500 mM TBAI–40 mM I<sub>2</sub> and 500 mM LiI–40 mM I<sub>2</sub> electrolytes, the *J-E* curves in the dark stabilized in less than half the time required under illumination. This is consistent with the fact that under illumination, the  $J_{sc}$  required more time to reach a stable value than did  $V_{oc}$  ( $\approx 3$  h and  $\approx 1$  h, respectively).

### 3.3.3 Spectral Response

Figure 3.4a shows the spectral response data for cells that contained the same electrolyte compositions used to measure the  $J$ - $E$  behavior. Cells with 500 mM LiI–40 mM I<sub>2</sub>–50 mM AcH showed spectral response properties in accord with typical behavior for TiO<sub>2</sub>-Ru(H<sub>2</sub>L')<sub>2</sub>(NCS)<sub>2</sub> DSSC's,<sup>16,20,21</sup> with a quantum yield of 0.72 at the maximum of the MLCT absorption band (525–535 nm) and a low-energy shoulder extending to ≈ 800 nm. The response at  $\lambda < 380$  nm was in part due to direct absorption of photons by TiO<sub>2</sub>, and the decreased observed for  $\lambda < 350$  nm due to absorption by the FTO electrode.

The  $EQY$  decreased at all wavelengths when 500 mM LiI–40 mM I<sub>2</sub> was used in place of 500 mM LiI–40 mM I<sub>2</sub>–50 mM AcH, and decreased further when the electrolyte was 500 mM TBAI–40 mM I<sub>2</sub>. This behavior is consistent with the changes in  $J_{sc}$  observed for these electrolytes (Figure 3.3, Table 3.2). The changes in the action spectrum, like those observed in the  $J$ - $E$  properties, were reversed upon changing the electrolyte solution. Consistently, convolution of the  $EQY$  with the photon flux vs wavelength profile of the AM1.5 solar spectrum produced a calculated value of  $J_{sc}$  that was within experimental error to the measured value of  $J_{sc}$ .

The shapes of the spectral response were compared by normalizing the  $EQY$  data by its value at the wavelength of maximum absorption of the MLCT band (Figure 3.4b). In addition to the global drop in photocurrent across the entire spectrum, the shape of the spectral response curve changed, exhibiting a blue-shift of nearly 100 nm for 500 mM TBAI–40 mM I<sub>2</sub> electrolytes as compared to 500 mM LiI–40 mM I<sub>2</sub>–50 mM AcH.

Calculation of the internal quantum yield ( $IQY$ ) required correction of the  $EQY$  data by the amount of light absorbed by the dye:

$$IQY(\lambda) = \frac{EQY(\lambda)}{1 - 10^{-A_{dye}(\lambda)}}, \quad 3.3$$

where  $A_{dye}(\lambda)$  is the absorbance of the dye bound to TiO<sub>2</sub>. The absorption spectrum of a bare TiO<sub>2</sub> film was subtracted from a spectrum of the dye bound to a TiO<sub>2</sub> film to give

$A_{\text{dye}}(\lambda)$ . Re-absorption of scattered light was not accounted for, due to the low amount of scattering at the wavelengths of interest. Plots of  $IQY$  for DSSCs as a function of electrolyte are shown in Figure 3.5a. Normalized to the MLCT absorption maximum, the  $IQY$  was significantly reduced from 600–650 nm for 500 mM TBAI–40 mM  $I_2$  electrolytes (Figure 3.5b). Due to increasing relative error in  $A_{\text{dye}}$  at longer wavelengths, the large error in the  $IQY$  for  $\lambda > 650$  nm precluded accurate comparison.

### 3.4 DISCUSSION

#### 3.4.1 Dependence of the Interfacial Energetics on the Nature of the Electrolyte Cation

Standard capacitance-based methods to measure flat-band potentials, such as Mott-Schottky analysis,<sup>22</sup> generally yield ambiguous results on nanocrystalline  $TiO_2$  films because the particles are completely depleted and therefore have no space-charge region.<sup>4</sup> A shift in the energy of electron acceptor states in  $TiO_2$  nanoparticle films has been observed previously as a shift in the onset potential for charging of the nanocrystalline  $TiO_2$  electrode.<sup>19,23-25</sup> In this work, the relative shift of the energy of acceptor states was determined by a spectroelectrochemical method, in which the total charge injected into a  $TiO_2$  film during a potential step was simultaneously monitored by chronocoulometry and absorption spectroscopy. This spectroelectrochemical potential-step method has the advantage of being useful in electrolytes that also contain redox-active species.

For a  $TiO_2$  film of a given thickness, the amount of capacitive charging for a potential step of a given time duration is a function of the relative density of empty states at the applied potential of interest. Determination of the flat-band potentials from the chronocoulometric data requires a fit of the charging data to a theoretical model of the functional form of the density of states in the conduction band of the nanocrystalline  $TiO_2$ .<sup>19</sup> However, the relative shift in the position of the acceptor states is the quantity of

interest in this work. Thus the shifts of the capacitive charging vs applied potential curves relative to those observed for cells containing 500 mM LiI–40 mM I<sub>2</sub>–50 mM AcH (in which the *IQY* approaches unity) can be used to estimate the relative shift in the energy of acceptor states,  $E_{accept}$ . These spectrochronocoulometric results thus report on the relative number of states accessible to the MLCT state of the dye when the film is immersed in a non-aqueous electrolyte.

In aqueous solution, the value of  $E_{accept}$  for TiO<sub>2</sub> shifts by -60 mV per pH unit, due to protonation-deprotonation equilibria involving oxide/hydroxide species on the electrode surface.<sup>19,22,25-27</sup> A similar dependence of  $E_{accept}$  on the concentration of protons has been observed for TiO<sub>2</sub> electrodes in other protic solvents.<sup>24</sup> In anhydrous, aprotic solvents the conduction band-edge position is determined instead by other small cations, such as Li<sup>+</sup>, Na<sup>+</sup>, and Mg<sup>2+</sup>, which can intercalate into the TiO<sub>2</sub>.<sup>25,28,29</sup>

The effect of small cations on the  $E_{accept}$  position of nanocrystalline TiO<sub>2</sub> films is clearly evident by plotting the extent of charging versus the applied potential for each electrolyte (Figures 3.1 & 3.2). Shifts in the capacitive charging curves of > 1 V were observed as a function of [Li<sup>+</sup>] and [H<sup>+</sup>], with the curves shifting to more negative potentials at lower [Li<sup>+</sup>] and [H<sup>+</sup>] (Table 3.1). The band-edge position was more sensitive to the concentration of protons than to the concentration of Li<sup>+</sup>, as seen by the 150 mV shift effected by the addition of 50 mM AcH to 500 mM Li<sup>+</sup>, as compared the 40 mV shift going from 100 mM Li<sup>+</sup> to 500 mM Li<sup>+</sup>.

In the presence of the I<sup>-</sup>/I<sub>3</sub><sup>-</sup> redox couple in solution, the large majority of charge passed in the spectrochronocoulometric measurements was Faradaic. Although the total amount of charge passed was larger by an order of magnitude or more than in the absence of I<sup>-</sup>/I<sub>3</sub><sup>-</sup>, the amount of reversible charging was the same, at the same electrode potential vs a fixed reference electrode potential (Figure 3.2). The shifts in the capacitive charging curves in solutions of 500 mM TBAI–40 mM I<sub>2</sub>, 500 mM LiI–40 mM I<sub>2</sub>, and 500 mM LiI–40 mM I<sub>2</sub>–50 mM AcH as measured both electrochemically and spectroscopically

were observed to be the same as those measured in 500 mM TBAClO<sub>4</sub>, 500 mM LiClO<sub>4</sub> and 500 mM LiClO<sub>4</sub>–50 mM AcH solutions, respectively (Figures 3.1 & 3.2). This behavior indicates that the same shift in  $E_{accept}$  occurred in the presence of either ClO<sub>4</sub><sup>-</sup> or I<sup>-</sup>/I<sub>3</sub><sup>-</sup> (under identical conditions to the working solar cells used herein).

### 3.4.2 Dependence of the $J$ - $E$ Behavior on the Nature of the Electrolyte Cation

Under illumination, decreases in the concentration of either Li<sup>+</sup> or H<sup>+</sup> resulted in an increase in  $V_{oc}$ , with a concomitant decrease in  $J_{sc}$  (Figure 3.3, Table 3.2). In the dark, the cathodic current at -600 mV vs  $E(A/A^-)$  was reduced by nearly two orders of magnitude when the electrolyte was changed from 500 mM LiI–40 mM I<sub>2</sub>–50 mM AcH to 500 mM TBAI–40 mM I<sub>2</sub>. This type of behavior has been reported previously for systems in which the concentration or size of electrolyte cations was varied.<sup>8</sup> The observed reduction in dark current, and concomitant increase in  $V_{oc}$ , is consistent with a shift in  $E_{accept}$ , as evidenced by the spectrochronocoulometric data.

The presence of TBA<sup>+</sup> could in principle reduce the cathodic current by forming a passivating, physisorbed-blocking layer on the surface of the TiO<sub>2</sub>, thereby reducing the electron-transfer rate to the solution redox species. However, although cells with 500 mM TBAI–40 mM I<sub>2</sub> are highly rectifying, the addition of only 50 mM AcH (a factor of ten less than [TBA<sup>+</sup>]) resulted in a cell with  $J$ - $E$  properties nearly identical to those with 500 mM LiI–40 mM I<sub>2</sub>–50 mM AcH. Hence, the lowered  $J_{sc}$  and increased  $V_{oc}$  are not associated with the presence of TBA<sup>+</sup>, but rather with the absence of the potential-determining small cations. Furthermore, the effect on  $E_{accept}$  of H<sup>+</sup> is much larger than that of Li<sup>+</sup>, as demonstrated by  $J$ - $E$  curves of a cell with 500 mM LiI–40 mM I<sub>2</sub> being much more similar to cells with 500 mM TBAI–40 mM I<sub>2</sub> than to those with 500 mM LiI–40 mM I<sub>2</sub>–50 mM AcH (Figure 3.3).

When only the nature of the electrolyte cation is changed, a reduction in  $J_{sc}$  indicates that: 1) the quantum yield for electron injection has decreased; 2) the regeneration rate of the oxidized dye, D<sup>+</sup>, has decreased; 3) the rate of interfacial

electron-transfer from electrons in  $\text{TiO}_2$  to the  $\text{D}^+$  and/or oxidizing species in solution has become competitive with the rate of electron collection at the back electrode; or 4) surface desorption or decomposition of the sensitizer has become significant. Thus the increase in  $V_{oc}$  comes at the expense of rapid electron injection, rapid regeneration of the reduced form of the sensitizer, an enlarged rate of recombination of injected electrons in  $\text{TiO}_2$  with either the  $\text{D}^+$  or solution species, or dye desorption. The  $\approx 150$  mV shift observed for  $E_{accept}$  going from an electrolyte of 500 mM LiI–40 mM  $\text{I}_2$ –50 mM AcH to 500 mM LiI–40 mM  $\text{I}_2$  clearly produced a change in the rate of the effected reaction(s) large enough to reduce the electron collection yield five-fold! Hence, an upper limit on the magnitude of the beneficial shift in  $E_{accept}$  of  $\approx 100$  mV is present when only cations in the electrolyte are used to tune the interfacial energetics.

The drop in  $J_{sc}$  and increase in  $V_{oc}$  induced by reducing the concentration of small cations was fully reversed upon subsequent addition of small cations, indicating that the decreased  $J_{sc}$  in the absence of small cations is not simply due to dye desorption or decomposition. The lack of complete reversibility when 500 mM LiI–40 mM  $\text{I}_2$ –50 mM AcH was used first and then followed by flushing with 500 mM TBAI–40 mM  $\text{I}_2$  can be attributed to trace levels of  $\text{H}^+$  and  $\text{Li}^+$  still present in the electrolyte, even after flushing with 5–10 times the cell volume with 500 mM TBAI–40 mM  $\text{I}_2$ . This is consistent with the spectrochronocoulometry measurements, which indicated that even  $\text{Li}^+$  concentrations of less than 1 mM had a significant impact on the band-edge positions.

For cells without AcH, both the  $J$ - $E$  behavior in the dark and the photovoltage stopped changing faster than did the photocurrent, which gradually dropped for several hours before reaching a stable value. The time for the dark  $J$ - $E$  curves and the photovoltage to reach a constant value is presumably related to rate of surface protonation-deprotonation reactions and/or intercalation events as the  $\text{TiO}_2$  equilibrates with the electrolyte solution.<sup>27,28,30</sup> The loss of photocurrent however, was not well correlated in time to the changes in the dark  $J$ - $E$  curves, indicating a secondary effect.

### 3.4.3 Spectral Response Properties

Of the mechanisms that can account for loss in  $J_{sc}$  (decreased injection rate, decreased rate of dye regeneration, increased rate of back reaction to  $D^+$  and/or  $I_3^-$ , and dye decomposition), it is possible to rule out three. First, the return of high photocurrents upon replacement of the cell electrolyte is conclusive evidence that the loss of photocurrent is not due to dye desorption. Second, from the shifts in the  $J-E$  data in the dark, it is clear that the rate of electron transfer from  $TiO_2$  to solution species such as  $I_3^-$  is greatly reduced in the same electrolytes that result in low values of  $J_{sc}$ . This behavior is therefore inconsistent with the increased interfacial electron transfer to solution species. Third, the spectral response data are inconsistent with the efficiency of electron transfer from the excited state of the dye to  $TiO_2$  being sufficiently diminished to account for the drop in  $J_{sc}$ .

Injection is known to occur from both vibrationally hot and relaxed levels of the triplet state or singlet state.<sup>31-33</sup> Thus, if  $E_{accept}$  shifts more negative, and the energy levels of the ground and excited states of the dye do not shift by the same amount, electron injection would become thermodynamically less favorable. Hence the lower-energy triplet states of the dye would have reduced injection yields, producing a reduction in  $J_{sc}$ , in accord with the observed  $J-E$  data. However, since the  $^1MLCT$  state energy is  $\approx 750$  meV higher than that of the  $^3MLCT$  state,<sup>33</sup> electron injection would still be favorable from singlet levels as long as the shift in the conduction band edge were less than 750 meV. A cut-off in the spectral response at longer wavelengths, while maintaining high quantum yields at shorter wavelengths, would provide evidence of this reduced overlap of the dye excited states and the acceptor states in  $TiO_2$ . However, the measured  $EQY$  exhibited a nearly monotonic drop across all wavelengths (Figure 3.4a), including energies nearly 1 eV greater than the  $^3MLCT$  absorption maximum. Moreover, the monotonic drop was evident even when the shift in  $E_{accept}$  was only 200 meV, i.e., in the 500 mM LiI–40 mM  $I_2$  electrolyte. This behavior implies that the loss of photocurrent is *not* primarily due to

changes in the rate of electron transfer from the dye to the TiO<sub>2</sub> as a result of a decreased driving force of the reaction. The largely wavelength-independent drop in *EQY* indicates that the decrease in  $J_{sc}$  for cells without AcH in the electrolyte is thus not solely a result of a loss of driving force for injection.

The reduced  $J_{sc}$  could be due to an increased steady-state concentration of D<sup>+</sup> on the TiO<sub>2</sub> surface, which could result in increased recombination of injected electrons with D<sup>+</sup> and/or decreased absorption of sunlight. An increased concentration of D<sup>+</sup> could be due to a decrease in the regeneration rate of the dye due to a shift in the ground state reduction potential of the dye to higher energy.<sup>34-37</sup> Time-resolved measurements, described in the accompanying manuscript,<sup>37</sup> show that the loss of photocurrent in electrolytes with low concentrations of potential-determining cations can be largely attributed in fact to a loss of driving force for regeneration of the oxidized dye, explaining the lack of wavelength dependence observed in the spectral response.

Comparison of the normalized *EQY* *does* reveal a relative change in profile as the electrolyte cation was changed (Figure 3.4b). This shift points to a change in the energy distribution of the injecting states of the dye relative to the TiO<sub>2</sub> acceptor states. Cells with lower concentrations of H<sup>+</sup> or Li<sup>+</sup> showed a blue-shifted onset of their *EQY* by as much as 100 nm ( $\approx 0.3$  eV). Plotting the *IQY*, normalized to the MLCT maximum for comparison, thus shows the relative loss of injection yield at  $\lambda > 600$  nm for TBAI/I<sub>2</sub> samples (see Figure 3.5b). The decreasing ratio of *IQY* for low- vs high-energy photons as the concentrations of Li<sup>+</sup> and H<sup>+</sup> were decreased indicates that, although not the principal factor responsible for the reduced  $J_{sc}$  in the *J-E* curves, the conduction band edge of TiO<sub>2</sub> may indeed be shifted to higher energy relative to the excited state of the dye. Indeed, the comparison of normalized *IQY* curves indicate that electron injection from higher energy states of the dye ( $400 < \lambda < 500$ ) is relatively more efficient than the thermally relaxed state when comparing electrolytes without H<sup>+</sup> and/or Li<sup>+</sup> added.

While the origin of the lost photocurrent cannot be positively established using only steady-state methods, the reduced internal quantum yield across all wavelengths is strong evidence *against* a model in which solely the energy of conduction band states is shifted while the ground and excited states of the sensitizer remain constant. In the report following this one, time-resolved methods indicate that in fact the reduction potential of the dye is significantly shifted along with  $E_{accept}$  of  $\text{TiO}_2$ .<sup>37</sup>

### 3.5 CONCLUSIONS

The photocurrent and photovoltage of DSSCs are to a large extent determined by the concentration of potential-determining cations in the electrolyte. The nearly complete absence of small cations caused a  $\approx 1$  V shift in the conduction band energy, resulting in a 0.3 V increase in  $V_{oc}$ . The band-edge position shifted similarly regardless of whether it was measured in  $\text{ClO}_4^-$ -based electrolytes or those containing the  $\text{I}^-/\text{I}_3^-$  redox couple. However,  $J_{sc}$  was reduced five-fold in the absence of small cations. The decline in  $J_{sc}$  is not due to dye desorption from the  $\text{TiO}_2$  surface, as the current was fully regained by changing the electrolyte solution, nor is it due to a reduced overlap of the action spectrum with the solar spectrum. Instead, the decline is due to a loss of current across all wavelengths. The observed blue shift in the spectral response is nonetheless indicative of a decreased energy difference between the dye excited state and the conduction band. The spectral response data thus indicates that while electrolyte ions do affect the driving force for electron injection, the overall loss of photocurrent is not principally caused by this phenomenon.

### 3.6 ACKNOWLEDGMENTS

We acknowledge the Department of Energy, Office of Basic Energy Sciences, and the Beckman Institute of the California Institute of Technology for support of this work. We thank James McCusker for numerous valuable discussions.

**Table 3.1** Relative shifts in capacitive charge curves ( $E_{accept}$ ) as a function of electrolyte cations as determined by global fits of the spectroelectrochemical data. The calculated shift in  $E_{accept}$  is shown for each measurement method. The onset potential of the 500 mM Li<sup>+</sup> with 50 mM AcH was set to zero and others measured relative to it.

	<b>Coulometric (V)</b>	<b><math>\Delta A_{800\text{nm}}</math> (V)</b>	<b><math>\Delta A_{360\text{nm}}</math> (V)</b>
500 mM Li <sup>+</sup> , 50 mM AcH <sup>a</sup>	0	0	0
500 mM Li <sup>+</sup> <sup>b</sup>	-0.20 ± 0.03	-0.12 ± 0.06	-0.14 ± 0.06
100 mM Li <sup>+</sup> <sup>c</sup>	-0.25 ± 0.03	-0.18 ± 0.04	-0.14 ± 0.06
1 mM Li <sup>+</sup> <sup>d</sup>	-0.31 ± 0.03	-0.23 ± 0.06	-0.21 ± 0.08
500 mM TBA <sup>+</sup> <sup>e</sup>	-1.08 ± 0.17	-0.90 ± 0.24	n/a

a) 500 mM LiI, 40 mM I<sub>2</sub>, 50 mM AcH or 500 mM LiClO<sub>4</sub>, 50 mM AcH; b) 500 mM LiI, 40 mM I<sub>2</sub> or 500 mM LiClO<sub>4</sub>; c) 400 mM TBAClO<sub>4</sub>, 100 mM LiClO<sub>4</sub>; d) 500 mM TBAClO<sub>4</sub>, 1 mM LiClO<sub>4</sub>; e) 500 mM TBAI, 40 mM I<sub>2</sub> or 500 mM TBAClO<sub>4</sub>. All solutions CH<sub>3</sub>CN-based.

**Table 3.2** Summary of results of  $J$ - $E$  curves for various CH<sub>3</sub>CN-based electrolytes, under illumination and in the dark after equilibration (TiO<sub>2</sub> film exposed to electrolyte solution for 2 or more hours).

Electrolyte	$J_{sc}$ (mA/cm <sup>2</sup> )	$V_{oc}$ (V vs. $E(A/A^+)$ )	$ff$	Dark J at -600 mV vs. $E(A/A^+)$ , (mA cm <sup>-2</sup> )
500 mM LiI-40 mM I <sub>2</sub> - 50 mM AcH	17.3 ± 0.9	-0.56 ± 0.04	0.40 ± 0.02	-1.8 ± 0.5
500 mM LiI-40 mM I <sub>2</sub>	3.2 ± 0.1	-0.71 ± 0.01	0.62 ± 0.01	-0.18 ± 0.01
500 mM TBAI-40 mM I <sub>2</sub>	1.7 ± 1.2	-0.86 ± 0.03	0.72 ± 0.08	-0.05 ± 0.01

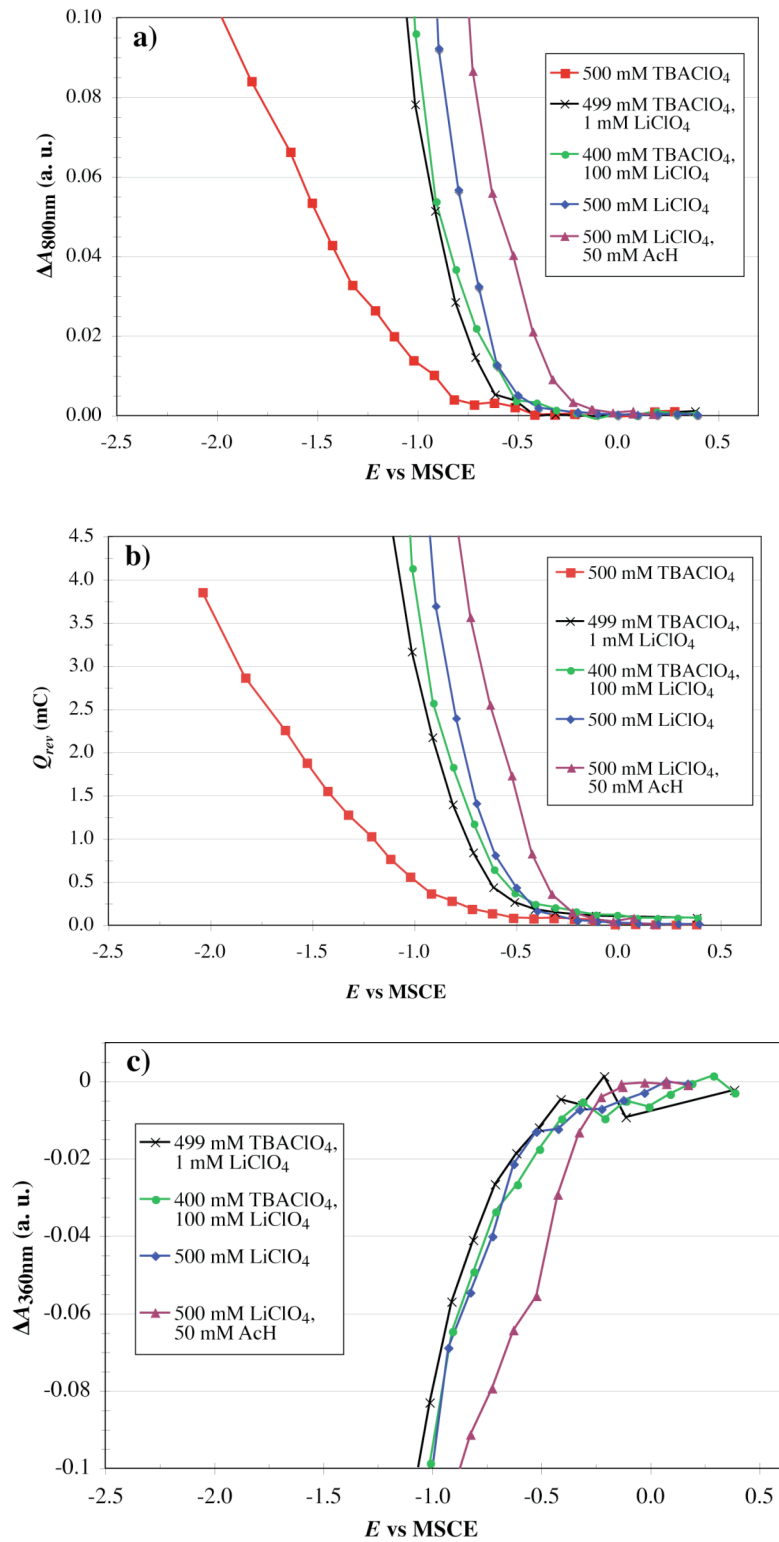


**Figure 3.1** The degree capacitive charging of TiO<sub>2</sub> films during a 30-sec potential step plotted vs the potential of the step, showing the effect of electrolyte cations on the relative energy distribution of acceptor states in TiO<sub>2</sub> in ClO<sub>4</sub><sup>-</sup>-based electrolytes in CH<sub>3</sub>CN. **a)** Charging curves as measured at 800 nm by time-dependent absorption spectroscopy. The broad absorption peak monitored here is due to the absorption of electrons in the TiO<sub>2</sub> film.<sup>19</sup> **b)** Plot of the charge reversibly injected electrochemically into a TiO<sub>2</sub> film as measured by chronocoulometry. Charge due to Faradaic current was subtracted from the total charge at each potential. **c)** A plot of the change in absorption at 360 nm. The drop in absorption near the band edge is due to the Burstein-Moss shift.<sup>19</sup>

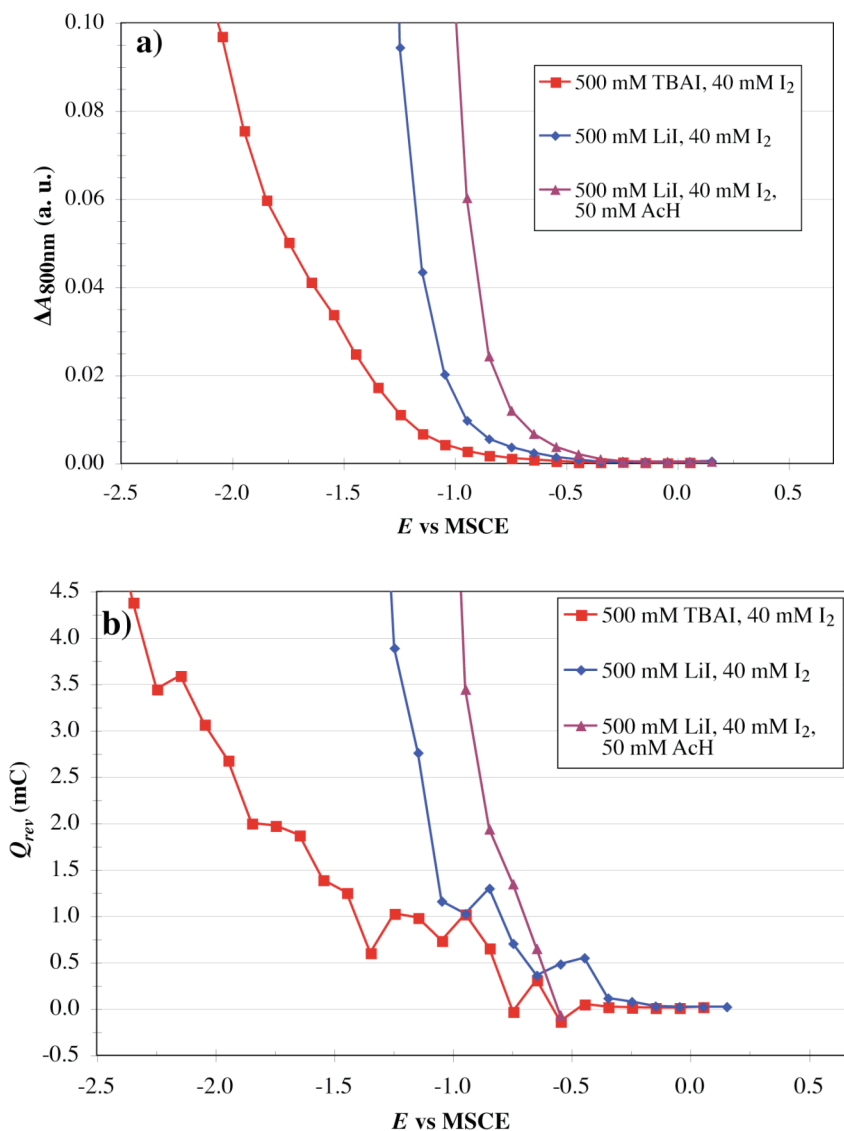


**Figure 3.2** The degree capacitive charging of  $\text{TiO}_2$  films during a 30-sec potential step plotted vs the potential of the step, showing the effect of electrolyte cations on the relative energy distribution of acceptor states in  $\text{TiO}_2$  a redox-active electrolyte of 500 mM  $\text{I}^-$  and 40 mM  $\text{I}_2$  in  $\text{CH}_3\text{CN}$ . **a)** Charging curves as measured at 800 nm by absorption spectroscopy. **b)** Plot of the charge reversibly injected electrochemically into a  $\text{TiO}_2$  film as measured by chronocoulometry. The Faradaic current due to reduction of  $\text{I}_3^-$  and  $\text{I}_2$  in solution was subtracted from the total at each potential.

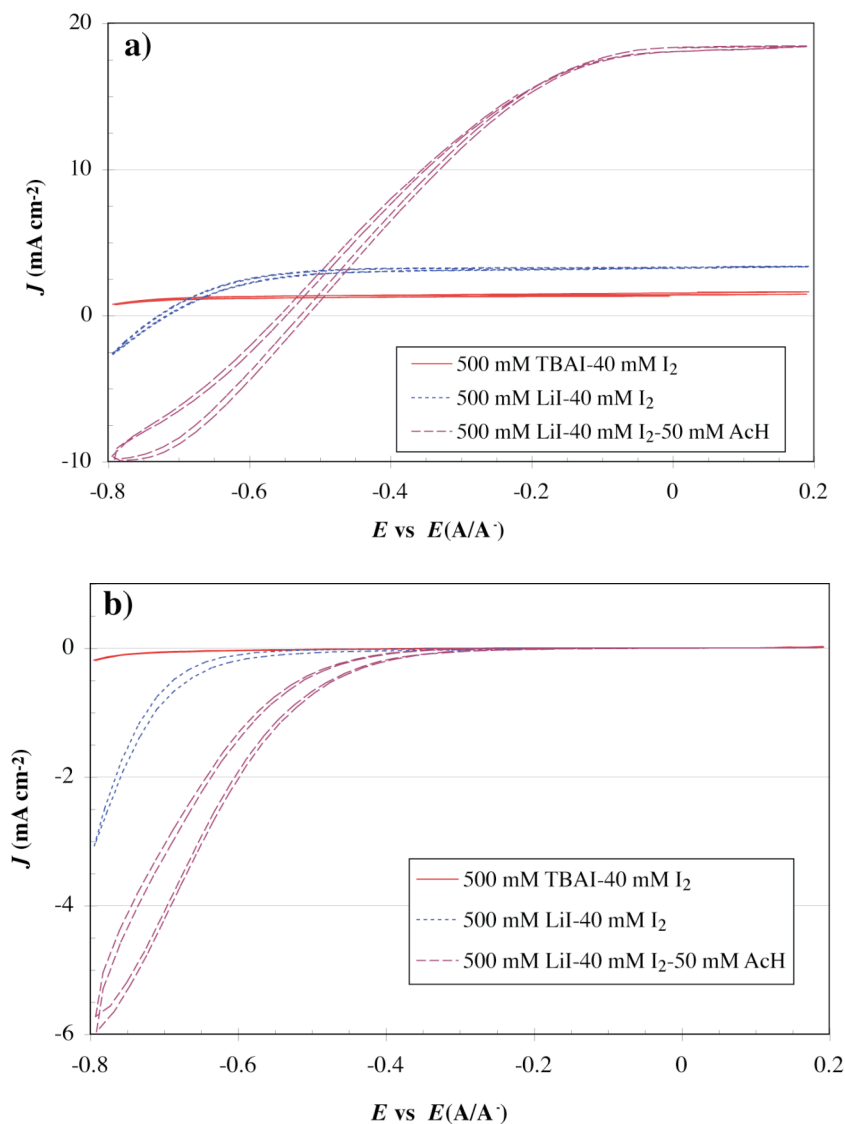


**Figure 3.3** Current density vs applied potential curves under illumination (a) and in the dark (b). The absence of potential-determining cations such as Li<sup>+</sup> or H<sup>+</sup> causes a drop in photocurrent and a simultaneous increase in photovoltage. The  $J$ - $E$  curves in the dark also reflect the increased photovoltage observed with low concentration of small cations.

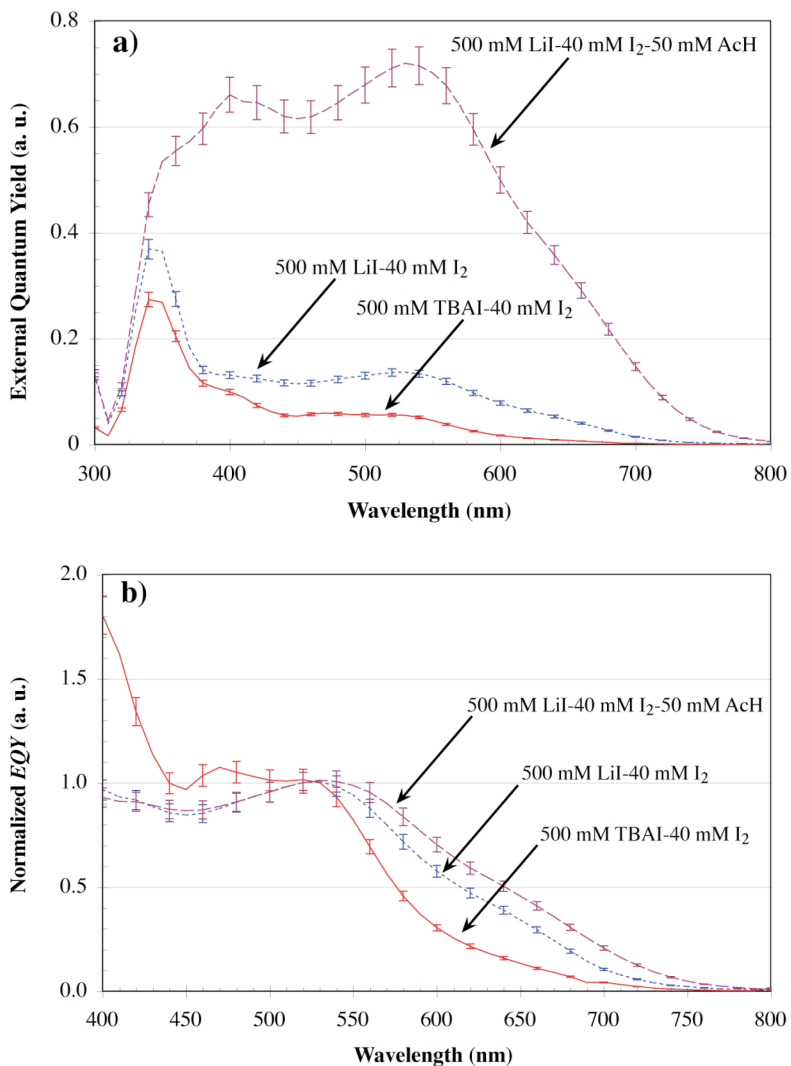


**Figure 3.4** Spectral response curves showing the effect of small cations in the electrolyte. **(a)** Plot of the external quantum yield vs wavelength of incident light. The apparent formation of a peak at 350 nm is due to the partial contribution to the photocurrent by direct band-gap absorption by  $\text{TiO}_2$ , which is unchanged, and the cut-off of the FTO glass, which does not transmit below 320 nm. **(b)** Spectral response curves, with the external quantum yield normalized to the maximum at the MLCT absorption band of  $\text{Ru}(\text{H}_2\text{L}')_2(\text{NCS})_2$ , showing the effect blue-shifted onset for cells with no  $\text{H}^+$  or  $\text{Li}^+$  in the electrolyte.

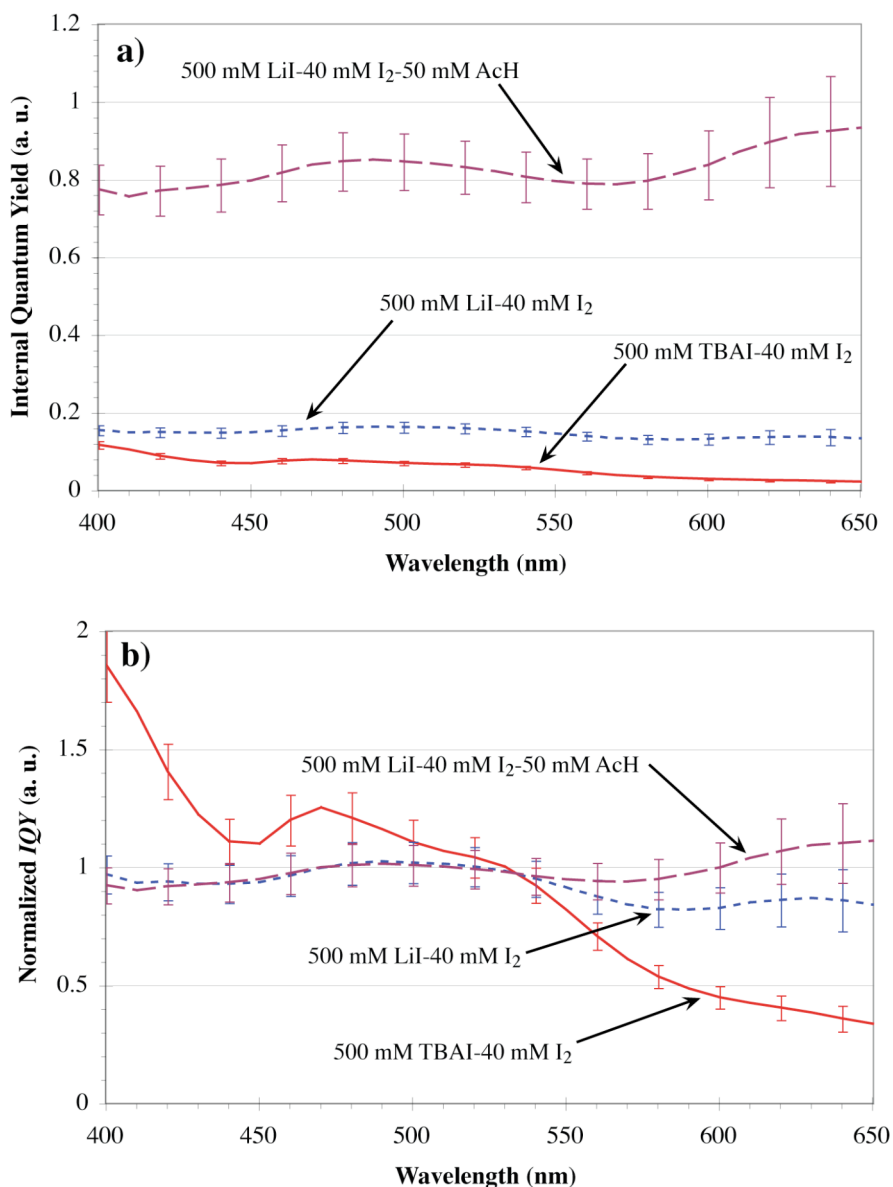


**Figure 3.5** (a) Internal quantum yield curves showing the significant decrease at all wavelengths for electrolytes lacking small cations. (b) Internal quantum yield, normalized to the maximum at the MLCT band of Ru(H<sub>2</sub>L')<sub>2</sub>(NCS)<sub>2</sub>, showing the increased collection ratio of high- to low-energy photons for cells containing no H<sup>+</sup> or Li<sup>+</sup>.

## REFERENCES

- (1) Oregan, B.; Gratzel, M. *Nature* **1991**, 353, 737.
- (2) Gratzel, M. *Nature* **2001**, 414, 338.
- (3) Hagfeldt, A.; Gratzel, M. *Accounts Chem. Res.* **2000**, 33, 269.
- (4) Cahen, D.; Hodes, G.; Gratzel, M.; Guillemoles, J. F.; Riess, I. *J. Phys. Chem. B* **2000**, 104, 2053.
- (5) Pichot, F.; Gregg, B. A. *J. Phys. Chem. B* **2000**, 104, 6.
- (6) Kallioinen, J.; Benko, G.; Myllyperkio, P.; Khriachtchev, L.; Skarman, B.; Wallenberg, R.; Tuomikoski, M.; Korppi-Tommola, J.; Sundstrom, V.; Yartsev, A. P. *J. Phys. Chem. B* **2004**, 108, 6365.
- (7) Lemon, B. I.; Liu, F.; Hupp, J. T. *Coord. Chem. Rev.* **2004**, 248, 1225.
- (8) Watson, D. F.; Meyer, G. J. *Coord. Chem. Rev.* **2004**, 248, 1391.
- (9) Durrant, J. R.; Haque, S. A.; Palomares, E. *Coord. Chem. Rev.* **2004**, 248, 1247.
- (10) Anderson, N. A.; Lian, T. *Coord. Chem. Rev.* **2004**, 248, 1231.
- (11) Tan, M. X.; Laibinis, P. E.; Nguyen, S. T.; Kesselman, J. M.; Stanton, C. E.; Lewis, N. S. Principles and Applications of Semiconductor Photoelectrochemistry. In *Progress in Inorganic Chemistry, Vol 41* **1994**, 21.
- (12) Serpone, N.; Pelizzetti, E., Eds. *Photocatalysis: Fundamentals and Applications* **1989**, Wiley: New York, 650.
- (13) Burnside, S.; Moser, J. E.; Brooks, K.; Gratzel, M.; Cahen, D. *J. Phys. Chem. B* **1999**, 103, 9328.

- (14) Kelly, C. A.; Farzad, F.; Thompson, D. W.; Stipkala, J. M.; Meyer, G. J. *Langmuir* **1999**, *15*, 7047.
- (15) Park, N. G.; Chang, S. H.; van de Lagemaat, J.; Kim, K. J.; Frank, A. J. *Bull. Korean Chem. Soc.* **2000**, *21*, 985.
- (16) Nazeeruddin, M. K.; Kay, A.; Rodicio, I.; Humphrybaker, R.; Muller, E.; Liska, P.; Vlachopoulos, N.; Gratzel, M. *J. Am. Chem. Soc.* **1993**, *115*, 6382.
- (17) Nazeeruddin, M. K.; Humphry-Baker, R.; Liska, P.; Gratzel, M. *J. Phys. Chem. B* **2003**, *107*, 8981.
- (18) Pelet, S.; Moser, J. E.; Gratzel, M. *J. Phys. Chem. B* **2000**, *104*, 1791.
- (19) Rothenberger, G.; Fitzmaurice, D.; Gratzel, M. *J. Phys. Chem.* **1992**, *96*, 5983.
- (20) Sauve, G.; Cass, M. E.; Coia, G.; Doig, S. J.; Lauermann, I.; Pomykal, K. E.; Lewis, N. S. *J. Phys. Chem. B* **2000**, *104*, 6821.
- (21) Sauve, G.; Cass, M. E.; Doig, S. J.; Lauermann, I.; Pomykal, K.; Lewis, N. S. *J. Phys. Chem. B* **2000**, *104*, 3488.
- (22) Bolts, J. M.; Wrighton, M. S. *J. Phys. Chem.* **1976**, *80*, 2641.
- (23) Enright, B.; Redmond, G.; Fitzmaurice, D. *J. Phys. Chem.* **1994**, *98*, 6195.
- (24) Redmond, G.; Fitzmaurice, D. *J. Phys. Chem.* **1993**, *97*, 1426.
- (25) Boschloo, G.; Fitzmaurice, D. *J. Phys. Chem. B* **1999**, *103*, 7860.
- (26) Dang, X. J.; Massari, A. M.; Hupp, J. T. *Electrochem. Solid State Lett.* **2000**, *3*, 555.
- (27) Lyon, L. A.; Hupp, J. T. *J. Phys. Chem. B* **1999**, *103*, 4623.
- (28) Lyon, L. A.; Hupp, J. T. *J. Phys. Chem.* **1995**, *99*, 15718.

- (29) Sodergren, S.; Siegbahn, H.; Rensmo, H.; Lindstrom, H.; Hagfeldt, A.; Lindquist, S. E. *J. Phys. Chem. B* **1997**, *101*, 3087.
- (30) Lemon, B. I.; Hupp, J. T. *J. Phys. Chem.* **1996**, *100*, 14578.
- (31) Lenzmann, F.; Krueger, J.; Burnside, S.; Brooks, K.; Gratzel, M.; Gal, D.; Ruhle, S.; Cahen, D. *J. Phys. Chem. B* **2001**, *105*, 6347.
- (32) Benko, G.; Kallioinen, J.; Korppi-Tommola, J. E. I.; Yartsev, A. P.; Sundstrom, V. *J. Am. Chem. Soc.* **2002**, *124*, 489.
- (33) Asbury, J. B.; Anderson, N. A.; Hao, E. C.; Ai, X.; Lian, T. Q. *J. Phys. Chem. B* **2003**, *107*, 7376.
- (34) Zaban, A.; Ferrere, S.; Gregg, B. A. *J. Phys. Chem. B* **1998**, *102*, 452.
- (35) Zaban, A.; Ferrere, S.; Sprague, J.; Gregg, B. A. *J. Phys. Chem. B* **1997**, *101*, 55.
- (36) Yan, S. G.; Hupp, J. T. *J. Phys. Chem.* **1996**, *100*, 6867.
- (37) Katz, J. E.; Smeigh, A. L.; McCusker, J. K.; Brunshwig, B. S.; Lewis, N. S. (*submitted for publication*), 2007.

## CHAPTER 4

### *Time-Resolved Characterization of the Dependence of Interfacial Electron-Transfer Rates on Electrolyte Ions in Dye-Sensitized Solar Cells*

#### 4.1 INTRODUCTION

The inexpensive earth-abundant materials used in dye-sensitized solar cells (DSSCs), and the high-energy conversion efficiencies of the devices have prompted a great deal of interest since the initial report by O'Regan and Gratzel in 1991.<sup>1-14</sup> However due to the complexity of the DSSC system, in the intervening years the efficiency of DSSCs has only improved marginally. It is now recognized that the cell's complex kinetics and thermodynamics leads to a conflicting set of requirements to optimize both the photocurrent and photovoltage of the cell. Thus only a thorough understanding of the kinetics and thermodynamics of a working solar cell will allow for further improvements in conversion efficiencies.

In a typical DSSC, a sensitizer dye is bound to a nanoporous film of TiO<sub>2</sub> particles mounted on a transparent conductive substrate. The film is immersed in a redox-containing electrolyte solution. Upon absorption of light, the dye forms an excited state which injects an electron into the TiO<sub>2</sub> film. The electron is collected at the

back contact, passes through an external circuit, and then reduces the redox species in solution at the counter electrode. The reduced redox species subsequently donates an electron to the oxidized sensitizer to complete the circuit.

The principal electron-transfer reactions in a DSSC are shown in Figure 4.1. This report focuses on the effects of electrolyte on the rates of interfacial electron transfer at the TiO<sub>2</sub> electrode: injection into TiO<sub>2</sub>,  $k_2$ ; regeneration of the oxidized dye by the redox mediator,  $k_3$ ; and recombination or back reaction between injected electrons in TiO<sub>2</sub> and the oxidized dye,  $k_4$ .

For a solar cell to have a high overall conversion efficiency, large photocurrents and photovoltages are required simultaneously. Generation of high photocurrents requires that: The sensitizer must strongly absorb photons at energies where the solar flux is greatest. Electron injection must be fast compared to deactivation of the excited state ( $k_2 \gg k_{-1}$ ). Dye regeneration must be faster than recombination ( $k_3[I] \gg k_4[e^-]$ ), where  $[e^-]$  is the surface concentration of electrons in TiO<sub>2</sub>. And finally electron transport through the TiO<sub>2</sub> film and collection at the back contact must effectively compete with reduction of any solution redox species ( $k_5$ ). The maximum photovoltage,  $V_{oc}^{max}$ , is given by the difference between the Nernstian potential of the solution,  $E(A/A^-)$  and the potential of the bottom of the conduction band of the semiconductor. Thus to maximize the photovoltage, the driving forces for the electron injection,  $E_{inj}$ , and regeneration of the dye,  $E_{regen}$ , need to be minimized. However, minimization of these will ultimately lead to decreases in  $k_2$  and  $k_3$  and loss of photocurrent. The goal of the present study is to elucidate the interplay between the multiple and partially contradictory requirements for efficient DSSCs.

Cations, such as  $\text{H}^+$  and  $\text{Li}^+$ , in the electrolyte solution have a significant impact on both the steady-state and kinetic properties of DSSCs.<sup>7,15-17</sup> In Chapter 3, we showed that the use of  $\text{TBA}^+$  in place of  $\text{Li}^+$  and acetic acid ( $\text{AcH}$ ) as the electrolyte in a  $\text{TiO}_2$ -based cell using  $\text{Ru}(\text{H}_2\text{L}')_2(\text{NCS})_2$ , decreases the short-circuit current ( $J_{sc}$ ) by a factor of  $\sim 5$ , while increasing the open-circuit voltage ( $V_{oc}$ ), by  $\sim 0.3$  V.<sup>16</sup> The absence of small cations produced a  $\sim -1$  V shift in the energy of electron acceptor states in  $\text{TiO}_2$ ,  $E_{accept}$ , compared to solutions with  $\text{Li}^+$  and  $\text{AcH}$ . Thus the increased  $V_{oc}$  was due to this shift in  $E_{accept}$  as a function of the concentration of small cations. The concomitant decreased photocurrent was shown not to be due to loss of dye absorption,  $k_1$ , nor were increases in dark current observed, which suggests that  $k_5$  did not increase. Further, spectral response measurements showed that the decrease in  $J_{sc}$  was largely independent of wavelength, suggesting that the loss of photocurrent was not predominately caused by reduced electron injection from the lowest energy levels of the excited state.

The impact of both the cations and the anions in the electrolyte solution on the electron transfer reactions occurring at the  $\text{TiO}_2$ -dye-electrolyte interface will be discussed, along with the implications this has on the photocurrent and photovoltage of DSSCs. The transient absorption (TA) data presented here compare the two electrolytes resulting in the largest difference in the conduction band-edge energy as two limiting cases: electrolytes using the sterically bulky cation tetra-butylammonium ( $\text{TBA}^+$ ) and having a concentration of small cations approaching zero, with that of an electrolyte containing the potential-determining cations  $\text{Li}^+$  and  $\text{H}^+$ .

## 4.2 EXPERIMENTAL

### 4.2.1 Materials

Reagent purification and preparation was as described in Chapter 3. Acetonitrile, acetic acid (AcH), silver nitrate, lithium iodide, and  $\text{Ru}(\text{H}_2\text{L}')_2(\text{NCS})_2$  (Ruthenium 535, Solaronix) were used as received. Lithium perchlorate was dried by fusing at 240 °C under vacuum. Tetrabutylammonium perchlorate ( $\text{TBAClO}_4$ ) was recrystallized three times from hot ethanol with diethylether and dried under vacuum at 130 °C. Tetrabutylammonium iodide (TBAI) was recrystallized from acetone with ether three times and dried under vacuum at room temperature. Iodine was resublimed at 40 °C. All materials were stored in the dark, and under  $\text{N}_2(\text{g})$ , with the exception of  $\text{I}_2$ , acetic acid, and  $\text{Ru}(\text{H}_2\text{L}')_2(\text{NCS})_2$ . All electrolytes were prepared under  $\text{N}_2(\text{g})$ . Ferrocene (Fc) (Aldrich, 98%) and 1,1'-dimethylferrocene ( $\text{Me}_2\text{Fc}$ ) (Aldrich, 97%) were sublimed under dynamic vacuum at 35 °C. 1,1'-dibromoferrocene (Alfa Aesar, 96%) was used as received.

Nanoparticles of  $\text{ZrO}_2$  were synthesized using the sol-gel method.<sup>18</sup> Zr-n-propoxide (70% in propanol, Aldrich), 6 mL, was added to 0.775 mL acetic acid (99.99%, Aldrich) under  $\text{N}_2(\text{g})$ .  $\text{H}_2\text{O}$  (25 mL, > 18  $\text{M}\Omega$  cm) was added quickly while stirring vigorously (in air). The initially formed jelly-like solution formed a white precipitate after stirring for ~ 1 h. After adding 1 mL  $\text{HNO}_3$  (70% solution, 99.999+%, Aldrich), the solution became clear. After stirring overnight and then adding  $\text{H}_2\text{O}$  for a total volume of 35 mL, the solution was heated to 215 °C in an acid digestion bomb (Parr) for 12 hours. The liquid was subsequently decanted, and the concentration was adjusted by roto-evaporation to 22.5% wt  $\text{ZrO}_2$ . Finally, 0.8 g polyethylene glycol (Carbowax 20,000, Fluka) was added and stirred overnight.  $\text{ZrO}_2$  particle size was 10–20

nm, comparable to that of TiO<sub>2</sub>, as determined by transmission electron microscopy images.

#### 4.2.2 Fabrication of Photoelectrochemical Cells

Photoanodes of TiO<sub>2</sub> nanoparticles on conductive fluorine-doped tin oxide (FTO) glass were prepared as described in Chapter 3. TiO<sub>2</sub> films, 5.0 μm thick, were treated with 0.2 M TiCl<sub>4</sub>(aq) overnight, rinsed with water, sintered at 450 °C for 30 minutes, cooled to 120 °C, and immediately immersed in a solution of  $\sim 1 \times 10^{-4}$  M Ru(H<sub>2</sub>L')<sub>2</sub>(NCS)<sub>2</sub> in ethanol.

ZrO<sub>2</sub> films were printed using the doctor blade technique, baked at 450 °C for 1 hour, and then measured to be  $\sim 10$  μm thick by profilometry (Dektak, 3030). Prior to use, ZrO<sub>2</sub> films were sintered and sensitized with Ru(H<sub>2</sub>L')<sub>2</sub>(NCS)<sub>2</sub> as for TiO<sub>2</sub> films.

Three electrochemical cell designs were used. A 3-electrode cell was used for combined spectroscopic and electrochemical measurements as described in Chapter 3. A “sandwich” cell was used for spectroscopic characterization. The cell was made by sealing a glass microscope slide to a TiO<sub>2</sub> or ZrO<sub>2</sub> electrode using a spacer of silicone rubber (0.8 mm thick). Electrolyte was introduced into the cell via a syringe needle placed between the silicone spacer and the glass cover slip. Alternately, sandwich cells were assembled using 60-μm-thick SX1170 film (Solaronix) as a spacer. The cell was sealed by heating on a hot plate at  $\sim 100$  °C and applying pressure for several seconds. Electrolyte was injected through one of two small holes drilled in the microscope slide, which were then sealed with SX1170 and a glass cover slip using a soldering iron. The cell was kept in the dark until use. All cells were prepared within 24 hours of performing measurements.

Electrolyte solutions were prepared and electrochemical cells assembled in a glove box under N<sub>2</sub> or Ar atmosphere. Acetonitrile-based electrolytes consisted of 50 mM AcH and 500 mM Li<sup>+</sup> with either ClO<sub>4</sub><sup>-</sup> or I<sup>-</sup>, or alternatively 500 mM TBA<sup>+</sup> with either ClO<sub>4</sub><sup>-</sup> or I<sup>-</sup>. In certain cases I<sub>2</sub> was added to I<sup>-</sup>-containing electrolytes. In all cases, the ionic strength of the electrolyte was kept constant at 500 mM.

Electronic absorption spectra were collected using a Hewlett-Packard Model 8425A diode array spectrophotometer (at MSU) or an Agilent 8453 (at Caltech).

### 4.2.3 Femtosecond Transient Absorption Spectroscopy

The femtosecond TA spectrometer used for these studies is described in detail elsewhere.<sup>19</sup> A sapphire-generated continuum (450–950 nm) was used as the probe source for all measurements. Single wavelength kinetics traces were obtained using 10 nm band-pass filters positioned after the sample. Dye excitation was carried out using 100 fs pulses of 530 nm light close to the maximum of the lowest energy <sup>1</sup>A<sub>1</sub> → <sup>1</sup>MLCT absorption of Ru(H<sub>2</sub>L')<sub>2</sub>(NCS)<sub>2</sub> when bound to TiO<sub>2</sub> or ZrO<sub>2</sub>. Significant problems with photobleaching of the films were encountered when excitation power densities were above 5 μJ. Consequently, the pump beam was typically attenuated with neutral density filters to yield pump powers on the order of ~ 2 μJ at the sample with a beam diameter of ~ 1 mm. Films were excited through the FTO back contact and translated after each full scan of the optical delay line to ensure the integrity of the sample. Data sets were typically the average of 10 scans. Absorption spectra collected before and after all time-resolved measurements differed by less than 5%. Optical densities of the Ru(H<sub>2</sub>L')<sub>2</sub>(NCS)<sub>2</sub>-sensitized films at 530 nm were in the range of 0.7–0.9 for TiO<sub>2</sub> and 0.3–0.5 for ZrO<sub>2</sub>; the lower ODs for the ZrO<sub>2</sub> films were a consequence of the lower

loading of Ru(H<sub>2</sub>L')<sub>2</sub>(NCS)<sub>2</sub> on these films. Estimation of  $\Delta t = 0$  at each probe wavelength was achieved utilizing pump scatter from a neat film (i.e., films with no adsorbed dye but otherwise identical) and/or stimulated Raman scattering from the solvent. All measurements were carried out at room temperature.

#### 4.2.4 Nanosecond Transient Absorption and Emission Spectroscopy

Nanosecond TA spectroscopy was performed using an instrument described previously.<sup>20</sup> A 520 nm excitation pulse with a repetition rate of 10 Hz and  $\sim 8$  ns width, was generated by an OPO pumped by a Nd:YAG laser. Probe light, from a 75 W Xe arc lamp, operated in pulsed mode, was passed through the sample and into a double monochromator (JY H10) and was monitored with a photomultiplier tube (Hamamatsu R928). The signal was amplified by a current-sensitive amplifier (Phillips Scientific 6931) and recorded with a oscilloscope (LeCroy 9354A). A 515-nm-long pass filter was placed between the probe source and sample. The sample was excited through the FTO back contact, and was only illuminated during data collection. For measurements at 560 nm, a 540-nm-long pass filter at the monochromator aperture rejected scattered laser light. UV-Vis absorption spectra of the cell were measured before and after TA experiments to check for sample degradation.

Time-resolved emission measurements of the dye adsorbed to ZrO<sub>2</sub> and TiO<sub>2</sub> films were as above, except with no probe light used. Samples were excited at either 355 nm or 520 nm. The system response was measured using scattered laser light from an unsensitized TiO<sub>2</sub> film. Using a routine written in Matlab, data was fit by iterative convolution of the system response function using a sum of exponentials (with  $n = 1, 2$ ):

$$\Delta A = a_0 + \sum_{i=1}^n a_i \exp(-\kappa_i t), \quad 4.1$$

The decays were characterized by weighted-average time constant,  $\tau_{avg}$ :

$$\tau_{avg} = \frac{\sum (a_i / \kappa_i)}{\sum a_i}. \quad 4.2$$

## 4.3 RESULTS

### 4.3.1 Femtosecond-Resolved Dynamics

#### 4.3.1.1 Injection Dynamics in $ClO_4^-$ -Based Electrolytes

The rate of electron injection into  $Ru(H_2L')_2(NCS)_2$ -sensitized films of  $TiO_2$  and  $ZrO_2$  was studied using  $\sim 100$  fs excitation pulse of 530 nm light. Electron injection kinetics of  $Ru(H_2L')_2(NCS)_2$ -sensitized films in contact with 500 mM  $LiClO_4$ –50 mM AcH or 500 mM  $TBAClO_4$  are plotted in Figure 4.2 and summarized in Table 4.1.

Figure 4.3 shows the dynamics on the non-injecting substrate  $ZrO_2$  were used as control studies for measurements on  $TiO_2$ . For the  $ZrO_2$  films, at either 700 or 800 nm, after the initial instrument-limited rise at  $t < 1$  ps, there was no significant change in the absorption characteristics of  $Ru(H_2L')_2(NCS)_2$  over a 250 ps window in both electrolytes. In contrast, Figure 4.2 shows significant changes in absorbance as a function of time for  $Ru(H_2L')_2(NCS)_2$  bound to  $TiO_2$  at  $t > 1$  ps. At  $\lambda_{probe} = 700$  nm (Figure 4.2a), an initial absorbance increase ( $t < 1$  ps) was followed by a decay to a steady-state value which persisted for 250 ps. At  $\lambda_{probe} = 800$  nm (Figure 4.2b), following an initial instrument-limited rise, an increase in absorbance was observed over the time window corresponding to the decay at 700 nm, leading to a plateau which stayed roughly constant to 250 ps. In the case of the 500 mM  $TBAClO_4$  electrolyte, the data at both wavelengths was fit to a single exponential with time constants of  $\tau_{700nm} = 9.0 \pm 1.2$  ps and  $\tau_{800nm} = 10 \pm 2$  ps; the

corresponding values for 500 mM LiClO<sub>4</sub>–50 mM AcH electrolyte were  $\tau_{700\text{nm}} = 9.2 \pm 1.3$  ps and  $\tau_{800\text{nm}} = 7 \pm 2$  ps (Table 4.1).

#### 4.3.1.2 Injection Dynamics in Electrolytes Containing I<sup>-</sup> or I<sub>3</sub><sup>-</sup>

Figure 4.4 shows the dynamics for Ru(H<sub>2</sub>L')<sub>2</sub>(NCS)<sub>2</sub>-sensitized TiO<sub>2</sub> films under conditions identical to those for which steady-state photocurrent measurements were made (see Chapter 3) and are summarized in Table 4.1. The electrolyte was either 500 mM LiI–40 mM I<sub>2</sub>–50 mM AcH or 500 mM TBAI–40 mM I<sub>2</sub> in CH<sub>3</sub>CN. As before, analogous data for Ru(H<sub>2</sub>L')<sub>2</sub>(NCS)<sub>2</sub> bound to ZrO<sub>2</sub> were acquired (Figure 4.5). The transient absorption data on ZrO<sub>2</sub> revealed no change in absorption at  $t > 1$  ps out to 250 ps. Figure 4.4a shows data obtained at  $\lambda_{\text{probe}} = 700$  nm for TiO<sub>2</sub> films, where a decay following excitation at 530 nm with a time constant of  $28 \pm 8$  ps was observed in 500 mM LiI–40 mM I<sub>2</sub>–50 mM AcH solutions. In the same solution at  $\lambda_{\text{probe}} = 800$  nm (bottom panel), an increase in the transient absorbance was observed with a time constant of  $15 \pm 5$  ps. This is within the error of the  $\sim 10$  ps dynamics obtained in the 500 mM LiClO<sub>4</sub>–50 mM AcH electrolyte

Significantly different results were obtained for solutions of 500 mM TBAI–40 mM I<sub>2</sub> at both probe wavelengths. Here, only small or no absorbance changes were observed (after the initial absorbance increase at  $t < 1$  ps) out to 250 ps. This was most clearly evident at  $\lambda_{\text{probe}} = 700$  nm (Figure 4.4a): whereas a clear decay was observed for 500 mM TBAClO<sub>4</sub>, 500 mM LiClO<sub>4</sub>–50 mM AcH (Figure 4.2) and 500 mM LiI–40 mM I<sub>2</sub>–50 mM AcH solutions (Figure 4.4), there was little evidence of spectral changes in the presence of 500 mM TBAI–40 mM I<sub>2</sub> on a corresponding time scale. At  $\lambda_{\text{probe}} = 800$  nm, after the initial rise, there was an increase in amplitude evident which could be fit with a

time constant of  $13 \pm 5$  ps. However, the magnitude of change in the signal was about 60% smaller than for the  $\text{Li}^+$ - or  $\text{ClO}_4^-$ -based solutions.

Additional measurements with no  $\text{I}_2$  added were carried out to determine whether this change in behavior was associated with the presence of  $\text{I}^-$  or  $\text{I}^-/\text{I}_3^-$ . These data are presented in Figure 4.6 for solutions of 500 mM LiI–50 mM AcH and 500 mM TBAI. The observations were qualitatively similar with or without added  $\text{I}_2$ , with some subtle differences. The time-resolved absorption data for 500 mM TBAI–40 mM  $\text{I}_2$  solutions showed a weak rising feature at  $\lambda_{\text{probe}} = 800$  nm (Figure 4.4b) that was more pronounced in the absence of  $\text{I}_3^-$ . This feature was smaller than that observed for 500 mM LiI–50 mM AcH and also for 500 mM LiI–40 mM  $\text{I}_2$ –50 mM AcH solutions. In addition, at  $\lambda_{\text{probe}} = 700$  nm, the data for 500 mM TBAI solutions appear to show a very slight decrease in amplitude over the first  $\sim 25$  ps. It should be stressed, however, that these amplitude changes are significantly attenuated relative to what was seen for 500 mM TBAClO<sub>4</sub> or any of the  $\text{Li}^+$ -based solutions. Again, bound to  $\text{ZrO}_2$ , the dye showed no dynamics on this timescale at either probe wavelength (Figure 4.7).

### 4.3.2 Nanosecond-Resolved Dynamics

#### 4.3.2.1 *Recombination with the Oxidized Dye*

Figure 4.8 shows the transient absorption signals at  $\lambda_{\text{probe}} = 560$  nm, attributable to recombination of injected electrons with  $[\text{Ru}(\text{H}_2\text{L}')_2(\text{NCS})_2]^+$  bound to  $\text{TiO}_2$ . No significant difference between 500 mM  $\text{LiClO}_4$ –50 mM AcH and 500 mM TBAClO<sub>4</sub> electrolytes is observed at 560 nm in the decays. Fitting the ground state recovery to an exponential fit, the weighted-average time constant was  $1.0 \pm 0.1$   $\mu\text{s}$  for both electrolytes (see Table 4.2).

#### 4.3.2.2 *Regeneration by I<sup>-</sup>*

Table 4.2 shows the kinetics of regeneration of the oxidized dye as a function of the concentration of I<sup>-</sup> in the contacting solution in both 500 mM LiI–50 mM AcH and TBAI electrolytes. Monitoring the negative absorption feature at 560 nm, a clear difference is observed in the kinetics for 500 mM LiI–50 mM AcH vs 500 mM TBAI solutions. As seen in Figure 4.9, a longer decay is observed for 500 mM TBAI than 500 mM LiI–50 mM AcH. For 500 mM LiI–50 mM AcH electrolytes, the weighted-average time constant of the bi-exponential fit was  $17 \pm 5$  ns (instrument limited), while for the 500 mM TBAI solution the measured time constant was  $350 \pm 20$  ns. Similarly, in 100 mM LiI–50 mM AcH (and 400 mM LiClO<sub>4</sub>), the time constant was  $300 \pm 30$  ns, compared to  $1.1 \pm 0.1$   $\mu$ s in 100 mM TBAI (and 400 mM TBAClO<sub>4</sub>). This value in 100 mM TBAI is a lower limit for regeneration of the dye, as recombination was competitive with regeneration on these time scales. Regeneration rates in solutions of 500 mM TBAI with 50 mM AcH added were nearly identical to those of 500 mM LiI–50 mM AcH (data not shown).

#### 4.3.2.3 *Regeneration by I<sup>-</sup> with I<sub>3</sub><sup>-</sup> Present*

Using 500 mM I<sup>-</sup> with 40 mM I<sub>2</sub>, as in a working device, Figure 4.10 shows that the regeneration rates were largely unchanged compared to measurements made solely in the presence of I<sup>-</sup>. For the 500 mM LiI–40 mM I<sub>2</sub>–50 mM AcH electrolyte, the decay of the negative absorption change at 560 nm was fit to a time constant of  $20 \pm 5$  ns, compared to  $280 \pm 20$  ns for 500 mM TBAI–40 mM I<sub>2</sub> (Table 4.2). When the concentration of the I<sup>-</sup>/I<sub>3</sub><sup>-</sup> redox couple was diluted five-fold, the difference in rates essentially disappeared however. In solutions of 100 mM TBAI with 8 mM I<sub>2</sub> (and 400

mM TBAClO<sub>4</sub>), the ground state return was fit to a time constant of  $1.3 \pm 0.1 \mu\text{s}$  (similar to that in 100 mM TBAI without I<sub>2</sub>). However, using 100 mM LiI, 8 mM I<sub>2</sub>, and 50 mM AcH (and 400 mM LiClO<sub>4</sub>), the time constant grew to  $0.8 \pm 0.1 \mu\text{s}$  (compared to only 0.3  $\mu\text{s}$  for 100 mM LiI without I<sub>2</sub>).

#### 4.3.2.4 *Regeneration by Ferrocene Derivatives*

Figure 4.11 shows the kinetics of reduction of  $[\text{Ru}^{\text{III}}(\text{H}_2\text{L}')_2(\text{NCS})_2]^+$  by Fc, Me<sub>2</sub>Fc, and Br<sub>2</sub>Fc as a function of  $[\text{Li}^+]$  and  $[\text{H}^+]$  in solution. The concentration of each ferrocene was 25 mM with a supporting electrolyte of either 500 mM TBAClO<sub>4</sub> or 500 mM LiClO<sub>4</sub>–50 mM AcH. In the 500 mM LiClO<sub>4</sub>–50 mM AcH solution, all three ferrocenes regenerated the oxidized dye similarly, with time constants of  $0.35 \pm 0.1 \mu\text{s}$ ,  $0.4 \pm 0.1 \mu\text{s}$  for, and  $0.45 \pm 0.1 \mu\text{s}$  for Fc, Me<sub>2</sub>Fc, and Br<sub>2</sub>Fc respectively. In the 500 mM TBAClO<sub>4</sub> electrolyte, the Br<sub>2</sub>Fc decay is strikingly slower than the other two ferrocenes, with a time constant of  $2.0 \pm 0.2 \mu\text{s}$ , compared to  $0.5 \pm 0.1 \mu\text{s}$  and  $0.5 \pm 0.1 \mu\text{s}$  for Fc and Me<sub>2</sub>Fc respectively (see Table 4.3).

#### 4.3.2.5 *Time-Resolved Emission*

The time-resolved emission from the <sup>3</sup>MLCT state of Ru(H<sub>2</sub>L')<sub>2</sub>(NCS)<sub>2</sub> was measured on ZrO<sub>2</sub> and TiO<sub>2</sub> films, in 500 mM LiClO<sub>4</sub>–50 mM AcH, and 500 mM TBAClO<sub>4</sub>, as well as 500 mM LiI–50 mM AcH and 500 mM TBAI (see Figure 4.12). On ZrO<sub>2</sub>, a broad emission peak was observed from 700 nm to 850 nm, peaking at 800 nm (uncorrected for the changing instrument sensitivity) in all solutions. In contrast, no measurable emission was observed under otherwise identical conditions for TiO<sub>2</sub> films. The emission decay on ZrO<sub>2</sub> was fit to a single exponential decay with a time constant of  $21 \pm 1 \text{ ns}$  (in both electrolytes), consistent with the reported lifetime of the excited state

of the dye in ethanolic or methanolic solution.<sup>20,21</sup> No measurable steady-state emission was observed for  $\text{Ru}(\text{H}_2\text{L}')_2(\text{NCS})_2$  bound to either  $\text{TiO}_2$  or  $\text{ZrO}_2$ .

## 4.4 DISCUSSION

### 4.4.1 Electron Injection into $\text{TiO}_2$

Femtosecond time-resolved absorption measurements were carried out following excitation at 530 nm, the low-energy side of the metal-to-ligand charge transfer (MLCT) transition of  $\text{Ru}(\text{H}_2\text{L}')_2(\text{NCS})_2$ . For visible and near-IR probe wavelengths, the chemical species that dominate the differential absorption spectrum are the excited state ( $[\text{Ru}(\text{H}_2\text{L}')_2(\text{NCS})_2]^*$ ), and the oxidized form ( $[\text{Ru}^{\text{III}}(\text{H}_2\text{L}')_2(\text{NCS})_2]^+$ ) of the dye, which is produced following electron injection into the  $\text{TiO}_2$  conduction band. Due to the overlapping nature of the absorption spectra of these two species, both contribute to the observed absorption vs time trace. Based on previously reported spectra,<sup>22-24</sup> probe wavelengths of 700 nm and 800 nm are dominated by  $[\text{Ru}(\text{H}_2\text{L}')_2(\text{NCS})_2]^*$  and  $\text{Ru}^{\text{III}}(\text{H}_2\text{L}')_2(\text{NCS})_2^+$ , respectively. Ground state absorbance is not significant at either wavelength.

Analogous data were acquired on dye-sensitized  $\text{ZrO}_2$  films (Figures 4.3, 4.5, and 4.7). The very negative conduction band energy of  $\text{ZrO}_2$  of -1.78 V vs NHE in water at pH 13.3 (compared to -0.63 V vs NHE for  $\text{TiO}_2$  at the same pH)<sup>25</sup> precludes interfacial electron transfer at the excitation energies employed, and thus only the dynamics of  $[\text{Ru}(\text{H}_2\text{L}')_2(\text{NCS})_2]^*$  are observed following excitation. Data from  $\text{Ru}(\text{H}_2\text{L}')_2(\text{NCS})_2$  on  $\text{ZrO}_2$  films thus serve as controls, allowing characterization of the dynamics associated with  $[\text{Ru}(\text{H}_2\text{L}')_2(\text{NCS})_2]^*$  in the absence of contributions from  $[\text{Ru}^{\text{III}}(\text{H}_2\text{L}')_2(\text{NCS})_2]^+$ .

Based on the spectra of  $\text{Ru}^{\text{III}}(\text{H}_2\text{L}')_2(\text{NCS})_2]^+$  and  $[\text{Ru}(\text{H}_2\text{L}')_2(\text{NCS})_2]^*$ ,<sup>22-24</sup> transient data at  $\lambda_{\text{probe}} = 700$  nm should consist of a pulse width-limited net absorption increase, due to formation of  $[\text{Ru}(\text{H}_2\text{L}')_2(\text{NCS})_2]^*$ . This is followed by an absorption loss due to formation of  $\text{Ru}^{\text{III}}(\text{H}_2\text{L}')_2(\text{NCS})_2]^+$  by interfacial electron transfer, and/or the formation of the ground state  $\text{Ru}(\text{H}_2\text{L}')_2(\text{NCS})_2$  due to relaxation. In contrast, appearance of  $\text{Ru}^{\text{III}}(\text{H}_2\text{L}')_2(\text{NCS})_2]^+$  will result in a net absorbance increase at  $\lambda_{\text{probe}} = 800$  nm, with a time constant corresponding to the rate of electron injection into the  $\text{TiO}_2$  conduction band.

While in principle relative quantum yields for injection can be determined from transient absorption data, such determinations are fraught with uncertainties because the concentration of dye between different cells was not uniform. Furthermore, since injection occurs from both the initially formed  $^1\text{MLCT}$  and  $^3\text{MLCT}$  states,<sup>26-29</sup> and their relative excited-state extinction coefficients are not known, one cannot quantitate their relative injection yields. Also, our time resolution is insufficient to resolve the kinetics associated with injection out of the  $^1\text{MLCT}$  state.

The net absorption in the  $\text{ZrO}_2$  data, seen at both 700 and 800 nm, is due to the broad absorption of  $[\text{Ru}(\text{H}_2\text{L}')_2(\text{NCS})_2]^*$ . The overall reduction in signal relative to the  $\text{TiO}_2$ -based data (*vide infra*) is due in large part to the decreased loading of  $\text{Ru}(\text{H}_2\text{L}')_2(\text{NCS})_2$  on the  $\text{ZrO}_2$  films. The lack of any further observed dynamics for  $\text{Ru}(\text{H}_2\text{L}')_2(\text{NCS})_2$  on  $\text{ZrO}_2$  films at  $t > 1$  ps is consistent with the  $\sim 21$  ns lifetime observed here and by others<sup>21</sup> for the  $^3\text{MLCT}$  state of this compound, and with no electron injection occurring due to the position of the  $\text{ZrO}_2$  conduction band.

The time scale of the kinetics shown in Figure 4.2 at  $t > 1$  ps suggests that the injection dynamics we are modeling are those associated with the lowest-energy  $^3\text{MLCT}$  state of  $\text{Ru}(\text{H}_2\text{L}')_2(\text{NCS})_2$ . These observations are qualitatively similar to what we and others have observed from time-resolved spectroscopic studies on related systems.<sup>30</sup> Based on previous work,<sup>28,31</sup> it is likely that a significant fraction of the overall interfacial electron transfer process occurs within the initial rise of the transients in Figure 4.2.

Figure 4.2 shows data for solutions with either 500 mM  $\text{TBAClO}_4$  or 500 mM  $\text{LiClO}_4$ –50 mM AcH electrolytes. The plots show that the two solutions exhibit similar dynamics on the picosecond timescale. Both show a fall in absorbance at  $t > 1$  ps at 700 nm (top plot) and a rise at 800 nm (bottom). While the rate constants are slightly different for the two probe wavelengths, they are within experimental error of each other (Table 4.1). Thus, for  $\text{ClO}_4^-$  solutions the addition of small cations does not effect the kinetics at  $t > 1$  ps. Further the absorbance changes are similar in magnitude, and the relative magnitude of the initial absorbance increase compared to the absorbance change  $t > 1$  ps are similar. This suggests that injection from the lowest  $^3\text{MLCT}$  level is not significantly effected by small cations for solutions with  $\text{ClO}_4^-$  anions and that both solutions have similar injection efficiencies from both the singlet and triplet MLCT state.

In Figures 4.4 and 4.6, we show dynamics for solutions containing  $\text{I}^-$ , with and without  $\text{I}_2$  present, respectively. Comparing the traces for solutions containing  $\text{Li}^+$  and AcH in Figures 4.4 and 4.6 shows that injection dynamics and amplitudes (both absolute and relative) are largely independent of whether the solution contains  $\text{I}_2$ . For these traces, at both 700 and 800 nm, the fitted time-constant of the rise or fall in all the curves are the same within experimental error. For solutions with no small cations ( $\text{TBA}^+$  only), the

situation is notably different (although again the curves with or without  $I_2$  are similar). None of the  $TBA^+$ -based solutions show clear kinetics on the  $t > 1$  ps time scale. While there are changes in absorbance on this time scale, the low signal-to-noise ratio makes it difficult to distinguish. Thus for all solutions containing  $I^-$ , the presence or absence of  $I_2$  does not change the kinetics, but unlike for the  $ClO_4^-$ -based solutions, a distinct difference is observed between solutions of only  $TBA^+$  and those containing  $Li^+$  and AcH.

Comparing the dynamics measured in the presence of  $I^-$  in solutions with  $TBA^+$  to those with  $Li^+$  and AcH: while both solutions show significant injection at very short times, the  $TBA^+$ -based solutions do not show any clear evidence of injection on the longer times ( $t > 1$  ps) while the  $Li^+$  solutions do. In Figure 4.4 solutions with  $I_2$  and either TBAI or LiI with 50 AcH are directly compared. For solutions containing  $I^-$  (with or without  $I_2$ ), we observed that the  $TBA^+$  solution shows no slow injection, while the solutions with  $Li^+$  and  $H^+$  do. It is somewhat surprising that the amplitude of the two signals in Figure 4.4a are similar but this is partially coincidental, since different  $TiO_2$  films can have different concentrations of absorbed dye. However, the fact that the two amplitudes are similar at long time delays does suggest that the total number of electrons injected into the  $TiO_2$  does not vary by an order of magnitude, as do the values of  $J_{sc}$  as measured by  $J-E$  curves in Chapter 3.

That no emission is observed from the dye on  $TiO_2$  in all solutions (Figure 4.12) suggests that the dye is well quenched by the  $TiO_2$ , in both the presence and absence of small cations. In contrast, emission from the dye bound to  $ZrO_2$  is observed and no injection dynamics are observed. Thus we conclude that, on the  $TiO_2$ , while the injection

rate may decrease from the  $^3\text{MLCT}$  state of the dye when no small cations are present, the overall quantum yield for electron injection is still relatively high on  $\text{TiO}_2$  with and without small cations.

Given that the potential of the conduction band (and acceptor levels) are shifted negative by approximately -1 V in  $\text{TBA}^+$ -based electrolytes relative to those with  $\text{Li}^+$ - $\text{AcH}$ ,<sup>16</sup> one may ask why injection still takes place, especially in light of the fact that the dye does not inject into  $\text{ZrO}_2$  in any solution. One way for this to occur is if the redox potential of the dye moves in tandem with the changes in energy of the conduction band of the  $\text{TiO}_2$ , as shown in Figure 4.13, Cases C and D. Decreasing the concentration of small cations shifts the density of acceptor states of the  $\text{TiO}_2$  to more negative potentials.<sup>16</sup> Since the dye is adsorbed onto the surface of the  $\text{TiO}_2$ , this shift in surface potential may be felt by the dye, causing the ground state potential to shift in tandem. One might expect that the extent of the shift of the dye's potential would depend on both the cations and anions present in solution, and thus the extent of the dye's shift may vary for different electrolyte solutions.

If the reduction potential dye shifts to the same degree as does the  $\text{TiO}_2$  (Figure 4.13, Case C) one would expect that injection from the dye would not change, as observed in the solutions with  $\text{ClO}_4^-$  anions (Figure 4.2). However, in solution with other anions, such as  $\text{I}^-$  or  $\text{I}^-/\text{I}_3^-$ , the dye may not fully shift in tandem with the surface, reducing the thermodynamic driving force for electron injection (Case D). In this case, the injection from the triplet state of the dye would be suppressed, while injection from the higher-energy singlet state would be less effected by electrolyte cations.

In any case, the injection dynamics measured in a working solar cell (whose steady-state electrochemical properties had also been measured as described in Chapter 3) suggest that the extent of electron injection from the  $^3\text{MLCT}$  state of  $\text{Ru}(\text{H}_2\text{L}')_2(\text{NCS})_2$  is attenuated for the 500 mM TBAI–40 mM  $\text{I}_2$  electrolytes compared to those with 500 mM LiI–40 mM  $\text{I}_2$ –50 mM AcH. The injection dynamics and transient spectra observed for 500 mM TBAI and 500 mM TBAI–40 mM  $\text{I}_2$  solutions suggest that while the excited state dye potential shifts with changes in the potential of the surface, they do not move fully in concert with that shift (as in Figure 4.13, case D).

We have shown that the external quantum yield drops by a factor of five across the entire absorption spectrum of the dye as the conduction band edge is shifted negative by as little as 150 mV.<sup>16</sup> The spectral response indicates that the loss of photocurrent is not a strong function of the energy of the incident photon, consistent with  $E_{inj}$  being approximately constant in all electrolytes. This coupled with the lack of emission of the dye attached to  $\text{TiO}_2$ , and the similarity in absorbance changes in all the observed cells suggests that injection efficiency is not the cause of the lost in  $J_{sc}$  that was observed previously.

#### 4.4.2 Reduction of $[\text{Ru}^{\text{III}}(\text{H}_2\text{L}')_2(\text{NCS})_2]^+$

The kinetics of the reduction of the oxidized dye were studied by nanosecond transient absorption, monitoring the bleach of the ground-state MLCT absorption of  $\text{Ru}(\text{H}_2\text{L}')_2(\text{NCS})_2$  at 560 nm. In the absence of a redox couple in solution, following dye excitation and electron injection, an electron in  $\text{TiO}_2$  will reduce the oxidized dye. In contrast, in the presence of a kinetically viable reducing species in solution, the dye instead will be regenerated to the reduced state by that redox species (as in Figure 4.1).

In all cases, because no external circuit was connected to the cell in these measurements, any injected electrons must ultimately recombine at the TiO<sub>2</sub> interface with either the oxidized dye or hole carriers in solution, with no net chemical change (in the absence of side reactions due to impurities or oxygen).

Figure 4.9 shows that the regeneration rate of Ru<sup>III</sup>(H<sub>2</sub>L')<sub>2</sub>(NCS)<sub>2</sub>]⁺ by I⁻ is significantly diminished as either [Li⁺] or [H⁺] in the contacting solution is decreased. If the regeneration rate is significantly decreased in a DSSC, the photocurrent will be reduced, either due to competing recombination reactions or to a steady-state buildup in the concentration of oxidized dye. Thus, the slower dye reduction rate may also explain the loss of photocurrent in TBA⁺-based solutions described in Chapter 3. Furthermore, it is consistent with the monotonic drop in the action spectrum, as dye regeneration is not a photo-driven process itself. The decreased reduction rate is also consistent with the slow drop in photocurrent over the course of several hours, presumably as the concentration of oxidized dye builds up on the surface of the TiO<sub>2</sub>. The change in regeneration rate as a function of [Li⁺] and/or [H⁺] thus provides a self-consistent explanation of both the electron injection dynamics discussed above and the observed steady-state properties measured previously, and suggests a model such as in Case D in Figure 4.13.

The reduction rate in a solution of 100 mM LiI, 8 mM I<sub>2</sub>, and 50 mM AcH ( $\tau = 1100 \pm 100$ ) was much slower than in the same solution without I<sub>2</sub> ( $\tau = 300 \pm 30$ ). And yet at 500 mM I⁻, the presence of 40 mM I<sub>2</sub> did not significantly affect the measured rate of regeneration of Ru<sup>III</sup>(H<sub>2</sub>L')<sub>2</sub>(NCS)<sub>2</sub>]⁺ in both Li⁺- and TBA⁺-based solutions. The reason for this remains unclear.

The similarity of the traces in Figure 4.8 shows that the recombination rate was not sensitive to the concentration of small cations in solution. This further supports a model in which the ground state potential of the dye is shifted to a similar extent as the conduction band edge energy, thereby keeping the driving force of the reaction constant. Hupp et al. observed a similar insensitivity to recombination rate for another Ru-based dye (hexaphosphonated  $\text{Ru}(\text{bpy})_3^{2+}$ ) as a function of pH in aqueous solution, attributed initially to change in ground-state redox potential of the dye due to the pH.<sup>32</sup> That argument was refuted by further spectroelectrochemical studies of the same dye.<sup>33</sup>

However, using a potentiometric titration by chemical oxidation, Gregg et al. found that several other Ru-based dyes *did* have ground state redox potentials which were affected by either the pH of an aqueous solution, or by the size of the electrolyte cation in  $\text{CH}_3\text{CN}$ , but only when the dye was bound to  $\text{TiO}_2$ , rather than free in solution.<sup>34,35</sup> Greg and coworkers proposed an explanation based on the changing thickness of the double layer at the  $\text{TiO}_2$ -electrolyte interface as a function of cation size. A relatively large cation, such as  $\text{TBA}^+$ , allows the dye to be fully within the potential drop at the interface. In the presence of smaller cations, the electric field is dropped across a shorter distance. In this case, the dye is largely outside of the double layer, and so its potential is independent of the  $\text{TiO}_2$  flat-band potential. The insensitivity to the cation size in the recombination kinetics, despite a measured band-edge shift on the order of  $-1 \text{ V}$ ,<sup>16</sup> combined with the decrease in regeneration rate with the  $\text{TBA}^+$ -based electrolyte, as discussed below, is strong evidence that the ground-state redox potential of the  $\text{Ru}(\text{H}_2\text{L}')_2(\text{NCS})_2$  dye is shifted by changes in  $E_{\text{accept}}$ .

Direct measurement of the reduction potential of the sensitizer bound to TiO<sub>2</sub> was not possible. Measurement by cyclic voltammetry was not possible due to the low conductivity of the TiO<sub>2</sub> in the dark, as reported elsewhere.<sup>36</sup> Applying a bias to a sensitized TiO<sub>2</sub> film in the dark, no significant current was passed until the percolation threshold, and no peak due to dye oxidation or reduction was observed. Measurement by potentiometric titration was precluded by the irreversible chemical oxidation of Ru(H<sub>2</sub>L')<sub>2</sub>(NCS)<sub>2</sub>. Because of this experimental limitation, the shift in the position of the ground state redox potential was deduced from the kinetic data, namely recombination with free electrons in TiO<sub>2</sub> and of regeneration by electron donors in solution. Taken together, these measurements show that dye potential is indeed affected by the electrolyte cations.

In addition, consistent with *J-E* curves, spectrochronocoulometric and spectral response measurements reported in Chapter 3, electrolytes with 500 mM TBAI and 50 mM AcH added showed nearly identical kinetics as those with 500 mM LiI–50 mM AcH (data not shown). As in the steady-state measurements in Chapter 3, it is thus the presence of potential-determining cations that affects the regeneration rate rather than the presence of TBA<sup>+</sup>.

Other investigations on the effect of small cations on the regeneration rate of the oxidized dye have attributed the lowered rate to a change in the zeta potential of the TiO<sub>2</sub> surface, rather than to a change in the ground state reduction potential of the dye.<sup>15</sup> The authors proposed that an electric field at the interface, formed by a more negatively charged surface due to the lack of chemisorbed and/or intercalated cations, affects the formation of I<sup>-</sup>-I<sup>-</sup> ion pairs on the surface, and thereby changes the oxidation mechanism

of iodide. It is well established that the intercalation and adsorption of small cations does cause a shift in the zeta potential of  $\text{TiO}_2$ .<sup>15,37,38</sup> However a shift in the zeta potential should not affect a neutral, single-electron, outer-sphere reducing agent, e.g., ferrocene. Thus, to establish whether the reduction in regeneration rate of the dye by  $\text{I}^-$  was due to a shift in the ground state potential or to the changing zeta potential, the regeneration rate was measured for ferrocene (Fc) and two derivatives—dimethyl ferrocene ( $\text{Me}_2\text{Fc}$ ) and dibromoferrocene ( $\text{Br}_2\text{Fc}$ )—covering a range of redox potentials (0.21 V, 0.31 V, and 0.55 V vs SCE for  $\text{Me}_2\text{Fc}$ , Fc, and  $\text{Br}_2\text{Fc}$  respectively).<sup>39</sup>

Fc and  $\text{Me}_2\text{Fc}$  both regenerate  $\text{Ru}^{\text{III}}(\text{H}_2\text{L}')_2(\text{NCS})_2]^+$  effectively in all electrolytes tested here. Their use in a working solar cell is precluded however by a much greater dark current than for  $\text{I}^-/\text{I}_3^-$  (rate  $k_5$  in Figure 4.1 is much larger for the ferrocenes than for  $\text{I}_3^-$ ) effectively short-circuiting the cell such that every injected electron is lost to reduction of ferrocenium at the  $\text{TiO}_2$  interface.<sup>40</sup> However, in the nanosecond TA measurements, the cell was not connected to any external circuit and no appreciable amount of ferrocenium is built up in solution.

In 500 mM  $\text{LiClO}_4$ –50 mM AcH solutions, at a concentration of 25 mM, all three ferrocenes were capable of reducing  $\text{Ru}^{\text{III}}(\text{H}_2\text{L}')_2(\text{NCS})_2]^+$  at rate competitive with recombination as shown in Figure 4.11. In 500 mM  $\text{TBAClO}_4$  solutions, this was only true for Fc and  $\text{Me}_2\text{Fc}$ . In contrast the rate of regeneration by  $\text{Br}_2\text{Fc}$  was significantly decreased. Note that the decay time constant of the recombination reaction is in fact laser-intensity dependent,<sup>20</sup> which accounts for the difference in the upper limit for the regeneration time constants between the  $\text{I}^-$  and Fc regeneration measurements.

As a neutral single-electron outer-sphere reducing agent, Br<sub>2</sub>Fc should not be affected by a change in zeta potential, and so the change in regeneration rate is strong evidence that the ground state of the dye is indeed shifted to more negative potentials in the absence of small cations in solution. That both Fc and Me<sub>2</sub>Fc are still kinetically competent, but Br<sub>2</sub>Fc is not, puts an upper and lower limit on the shift of the dye reduction potential.

#### 4.5 CONCLUSIONS

In conclusion, we have determined the thermodynamic and kinetic effects of small cations (H<sup>+</sup> and Li<sup>+</sup>) in the electrolyte solution on the steady-state properties of DSSC's in both the light and in the dark. In Chapter 3, we established that the increase in photovoltage is indeed due to a shift in the conduction band edge of TiO<sub>2</sub> as a function of the concentration of potential-determining cations in solution in electrolytes with either ClO<sub>4</sub><sup>-</sup> or I<sup>-</sup>/I<sub>2</sub>. In this second paper, using time-resolved measurements, we have shown that loss of current is primarily due to a decrease in the regeneration rate of the oxidized Ru(H<sub>2</sub>L')<sub>2</sub>(NCS)<sub>2</sub> dye by I<sup>-</sup>.

There is strong evidence that this is due to a shift in the reduction potential of the ground and excited states of the dye as a function of [Li<sup>+</sup>] and [H<sup>+</sup>], resulting in a decreased driving force for regeneration,  $E_{regen}$ , rather than the initially expected change in electron injection rate (due to a change in  $E_{inj}$ ). This is also supported by the unchanged rate of recombination for injected electrons in TiO<sub>2</sub> with the oxidized dye. Although the injection dynamics from the triplet state in I<sup>-</sup>/I<sub>2</sub> electrolytes are different for the two electrolytes compared here, the lack of emission from the [Ru(H<sub>2</sub>L')<sub>2</sub>(NCS)<sub>2</sub>]\*

state on  $\text{TiO}_2$  is consistent with efficient electron injection. The conclusion that the ground and excited state reduction potentials are shifting with  $E_{accept}$  is also supported by the spectral response data presented in Chapter 3, which showed that the external quantum yield drops across the entire spectrum. The difference in picosecond dynamics (as well as the changes in the internal quantum yield measured previously) is indicative of a secondary, albeit minor, effect: while the potential of both the ground and excited states of the dye are shifted, the driving force for injection has nonetheless been affected, reducing the efficiency of the injection from the triplet state in solution containing no small cations.

Finally, the TA data using ferrocene and two derivatives as reducing agents indicates that the change in regeneration rate is not due to surface charge or a change in the zeta potential of the  $\text{TiO}_2$ , but rather a change in the reduction potential of the ground state of  $\text{Ru}(\text{H}_2\text{L}')_2(\text{NCS})_2$  on the  $\text{TiO}_2$  surface. These results have important implications for the design of DSSC's, indicating that the energetics of the  $\text{TiO}_2$  and the dye may be closely coupled.

**Table 4.1** Femtosecond-resolved transient absorbance data: Electron injection

Film	$\lambda_{\text{obsd}}$	500 mM TBAClO <sub>4</sub>	500 mM TBAI, 40 mM I <sub>2</sub>	500 mM TBAI	500 mM LiClO <sub>4</sub> , 50 mM AcH	500 mM LiI, 40 mM I <sub>2</sub> , 50 mM AcH	500 mM LiI, 50 mM AcH
	nm	ps	ps	ps	ps	ps	ps
TiO <sub>2</sub>	700	9.0 ± 1.2	-	-	9.2 ± 1.3	28 ± 8	15 ± 3
TiO <sub>2</sub>	800	10 ± 2	13 ± 5	22 ± 8	7 ± 2	15 ± 5	16 ± 2

**Table 4.2** Nanosecond-resolved transient absorbance data: Recombination and regeneration by I<sup>-</sup>

Film	[I <sub>2</sub> ] M	500 mM TBAClO <sub>4</sub>	500 mM TBAI	100 mM TBAI	500 mM LiClO <sub>4</sub> , 50 mM AcH	500 mM LiI, 50 mM AcH	100 mM LiI, 50 mM AcH
	M	ns	ns	ns	ns	ns	ns
TiO <sub>2</sub>	-	1000 ± 100	350 ± 20	1100 ± 100	1000 ± 100	17 ± 5	300 ± 30
TiO <sub>2</sub>	0.04	-	280 ± 20	-	-	20 ± 5	-
TiO <sub>2</sub>	0.08	-	-	1300 ± 100	-	-	800 ± 100

**Table 4.3** Nanosecond-resolved transient absorbance data: Regeneration by ferrocenes<sup>a</sup>

Film	Ferrocene (25 mM)	500 mM TBAClO <sub>4</sub> ,	500 mM LiClO <sub>4</sub> , 50 mM AcH
	Type	ns	ns
TiO <sub>2</sub>	Fc	500 ± 100	350 ± 100
TiO <sub>2</sub>	Me <sub>2</sub> Fc	400 ± 100	400 ± 100
TiO <sub>2</sub>	Br <sub>2</sub> Fc	2000 ± 200	450 ± 100

<sup>a</sup> Excited at 520 nm, probe at 560 nm

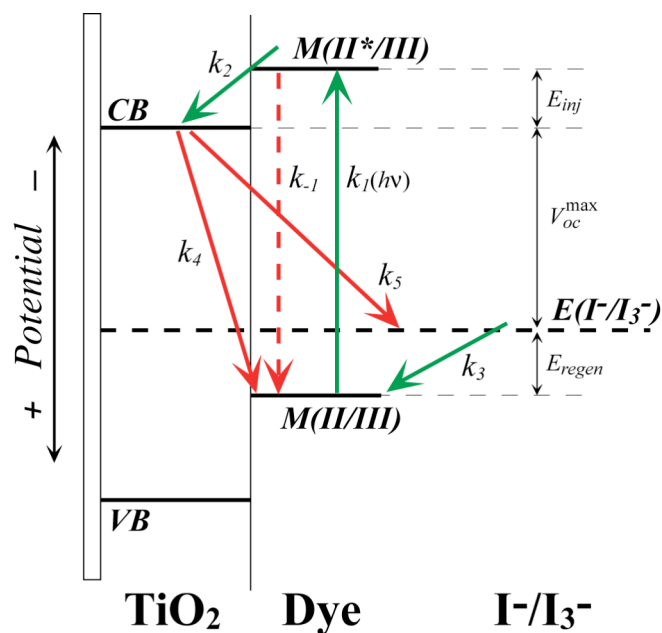


**Figure 4.1** Diagram showing the principal electron-transfer reactions of a DSSC: electronic excitation and de-excitation of the sensitizer,  $k_1$  and  $k_{-1}$ , respectively; electron injection from the sensitizer excited state into the TiO<sub>2</sub> film,  $k_2$ , with driving force  $E_{inj}$ ; regeneration of the oxidized dye by the solution redox couple (I<sub>3</sub><sup>-</sup>/I<sup>-</sup>),  $k_3$ , with driving force  $E_{regen}$ ; recombination reaction of oxidized dye with TiO<sub>2</sub> electron,  $k_4$ ; and loss reaction of oxidized solution couple with TiO<sub>2</sub> electron,  $k_5$ . CB and VB are the conduction and valence band edges respectively and  $V_{oc}^{max}$  is the maximum open circuit voltage. Lines indicate the redox potentials of the various species with more negative reduction potentials higher.

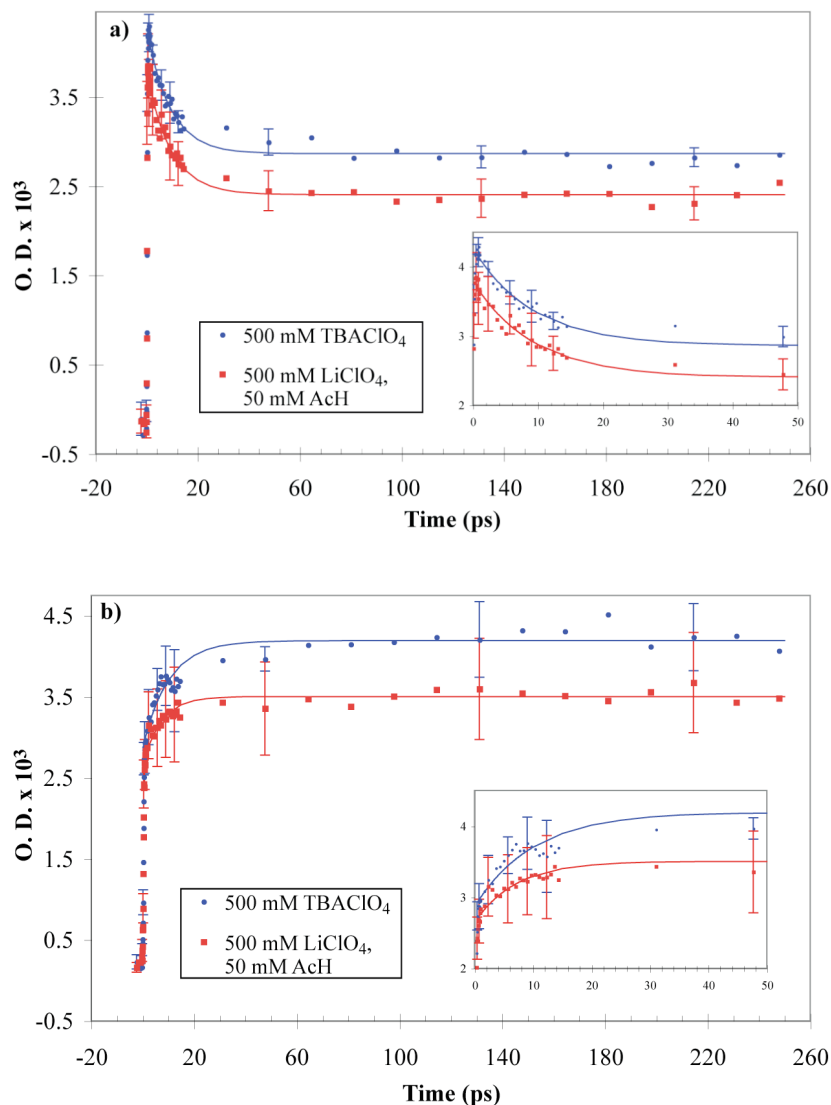


**Figure 4.2** Transient absorption data for TiO<sub>2</sub> films sensitized with Ru(H<sub>2</sub>L')<sub>2</sub>(NCS)<sub>2</sub> in contact with CH<sub>3</sub>CN solutions containing 500 mM TBAClO<sub>4</sub> (blue circles) or 500 mM LiClO<sub>4</sub> and 50 mM AcH (red squares). The data were obtained following ~ 100 fs excitation at 530 nm. **(a)**  $\lambda_{\text{probe}} = 700$  nm. The solid lines correspond to fits with  $\tau_{\text{obs}}^{\text{TBAClO}_4} = 9.0 \pm 1.2$  ps and  $\tau_{\text{obs}}^{\text{LiClO}_4} = 9.2 \pm 1.3$  ps. **(b)**  $\lambda_{\text{probe}} = 800$  nm. The solid lines correspond to fits with  $\tau_{\text{obs}}^{\text{TBAClO}_4} = 10 \pm 2$  ps and  $\tau_{\text{obs}}^{\text{LiClO}_4} = 7 \pm 2$  ps. The insets show the early time behavior.

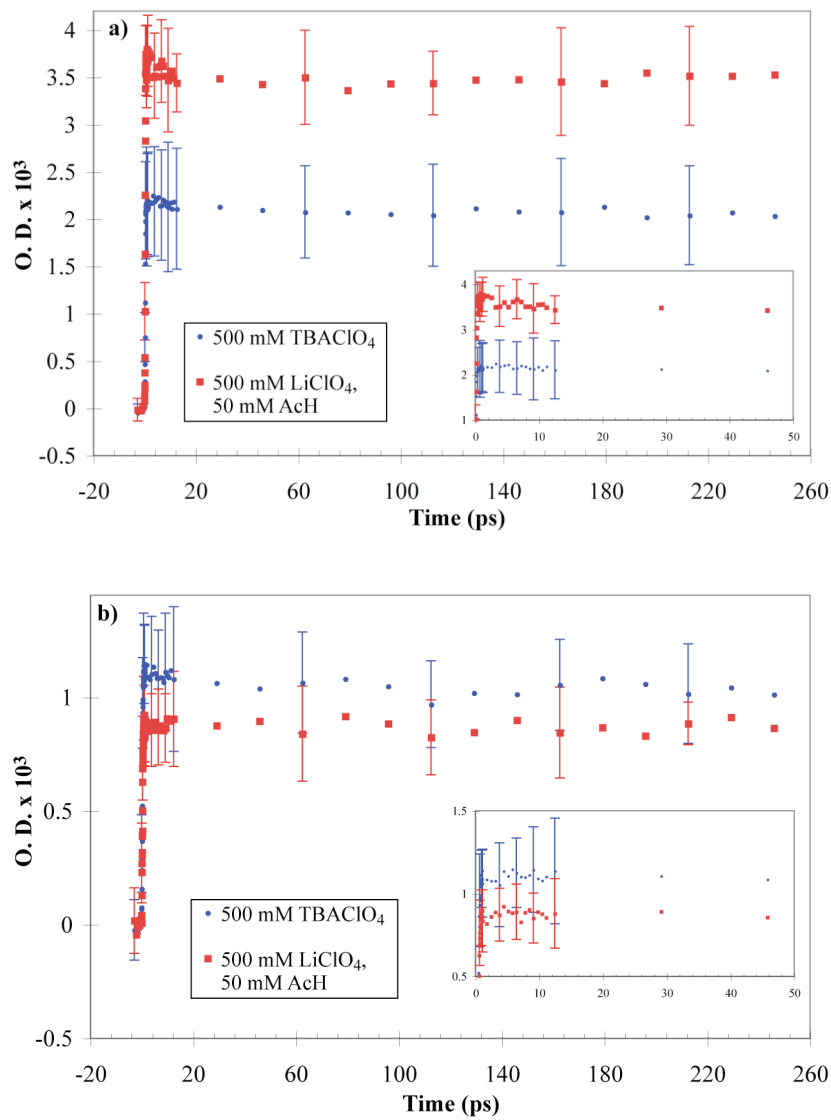


**Figure 4.3** Transient absorption data for ZrO<sub>2</sub> films sensitized with Ru(H<sub>2</sub>L')<sub>2</sub>(NCS)<sub>2</sub> in contact with CH<sub>3</sub>CN solutions containing 500 mM TBAClO<sub>4</sub> (blue circles) or 500 mM LiClO<sub>4</sub> and 50 mM AcH (red squares), analogous to data on TiO<sub>2</sub> presented in Figure 4.2. **(a)**  $\lambda_{\text{probe}} = 700$  nm. **(b)**  $\lambda_{\text{probe}} = 800$  nm. The insets show the early time behavior.

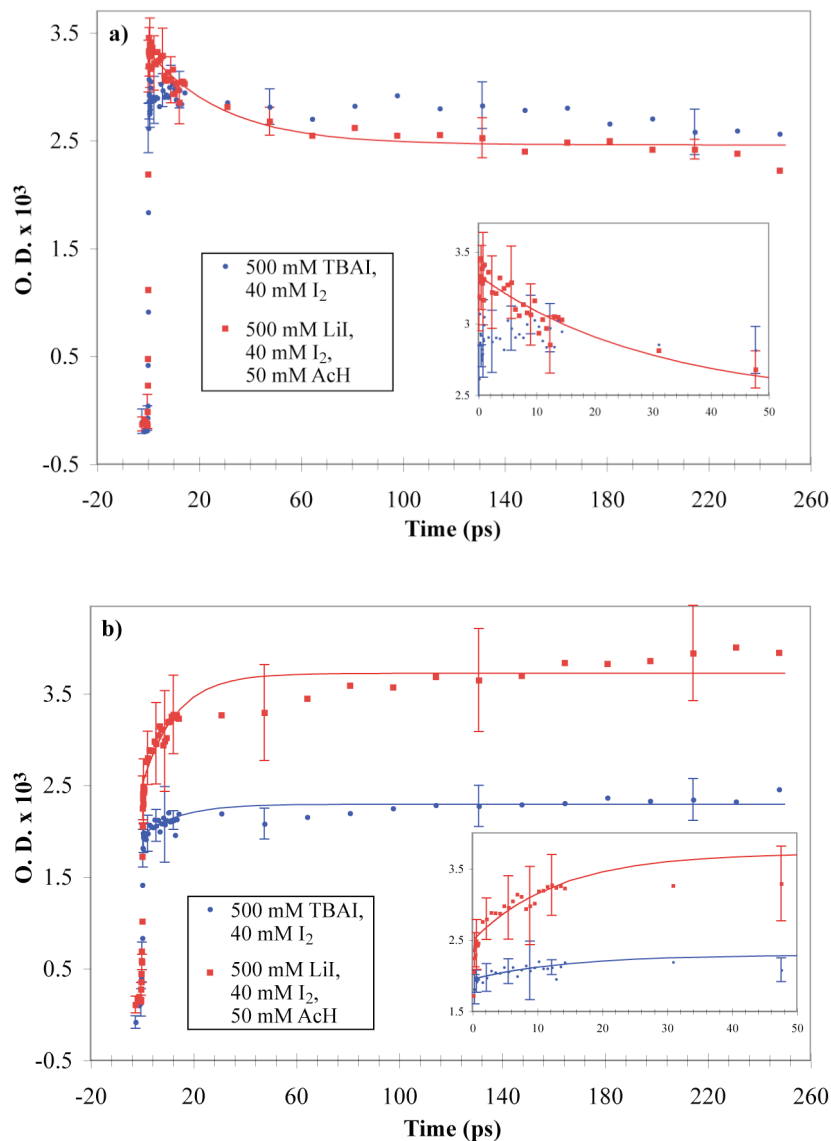


**Figure 4.4** Transient absorption data for TiO<sub>2</sub> films sensitized with Ru(H<sub>2</sub>L')<sub>2</sub>(NCS)<sub>2</sub> in contact with CH<sub>3</sub>CN solutions containing 500 mM TBAI and 40 mM I<sub>2</sub> (blue circles) or 500 mM LiI, 40 mM I<sub>2</sub>, and 50 mM AcH (red squares). The data were obtained following ~ 100 fs excitation at 530 nm. **(a)**  $\lambda_{\text{probe}} = 700$  nm. The solid line corresponds to a fit with  $\tau_{\text{obs}}^{\text{LiI/I}_2} = 28 \pm 8$  ps. **(b)**  $\lambda_{\text{probe}} = 800$  nm. The solid lines correspond to fits with  $\tau_{\text{obs}}^{\text{TBAI/I}_2} = 13 \pm 5$  ps and  $\tau_{\text{obs}}^{\text{LiI/I}_2} = 14 \pm 3$  ps. The insets show the early time behavior.

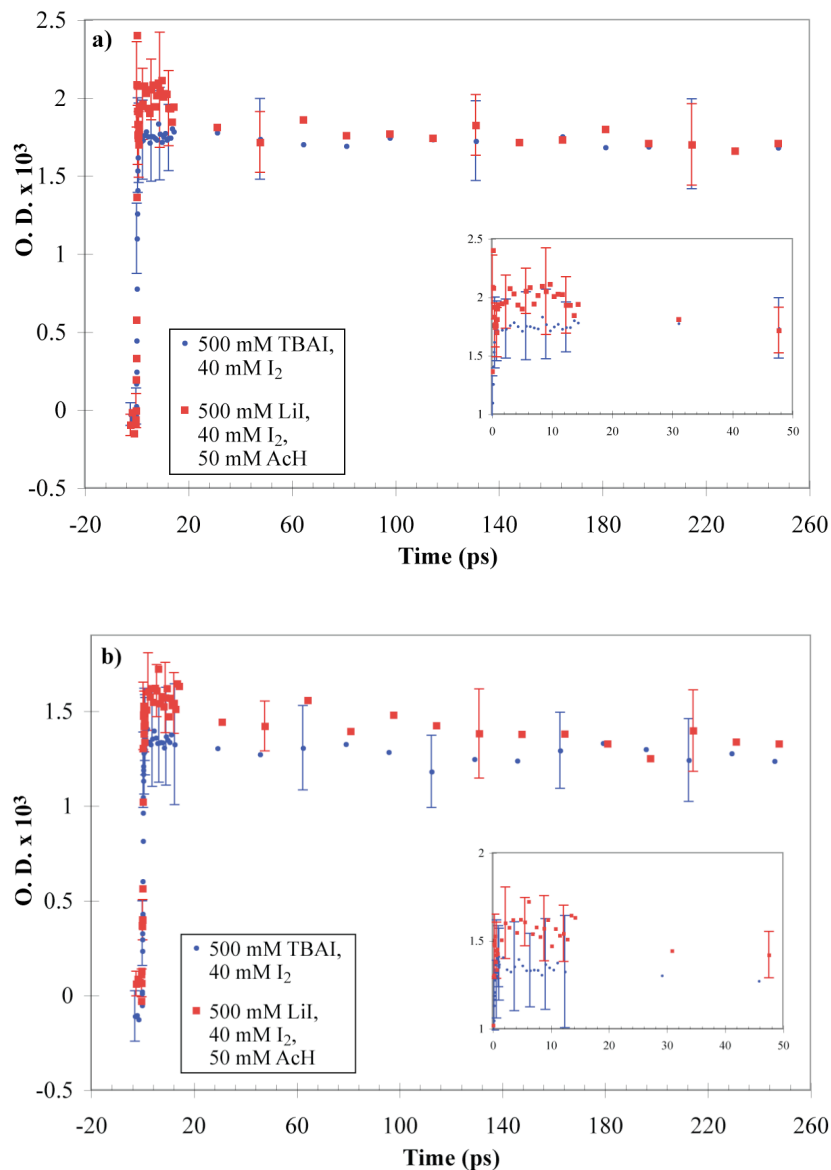


**Figure 4.5** Transient absorption data for  $ZrO_2$  films sensitized with  $Ru(H_2L')_2(NCS)_2$  in contact with  $CH_3CN$  solutions containing 500 mM TBAI and 40 mM  $I_2$  (blue circles) or 500 mM LiI, 40 mM  $I_2$ , and 50 mM AcH (red squares), analogous to data on  $TiO_2$  presented in Figure 4.4. **(a)**  $\lambda_{\text{probe}} = 700$  nm. **(b)**  $\lambda_{\text{probe}} = 800$  nm. The insets show the early time behavior.

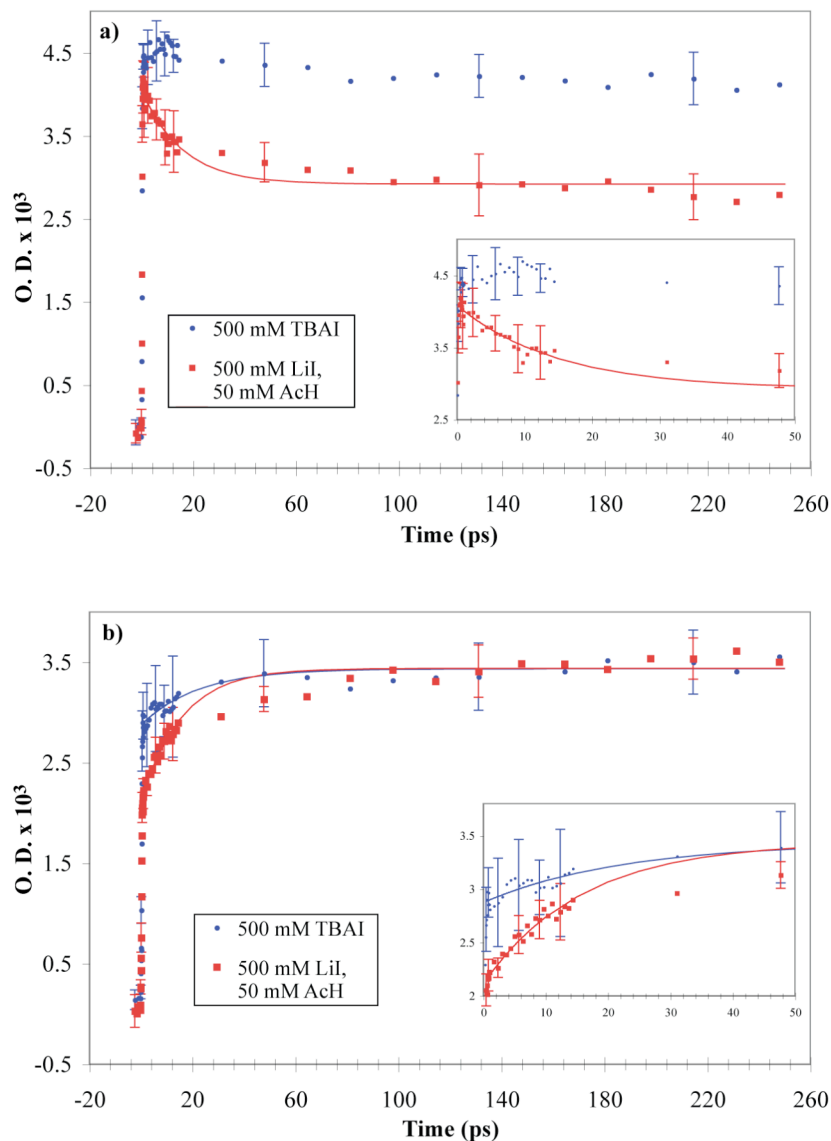


**Figure 4.6** Transient absorption data for TiO<sub>2</sub> films sensitized with Ru(H<sub>2</sub>L')<sub>2</sub>(NCS)<sub>2</sub> in contact with CH<sub>3</sub>CN solutions containing 500 mM TBAI, 40 mM I<sub>2</sub> (blue circles) or 500 mM LiI, 40 mM I<sub>2</sub>, and 50 mM AcH (red squares). The data were obtained following ~ 100 fs excitation at 530 nm. **(a)**  $\lambda_{\text{probe}} = 700$  nm. The solid line corresponds to a fit with  $\tau_{\text{obs}}^{\text{LiI}} = 15 \pm 3$  ps. **(b)**  $\lambda_{\text{probe}} = 800$  nm. The solid lines correspond to fits with  $\tau_{\text{obs}}^{\text{TBAI}} = 22 \pm 8$  ps and  $\tau_{\text{obs}}^{\text{LiI}} = 15 \pm 3$  ps. The insets show the early time behavior.

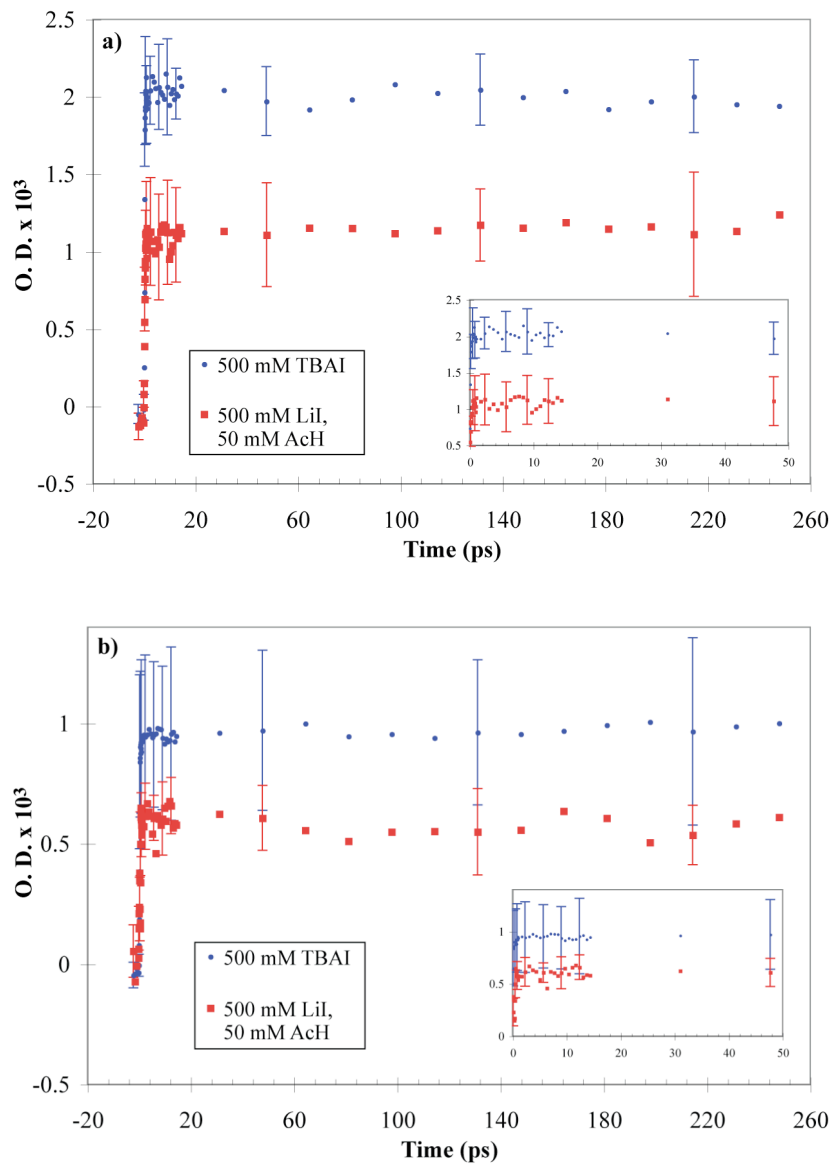


**Figure 4.7** Transient absorption data for  $\text{ZrO}_2$  films sensitized with  $\text{Ru}(\text{H}_2\text{L}')_2(\text{NCS})_2$  in contact with  $\text{CH}_3\text{CN}$  solutions containing 500 mM TBAI, 40 mM  $\text{I}_2$  (blue circles) or 500 mM LiI, 40 mM  $\text{I}_2$ , and 50 mM AcH (red squares), analogous to data on  $\text{TiO}_2$  presented in Figure 4.6. **(a)**  $\lambda_{\text{probe}} = 700$  nm. **(b)**  $\lambda_{\text{probe}} = 800$  nm. The insets show the early time behavior.

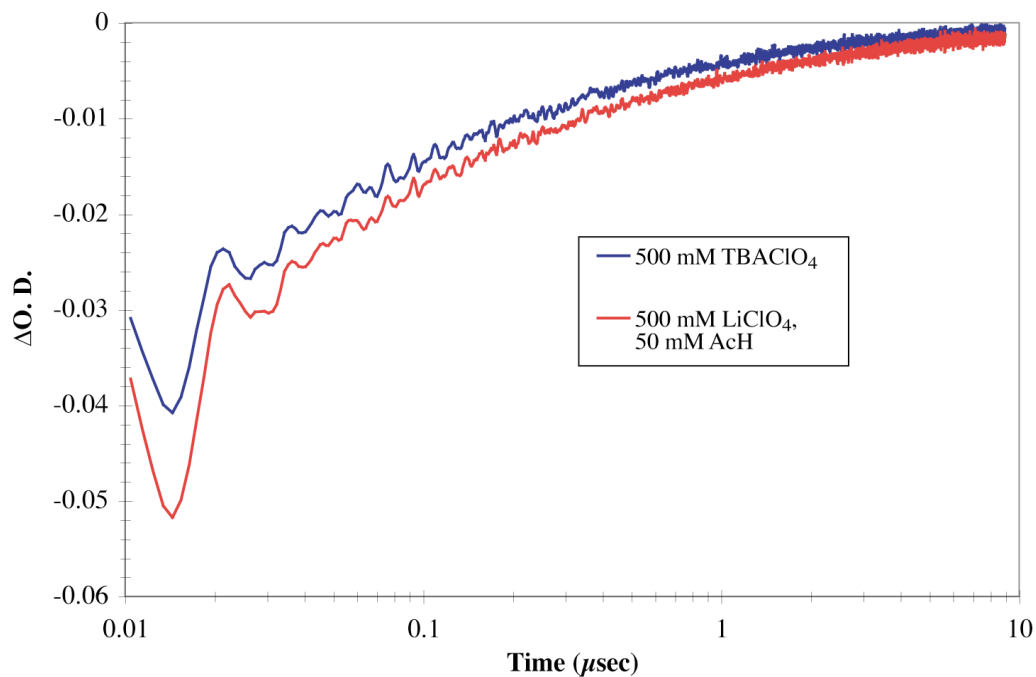


**Figure 4.8** Transient absorption traces monitoring the recombination reaction of  $\text{Ru}(\text{H}_2\text{L}')_2(\text{NCS})_2$  with injected electrons from  $\text{TiO}_2$  in a  $\text{CH}_3\text{CN}$  solution of 500 mM  $\text{LiClO}_4$  with 50 mM AcH and 500 mM  $\text{TBAClO}_4$ . Samples were excited at 530 nm and monitored at 560 nm.

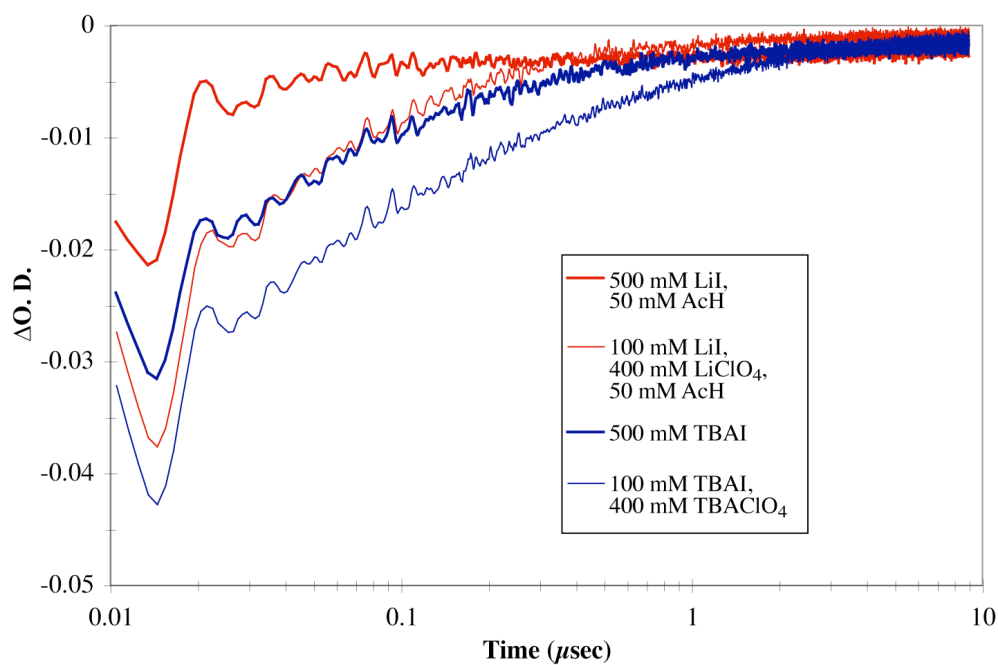


**Figure 4.9** Transient absorption traces showing the regeneration kinetics of  $\text{Ru}(\text{H}_2\text{L}')_2(\text{NCS})_2$  on  $\text{TiO}_2$  in the contact with  $\text{CH}_3\text{CN}$  solutions of  $\text{I}^-$ . The ground state recovery was measured by ns-TA, monitoring the bleach of the  $^3\text{MLCT}$  at 560 nm. Using 0.50 M LiI with 50 mM AcH, the trace is an upper bound, limited by the instrument response; using 0.10 M TBAI, the rate is a lower bound, limited by competition with the recombination reaction.

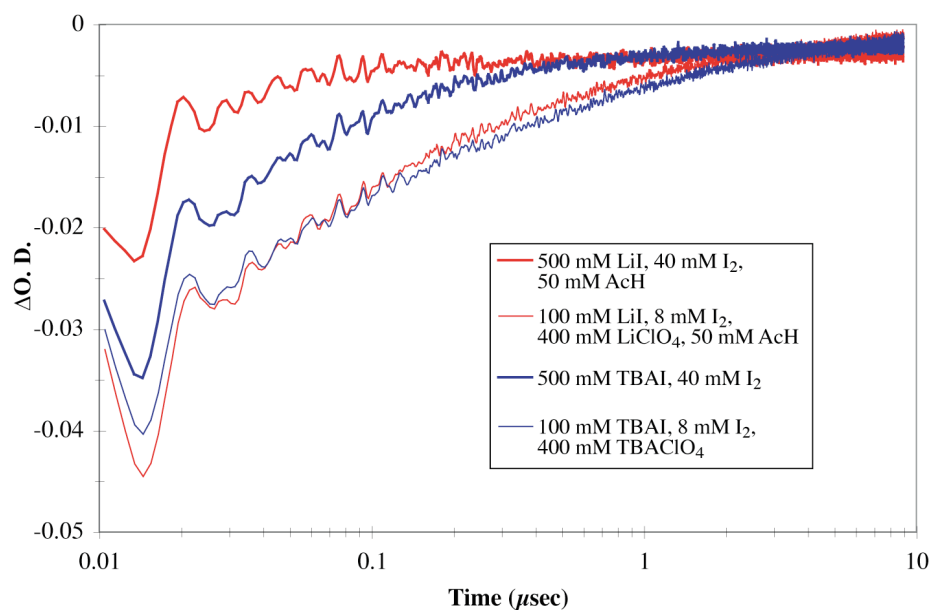


**Figure 4.10** Transient absorption traces showing the regeneration kinetics of  $\text{Ru}(\text{H}_2\text{L}')_2(\text{NCS})_2$  on  $\text{TiO}_2$  in the contact with  $\text{CH}_3\text{CN}$  solutions of  $\text{I}^-$  and  $\text{I}_3^-$ . The ground state recovery was measured by ns-TA, monitoring the bleach of the  $^3\text{MLCT}$  at 560 nm. Note that in the presence of  $\text{I}_2$ , the difference in rates between solutions with  $\text{Li}^+$  and AcH and TBA $^+$  only essentially disappeared at lower concentrations of the redox couple. This is in contrast to rates with only  $\text{I}^-$  present, where solutions with TBA $^+$  only were significantly slower than the corresponding one with  $\text{Li}^+$  and AcH at all concentrations.

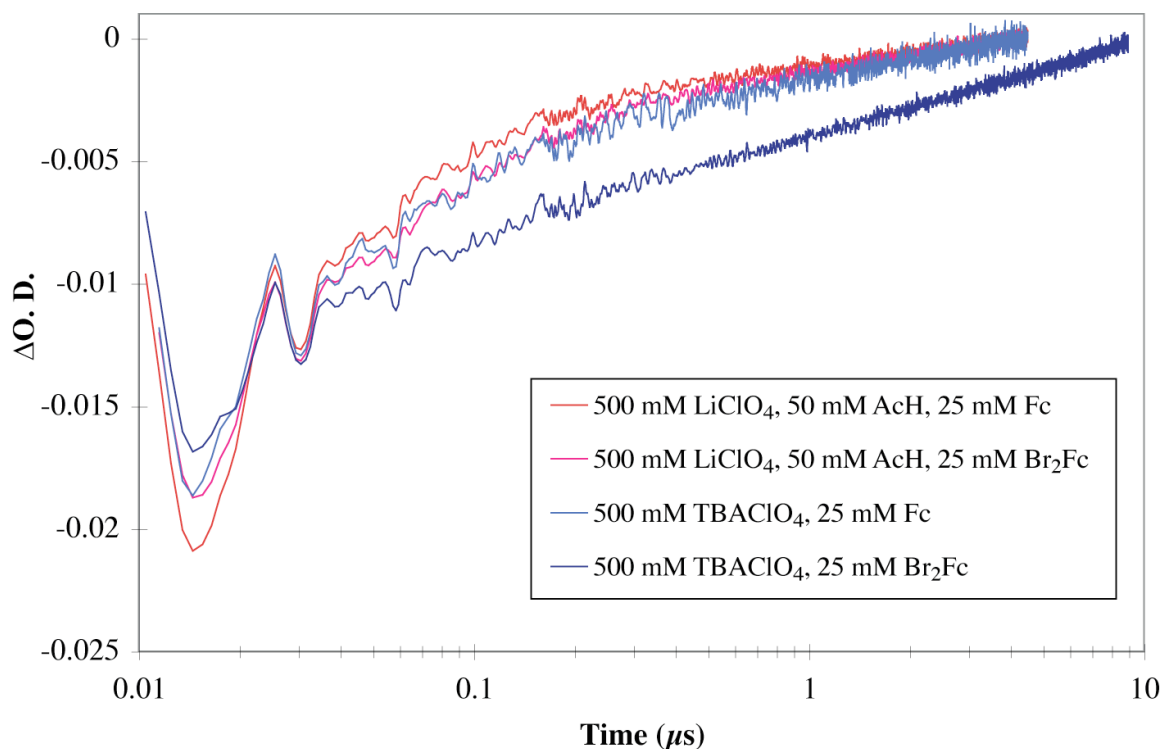


**Figure 4.11** Transient absorption traces showing the regeneration kinetics of  $\text{Ru}(\text{H}_2\text{L}')_2(\text{NCS})_2$  on  $\text{TiO}_2$  in the contact with a  $\text{CH}_3\text{CN}$  solution of 25 mM ferrocene (Fc) and 1,1'-dibromoferrocene ( $\text{Br}_2\text{Fc}$ ) in solution. In the presence of Fc and  $\text{Me}_2\text{Fc}$ , the dye was reduced equally quickly in both electrolytes of 500 mM  $\text{TBAClO}_4$  as well as 500 mM  $\text{LiClO}_4$ –50 mM  $\text{AcH}$ . In contrast to Fc and  $\text{Me}_2\text{Fc}$ , which have more negative reduction potentials,  $\text{Br}_2\text{Fc}$  was not able to regenerate the oxidized dye in the 500 mM  $\text{TBAClO}_4$  electrolyte, but did do so in the presence of 500 mM  $\text{LiClO}_4$ –50 mM  $\text{AcH}$ . The excitation wavelength was 530 nm and was probed at 560 nm.

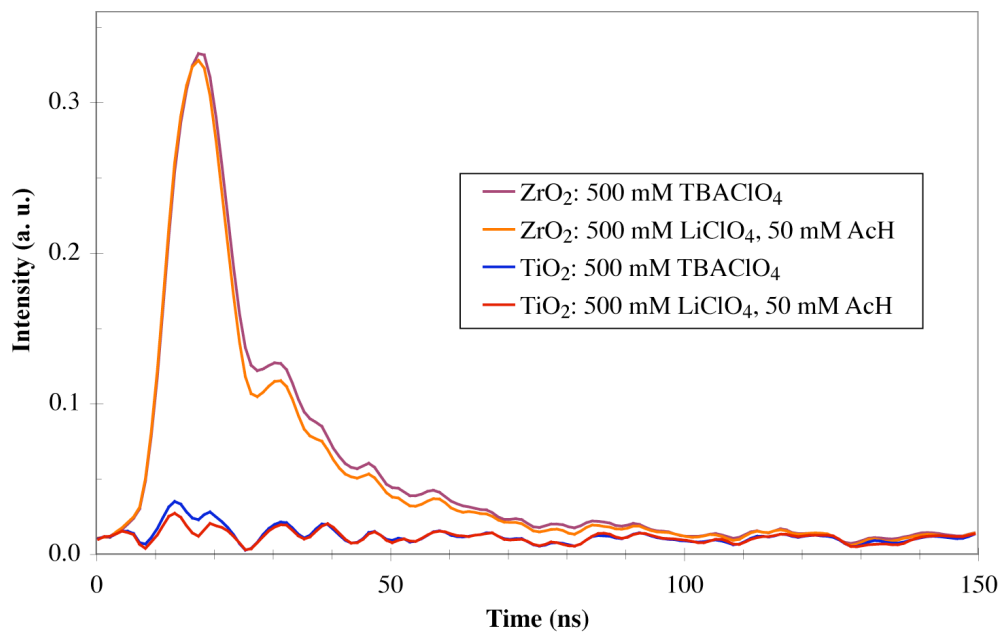


**Figure 4.12** Time-resolved emission of Ru(H<sub>2</sub>L')<sub>2</sub>(NCS)<sub>2</sub> bound to ZrO<sub>2</sub> vs TiO<sub>2</sub>, excited at 520 nm and monitored at 800 nm. Under no circumstances was significant emission observed from the chromophore when bound to TiO<sub>2</sub>, even at high excitation laser intensities.

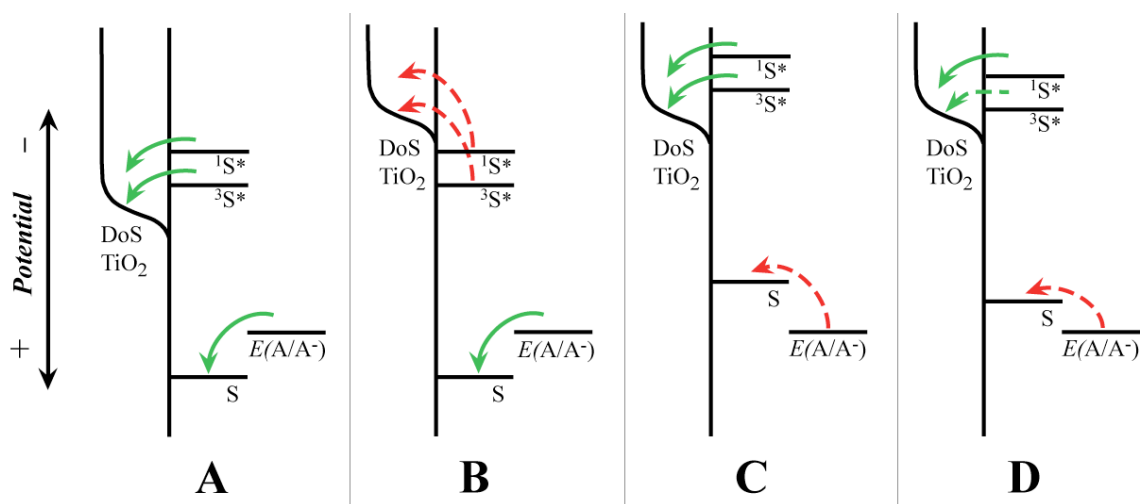


**Figure 4.13** Schematic diagram of the effect on the electron transfer rates to and from the sensitizer on TiO<sub>2</sub> under three circumstances, where DoS-TiO<sub>2</sub> indicates the density of states in the TiO<sub>2</sub>, S and <sup>1</sup>S\* and <sup>3</sup>S\* indicate the ground, singlet, and triplet excited states potential of the sensitizer, and  $E(A/A^-)$  is the Nernst potential of the redox mediator in solution. **Case A:** The potentials of the redox couple, the ground and excited state of the dye, and acceptor states in TiO<sub>2</sub> are all positioned so as to allow for efficient forward electron transfer. **Case B:** While the density of states in TiO<sub>2</sub> is shifted, the dye states have not been affected, and so while the reduction rate by electrolyte species is unchanged, the efficiency and rate of injection is greatly reduced, and the rate of recombination is increased (assuming the normal Marcus region). **Case C:** DoS-TiO<sub>2</sub> is shifted more negative, but the dye has been shifted an equivalent amount, resulting in

unchanged electron injection and recombination rates, but a greatly reduced regeneration reaction rate. **Case D:** Both Dos-TiO<sub>2</sub> and the potential of the dye have shifted, but not by the same amount. In this case, the injection efficiency from the <sup>3</sup>MLCT state might be reduced while the higher energy <sup>1</sup>MLCT state would still inject with high efficiency.

## REFERENCES

- (1) O'Regan, B.; Gratzel, M. *Nature* **1991**, *353*, 737.
- (2) Nazeeruddin, M. K.; Kay, A.; Rodicio, I.; Humphrybaker, R.; Muller, E.; Liska, P.; Vlachopoulos, N.; Gratzel, M. *J. Am. Chem. Soc.* **1993**, *115*, 6382.
- (3) Frank, A. J.; Kopidakis, N.; van de Lagemaat, J. *Coord. Chem. Rev.* **2004**, *248*, 1165.
- (4) Katoh, R.; Furube, A.; Barzykin, A. V.; Arakawa, H.; Tachiya, M. *Coord. Chem. Rev.* **2004**, *248*, 1195.
- (5) Gregg, B. A. *Coord. Chem. Rev.* **2004**, *248*, 1215.
- (6) Anderson, N. A.; Lian, T. *Coord. Chem. Rev.* **2004**, *248*, 1231.
- (7) Watson, D. F.; Meyer, G. J. *Coord. Chem. Rev.* **2004**, *248*, 1391.
- (8) Nelson, J.; Chandler, R. E. *Coord. Chem. Rev.* **2004**, *248*, 1181.
- (9) Durrant, J. R.; Haque, S. A.; Palomares, E. *Coord. Chem. Rev.* **2004**, *248*, 1247.
- (10) Argazzi, R.; Iha, N. Y. M.; Zabri, H.; Odobel, F.; Bignozzi, C. A. *Coord. Chem. Rev.* **2004**, *248*, 1299.
- (11) Gratzel, M. *Nature* **2001**, *414*, 338.
- (12) Gratzel, M. *Inorg. Chem.* **2005**, *44*, 6841.
- (13) Watson, D. F.; Meyer, G. J. *Annu. Rev. Phys. Chem.* **2005**, *56*, 119.
- (14) Hagfeldt, A.; Gratzel, M. *Accounts Chem. Res.* **2000**, *33*, 269.
- (15) Pelet, S.; Moser, J. E.; Gratzel, M. *J. Phys. Chem. B* **2000**, *104*, 1791.
- (16) Katz, J. E.; Brunshwig, B. S.; Lewis, N. S. (*submitted for publication*), **2007**.

- (17) Katz, J. E.; Smeigh, A. L.; McCusker, J. K.; Brunschwig, B. S.; Lewis, N. S. (*submitted for publication*), **2007**.
- (18) Bonhote, P.; Gogniat, E.; Tingry, S.; Barbe, C.; Vlachopoulos, N.; Lenzmann, F.; Comte, P.; Gratzel, M. *J. Phys. Chem. B* **1998**, *102*, 1498.
- (19) Juban, E. A.; McCusker, J. K. *J. Am. Chem. Soc.* **2005**, *127*, 6857.
- (20) Kuciauskas, D.; Freund, M. S.; Gray, H. B.; Winkler, J. R.; Lewis, N. S. *J. Phys. Chem. B* **2001**, *105*, 392.
- (21) Nazeeruddin, M. K.; Zakeeruddin, S. M.; Humphry-Baker, R.; Jirousek, M.; Liska, P.; Vlachopoulos, N.; Shklover, V.; Fischer, C. H.; Gratzel, M. *Inorg. Chem.* **1999**, *38*, 6298.
- (22) Kallioinen, J.; Benko, G.; Sundstrom, V.; Korppi-Tommola, J. E. I.; Yartsev, A. P. *J. Phys. Chem. B* **2002**, *106*, 4396.
- (23) Benko, G.; Kallioinen, J.; Korppi-Tommola, J. E. I.; Yartsev, A. P.; Sundstrom, V. *J. Am. Chem. Soc.* **2002**, *124*, 489.
- (24) Das, S.; Kamat, P. V. *J. Phys. Chem. B* **1998**, *102*, 8954.
- (25) Harris, L. A.; Wilson, R. H. *Annu. Rev. Mater. Sci.* **1978**, *8*, 99.
- (26) Kuciauskas, D.; Monat, J. E.; Villahermosa, R.; Gray, H. B.; Lewis, N. S.; McCusker, J. K. *J. Phys. Chem. B* **2002**, *106*, 9347.
- (27) Asbury, J. B.; Anderson, N. A.; Hao, E. C.; Ai, X.; Lian, T. Q. *J. Phys. Chem. B* **2003**, *107*, 7376.
- (28) Asbury, J. B.; Ellingson, R. J.; Ghosh, H. N.; Ferrere, S.; Nozik, A. J.; Lian, T. Q. *J. Phys. Chem. B* **1999**, *103*, 3110.

- (29) Benko, G.; Kallioinen, J.; Myllyperkio, P.; Trif, F.; Korppi-Tommola, J. E. I.; Yartsev, A. P.; Sundstrom, V. *J. Phys. Chem. B* **2004**, *108*, 2862.
- (30) Kallioinen, J.; Benko, G.; Myllyperkio, P.; Khriachtchev, L.; Skarman, B.; Wallenberg, R.; Tuomikoski, M.; Korppi-Tommola, J.; Sundstrom, V.; Yartsev, A. P. *J. Phys. Chem. B* **2004**, *108*, 6365.
- (31) Hannappel, T.; Burfeindt, B.; Storck, W.; Willig, F. *J. Phys. Chem. B* **1997**, *101*, 6799.
- (32) Yan, S. G.; Hupp, J. T. *J. Phys. Chem.* **1996**, *100*, 6867.
- (33) Yan, S. G.; Hupp, J. T. *J. Phys. Chem. B* **1997**, *101*, 1493.
- (34) Zaban, A.; Ferrere, S.; Gregg, B. A. *J. Phys. Chem. B* **1998**, *102*, 452.
- (35) Zaban, A.; Ferrere, S.; Sprague, J.; Gregg, B. A. *J. Phys. Chem. B* **1997**, *101*, 55.
- (36) Heimer, T. A.; Heilweil, E. J.; Bignozzi, C. A.; Meyer, G. J. *J. Phys. Chem. A* **2000**, *104*, 4256.
- (37) Enright, B.; Redmond, G.; Fitzmaurice, D. *J. Phys. Chem.* **1994**, *98*, 6195.
- (38) Nelson, B. P.; Candal, R.; Corn, R. M.; Anderson, M. A. *Langmuir* **2000**, *16*, 6094.
- (39) Hall, D. W.; Russell, C. D. *J. Am. Chem. Soc.* **1967**, *89*, 2316.
- (40) Gregg, B. A.; Pichot, F.; Ferrere, S.; Fields, C. L. *J. Phys. Chem. B* **2001**, *105*, 1422.

## CHAPTER 5

### *Combinatorial Synthesis of Mixed-Metal Oxides and High-Throughput Screening of Photovoltage for Water Splitting under Visible Light Illumination*

#### 5.1. INTRODUCTION

##### 5.1.1 The Challenge of Clean, Cheap, and Abundant Chemical Fuels

The 1972 landmark publication by Fujishima and Honda<sup>1</sup> first brought widespread attention to the possibility of using sunlight to produce hydrogen gas from water as an energy source. Today, the threat of global warming has renewed interest in finding viable alternatives to carbon dioxide-emitting fossil fuels.<sup>2-4</sup> Although many schemes have been suggested for providing the necessary scale of carbon-free energy, the use of sunlight to produce a chemical fuel, such as hydrogen gas, is ideal. While the world currently consumes some  $4.5 \times 10^{20}$  J per year,<sup>5</sup> equivalent to an average burn rate of 14.5 TW, the 120,000 TW of solar power that strikes the surface of the earth dwarfs this by nearly four orders of magnitude. While current photovoltaic solid-state devices can already generate electricity with overall conversion efficiencies approaching 50%,<sup>6</sup> such highly efficient solar cells remain extremely expensive to manufacture. Furthermore, electricity is not an optimal form of energy because of significant losses

incurred in storage and distribution. Splitting water with sunlight uses two abundant and renewable resources and produces a chemical fuel that can be stored efficiently. The only waste product of burning H<sub>2</sub> (or using it in a fuel cell) is water, and so by generating H<sub>2</sub> from only water and sunlight, the fuel cycle is a closed loop. Solving the problem of how to split water with sunlight cheaply and efficiently would be a tremendous breakthrough as a viable solution to what has been called “the most important scientific and technical challenge facing humanity in the 21<sup>st</sup> century.”<sup>4</sup>

### **5.1.2 The Four Requirements for Photoelectrosynthetic Solar Cells**

There are four fundamental requirements for any system to convert and store solar energy using a semiconducting material.<sup>7</sup> First, sunlight must be efficiently absorbed to produce electronically excited states in the photoactive material. Secondly, the photoexcited electron and the accompanying electron vacancy or hole must be separated in space to prevent their recombination, which produces heat and wastes energy. Third, the photoexcited charge carriers must be energetically and kinetically able to perform the desired chemical reaction (the splitting of water requires at minimum 1.23 V). Fourth, these charge carriers must not undergo deleterious side-reactions that chemically transform or otherwise degrade the semiconductor.

Finally, in addition to these four essential technical requirements, any viable candidate as an energy source on a global scale must be economically competitive with the cheapest and most abundant known fuel: coal. Current economic policies worldwide are simply incompatible with a renewable energy technology contributing a large majority of energy worldwide if the price is not competitive with the abundant fossil fuels that are already readily available. Due to the scale of the energy production globally, this

economic constraint also effectively demands that any raw materials used in the photoelectrochemical cell be extremely abundant, as even the most efficient systems will require vast stocks of raw materials (as an example, to generate 10 TW of power with a 10% efficient Si-based solar cell would require nearly 5 million metric tons of pure crystalline silicon).

### 5.1.3 Past and Current Research

While finding materials that meet some combination of three of the four technical requirements has already been demonstrated, no known system satisfies all four.<sup>8,9</sup> Several wide-band gap metal oxide semiconductors, such as  $\text{TiO}_2$ ,  $\text{SrTiO}_3$ , and  $\text{KTaO}_3$ , have been shown to split water efficiently and to be chemically stable.<sup>10-12</sup> However, these materials have band gaps of 3 eV or larger, and thus only absorb UV radiation, of which there is very little in terrestrial sunlight. This results in overall conversion efficiencies of only 1–2% at most. Other materials, such as CdTe or InP, have band-gaps that are better matched to the solar spectrum, but these semiconductors either corrode or become inert when used as photoelectrodes in aqueous solution.<sup>13</sup> Other materials are stable, have band gaps relatively well matched to the solar spectrum, but these do not produce photoexcited electrons with sufficient energy to reduce water to  $\text{H}_2$ .<sup>11</sup>

While no material has been found to date to efficiently split water using sunlight, there is no fundamental law of physics or chemistry that forbids it; it is therefore a question of finding the novel material that meets all of the requirements outlined above. One approach is to take a material that partially satisfies these critical requirements and modify it so as to fulfill the missing requirement(s). For instance, Zou et al. have demonstrated that the addition of Ni to  $\text{InTaO}_4$  changes the photoelectrochemical

properties so as to be able to split water at wavelengths of light as long as 420 nm (although overall conversion efficiencies in sunlight remain below 1%).<sup>14</sup> Similarly, many researchers have tried to use chemical methods to chemically passivate the semiconductor so as to prevent corrosion or degradation.<sup>15,16</sup> Others have instead opted for a combinatorial approach to synthesize vast numbers new materials and characterize their photoelectrochemical properties using a fast, high-throughput process.<sup>17,18</sup>

We present herein a new high-throughput synthesis and screening methodology for testing the photoelectrochemical properties of novel semiconducting compounds. A commercial inkjet printer is used to quantitatively combine up to eight different metal solutions at once, which are then pyrolyzed to form mixed-metal oxides. The photoelectrochemical properties were determined by measuring the photocurrent as well as the photovoltage. Measuring the open-circuit voltage under high-intensity illumination provides a measurement of the majority carrier quasi-Fermi level under illumination, whose energy is critical to driving a fuel-forming reaction in a photoelectrochemical cell. This new method of measuring photovoltages provides several key advantages over measuring the photocurrent.

## **5.2. EXPERIMENTAL**

### **5.2.1. Materials**

Fluorine-doped tin oxide coated glass (FTO) (Hartford Glass, TEC 15) was used as a substrate for the mixed metal oxides. Prior to deposition of metal solutions, FTO slides were washed thoroughly with soap and water, rinsed with distilled water and isopropanol, dried with  $N_2(g)$ . Samples were then treated with SurfaSil Siliconizing

Solution (Pierce) to make them hydrophobic, then rinsed sequentially with isopropanol, water, and again with isopropanol, before being dried with  $N_2(g)$ . Metal nitrates,  $Al(NO_3)_3$ ,  $Cu(NO_3)_2$ ,  $Co(NO_3)_2$ ,  $Ni(NO_3)_2$ ,  $Sr(NO_3)_2$ ,  $Cr(NO_3)_3$ ,  $Fe(NO_3)_3$ , and  $Zn(NO_3)_2$  (all from Aldrich and  $\geq 98\%$ ), and titanium(IV) bis(ethyl aceto-acetato)diisopropoxide (Tyzor LA, Aldrich), a water-stable titanium complex, were used as received. The metal solutions for inkjet printing (0.5 M in metal ion) were made using base stock ink solution from MIS Associates. To improve solubility, the base stock was first acidified with glacial acetic acid (Aldrich,  $> 99.99\%$ ) to pH 4.5 for metal nitrate solutions and to pH 7.0 for Tyzor solutions. Electrolyte solutions for photoelectrochemical characterization consisted of 1.0 M KOH in  $> 18.1 M\Omega\text{ cm H}_2\text{O}$ .

### **5.5.2. Combinatorial Metal Oxide Synthesis**

A refurbished Epson Stylus Photo R800 piezoelectric inkjet printer (Epson.com) was used to deposit mixed-metal nitrate solutions directly onto the FTO substrate. Empty, spongeless ink cartridges (MIS Associates) were each filled with a metal solution and used in place of the standard ink cartridges. A high-density polyethylene (HDPE) template 2.3 mm thick (Small Parts, Inc.) was constructed to allow the glass sides to be fed into the front of the printer using the CD-printing functionality. The printer aligned itself along the front edge of the HDPE template to provide nearly identical positioning on the glass each printing cycle.

To obtain quantitative control of the relative proportion of the printed metal solutions, the QuadTone Raster Image Processor software (QTR) ([www.quadtonerip.com](http://www.quadtonerip.com)) was used. QTR allows for user-defined control of how much ink from each cartridge is deposited. A grayscale tagged image file format (TIFF) image,

with of the maximum of 256 distinct grayscale colors was printed (see Figure 5.1). Using the QTR software, another file (a so-called “.quad” file) was used to define each grayscale color as a specific volume of metal solution to be printed from each printer cartridge. The same TIFF image was printed for each slide, but each time using a different .quad file in QTR, resulting in a different mapping of the grayscale color to printed composition. In this way, a unique set of mixed-metal oxides was printed on each FTO slide.

After being printed, metal solutions were dried at 80 °C for ~ 30 min, before heated under flowing air at 500 °C for 3 h, and then cooled to room temperature over the course of 8 h.

### **5.2.3. Characterization of Printed Metal Oxides**

In order to ensure quantitative mixing of the aqueous metal solutions, the composition of mixed-metal oxide samples was characterized by energy dispersive spectroscopy (EDS) (LEO 1550VP SEM with Oxford INCA 300 spectrometer).

### **5.2.4. Photoelectrochemical Measurements**

Two measurement methods were used to determine the photoelectrochemical properties of the mixed-metal oxide materials synthesized: first, a photocurrent-only setup was developed, followed by a system that allowed for complete electrochemical characterization of each material. In both cases, photoelectrochemical measurements were performed under illumination, using a 150 W Xe arc lamp, and in the dark. The FTO substrate was submerged in a 1 M KOH solution (except for 1–2 cm at the top where electrical contact was made) and illuminated through a quartz plate (GM Associates). All measurements were made using LabView software via a National

Instruments BNC-2100 connector block and PCI-6034E data acquisition card. Illumination intensity was measured with a Newport 815 power meter.

#### 5.2.4.1. *Photocurrent Measurements*

To measure photocurrents, 252 metal oxide spots were printed on a 76 x 102 mm FTO slide, where each material was in electrical contact with the others through the continuous conductive FTO film. A typical printed slide of mixed metal oxides is shown in Figure 5.2. The measurement set-up is shown in Figure 5.3. A single electrical lead made contact to all metals oxides on the FTO slide. The output of the arc lamp was focused using quartz optics to a spot  $\sim 3\text{--}4$  mm in diameter and chopped at  $\sim 13$  Hz (CH-61, Boston Electronics). The photoelectrochemical cell was translated in the X-Z directions using a computer-controlled translation stage (UniSlide translation stage, Velmex, Inc; MD-2 stepper-motor driver, Arrick Robotics; MD-2 LabView driver, TEM Consulting, LP). Moving the entire electrochemical cell relative to the stationary illumination beam allowed each metal oxide spot on the slide to be uniquely illuminated in sequence. At each position of the translation stage, the photocurrent was measured, in a two-electrode configuration, with Pt gauze as a counter-electrode, using a lock-in amplifier (model 124A, EG&G) equipped with a current-sensitive preamplifier (model 184, EG&G). A quartz slide split off  $\sim 10\%$  of the arc lamp beam, and was monitored with a silicon photodiode to ascertain the stability of the illumination intensity.

#### 5.2.4.2. *Photovoltage Measurements*

For photovoltage measurements, it was necessary to electronically isolate each metal oxide material from the others and to passivate the FTO back contact area to attain reproducible measurements. FTO slides were laser etched ( $50\ \mu\text{m}$  laser spot size,

Laserod, Inc.) to generate 260 electronically isolated conductive pads (4 mm by 3.8–5 mm) on each 77 x 152 mm FTO slide, with 130 contacts along each of the two 155-mm edges of the slide (see Figure 5.2 and Figure 5.4b). To electronically passivate the FTO substrate not covered by printed metal oxides, an insulating epoxy (1 part ADE678 and 5 parts ADE26, Nazdar) was screen-printed (using a AMI Inc, model HC-53 screen printer, with a 255-40 mesh polyester screen and 12.7  $\mu\text{m}$  of MX emulsion (Sefar Printing) over all exposed FTO, resulting in an effective back-contact surface area approximately equal to the size of the printed metal oxide spot, as shown in Figure 5.4e. The epoxy was cured for  $\sim 30$  min at 80  $^{\circ}\text{C}$ , and left for 3–7 days before using to fully cure. Contact to each of the 1.0 mm center-to-center FTO contacts along the edge of the glass substrate was made with an elastomeric connector (Silver Zebra Series 5002 Solid Support, FujiPoly). The elastomeric connector was clamped between the substrate and a custom-designed printed circuit board (PCB) (Advanced Circuits), which had 134 1.0 mm center-to-center contact pads along one edge. The elastomeric connector was clamped firmly in place between the FTO and PCB using two extended-reach clamps (McMaster Carr), with a 12.5-mm-thick Al plate supporting the PCB for evenly applied pressure across the elastomer (Figure 5.4f). Each contact pad of the clamped PCB (PCB-1) was connected to one wire of one of four 34-wire ribbon cables, which were connected to a second PCB (PCB-2) (see Figure 5.5). On PCB-2, each wire was routed to make connection to the four 50-pin D-subminiature connectors of a National Instruments LHF200 switch cable, which was subsequently connected to a 196-channel multiplexer (SCXI-1175, National Instruments). Also, seven outputs were connected directly to terminals on PCB-2: one was the output terminal of the multiplexer, and the other six were the last three contacts on each side of

PCB-1, which were used as test contact to ensure proper alignment of the etched FTO contacts and the PCB-1 contact pads (discussed below). The photovoltage obtained from each spot was measured (by the data acquisition card) vs a saturated calomel reference electrode (SCE). To determine the effect of illumination relative to the equilibrium voltage in the dark, the light beam was manually blocked for  $\sim 1$  s, and the rise or decay in photovoltage was subsequently monitored. A schematic of the experimental setup to measure photovoltages is shown in Figure 5.5

#### 5.2.4.3. *Current-Density vs Potential Measurements*

Using a nearly identical setup as described for photovoltage measurements, current-density vs potential behavior was measured under potentiostatic control (SI 1287, Solartron) for mixed metal oxides combinatorially in a three-electrode setup. Platinum gauze was used as a counter electrode. Scan rates were 20 mV/s. Measurements were made both in the dark and under illumination.

## 5.3. RESULTS

### 5.3.1. Quantitative Mixing of Aqueous Metal Ion Solutions with an Inkjet Printer

#### 5.3.1.1. *Inkjet Printing*

The commercially available Epson R800 inkjet printer was used to print quantitative mixtures of aqueous metal solution on glass substrates with minimal modifications to the printer itself. Rather than installing the ink cartridges provided with the printer, empty replacement cartridges were filled with an aqueous solution of various metals. A built-in printer functionality (designed to allow printing on CDs and DVDs) was used to print on rigid glass substrates. A simple HDPE template replaced the CD

tray, which allows a CD to be fed into the printer. The template consisted of a rectangular sheet of HDPE (210 x 300 mm) with a hole cut out of the center corresponding to the size of the FTO substrate. The FTO slide was kept in place in the template by simply taping a piece of a sheet of transparency paper (for an overhead projector) across the hole on the underside of the template. Because of the way by which the printer senses the position of the template when it is loaded, it was possible to easily print on the FTO substrate with very high spatial resolution and reproducibility ( $\pm 0.5$  mm).

In order to print mixtures with pre-determined compositions, it was necessary to use an alternative driver other than the standard Epson-provided driver for the R800 printer. The software used, QTR, is commercially available and allows the user to create a complete color-managed system for black and white printing. To print using QTR, a single TIFF image was generated using Matlab, consisting of 256 different gray-scale colors (see Figure 5.1). In a separate so-called “.quad file,” each color is uniquely defined in terms of a specific amount of solution to be dispensed from each of the eight printer cartridges. For each selection of 255 unique mixed-metal oxides to be printed on a given substrate, the same TIFF image is printed but a different quad file is selected for each (the 256<sup>th</sup> grayscale color is reserved for the area surround the spots, and thus always defined as printing nothing). A Matlab code was written to automatically generate a set of quad files so as to print every single possible combination of eight unique metals, in steps of 10% (molar). Upon changing one or more of the metals loaded in the printer, a new series of .quad files is subsequently generated, using a history of

previously printed materials to only generate mixtures that had not yet been printed, so as to avoid any repetition.

#### *5.3.1.2. Determination of Metal Oxide Composition*

The composition of printed spots was confirmed by EDS after pyrolyzing the aqueous metal solutions at 500 °C. A set of ~ 100 binary mixtures was tested, and the concentration of each metal in each mixture was determined by the EDS INCA software, which calculates atomic percent compositions based on the acquired spectrum. Typical results from the compositional analysis of a single spot are shown in Figure 5.6 and Table 5.1. Elements present in the substrate were in all cases present in the EDS spectra, including oxygen, silicon, tin, and calcium. Only the elements specified in the .quad file to be printed on a given spot were ever observed (although the automatic elemental analysis by the INCA software was not always correct in that certain elements were commonly misidentified, in particular W and Re).

For binary combinations of metals, the EDS measurement of atomic percent matched the expected percentage within 5–10 percentage points (as much as 15, but within 10 percentage points the large majority of the time). A sampling of expected compositions and the values as measured by EDS are shown in Table 5.1 for a variety of binary metal oxides.

### **5.3.2. Photoelectrochemical Characterization**

#### *5.3.2.1. Photocurrent Measurements*

In the dark, a significant (and varying) amount of current was measured at short-circuit between the metal oxide spots and/or the FTO substrate and the counter-electrode. In order to distinguish this DC background current from the photocurrent, the light source

was chopped, allowing the AC effect of the light to be distinguished. The polarity of the current was indicative of whether the material exhibited photocathodic or photoanodic behavior. The photocurrent was measured for each spot for  $\sim 5$  seconds, and due to the sometimes slow rise- and decay-time of the photocurrent, measurement of a specific spot was repeated until a stable value was obtained. Figure 5.7 shows a false-color image of photocurrent as a function of location on the FTO substrate.

Initial measurements revealed a number of metal oxides that exhibited both anodic and cathodic photocurrents on the order of nA to several  $\mu\text{A}$  for a single printed spot (approximately  $4 \text{ mm}^2$ ). While most materials tested gave no photoresponse at all, several binary combinations gave particularly strong photocathodic currents, including Co and Zn (80% Co with 20% Zn and 70% Co and 30% Zn) and Co and Fe (90% Co and 10% Fe) and Al and Co (80% Co and 20% Al) (see Figure 5.7). Deoxygenation of the electrolyte solution by bubbling  $\text{N}_2(\text{g})$  resulted in significantly increased photocurrents for many materials. Additionally, for several materials the measured photocurrent changed over time. These changes included both increases and decreases in the magnitude of the photocurrent, and occurred both over a period of minutes to hours and also from day to day. The materials that gave these variable responses tended most often to give cathodic currents.

#### 5.3.2.2. *Photovoltage Measurements*

Initially, the photovoltage for mixed-metal oxides was measured in essentially the same way as for the photocurrent using selective illumination rather than electronic isolation, except the light source was not chopped. However, measured photovoltages for well-characterized materials, such as  $\text{TiO}_2$ , were approximately  $-0.15 \text{ V}$  vs SCE,

significantly more positive than expected (at pH 14, the flat-band potential of TiO<sub>2</sub> is -1.1 V vs SCE).<sup>8,10</sup> Not only were measured voltages significantly more positive than expected for photoanodes, photoactive materials took as long as 30 minutes to reach a stable open-circuit voltage after being illuminated. The decay back to the equilibrium voltage in the dark was even slower, thereby requiring eight or more hours to scan a single slide of 252 materials (as opposed to ~ 30 min when measuring photocurrents). The combination of etching the FTO substrate to electronically isolate spots and covering the FTO back contact area with epoxy solved both of these problems.

To electronically contact 130 individual spots on the etched in the FTO electrode, PCB-1 was designed with a high density of metallic contact pads along one edge (as shown in Figure 5.4f). To improve the conductivity of the connection, an elastomeric connector was used, resulting in negligible contact resistance between the FTO and PCB-1. Because of the small pitch of the contact pads, clamping the FTO glass to the contact pads of PCB-1 depended on precise alignment of PCB-1 with the FTO etch pattern (due to the fine pitch of the metallic component of the elastomer, it need not be placed in perfect register, forming numerous redundant conductive pathways for each PCB-1 pad). An X-Z micrometer stage was used to easily manipulate the position of the FTO glass relative to PCB-1 when clamping them together.

To ensure proper alignment was achieved each time (essential to proper correlation of material identity with photoresponse), a simple testing system was devised using a resistance measurement across four pairs of contacts. PCB-1 contained 134 contacts, four more than on the FTO slide (see Figure 5.4f). Thus on each end of PCB-1, two extra contact pads were included, and these contacted an un-etched area of the FTO

substrate. Thus, if the contacts were properly aligned, the last pair of contacts of each side of PCB-1 would be shorted via the FTO. Additionally, the adjacent contact pad to these (the third from the end) was separated from the last two by the first etch line on the FTO substrate. Therefore, this third-to-last and the penultimate contact pad should nominally be an open circuit. Thus the last three contacts on each side of PCB-1 are probed with a simple resistance measurement: if the contacts on each end are short-circuited and at open-circuit as expected, then each contact on the entire PCB must be properly aligned with the corresponding contact on the FTO slide. The six leads necessary for this measurement were connected from PCB-2 to a small switch box, and that to a voltage meter (see Figure 5.5).

Metal oxides printed on etched FTO substrates gave substantially faster response times, but still the measured photovoltages did not match expected values for test materials, in particular  $\text{TiO}_2$ . Covering the FTO substrate with epoxy had a large effect on the measured photovoltages (by as much as several hundred mV). For  $\text{TiO}_2$  at the same illumination intensity, the photovoltage changed from  $-0.807\text{ V}$  to  $-0.877\text{ V}$  vs SCE by simply coating the surrounding FTO substrate exposed to the electrolyte with epoxy. Under strong illumination, the measured photovoltage of  $\text{TiO}_2$  approached the flat-band potential of  $\text{TiO}_2$  at pH 14 ( $-0.88\text{ V}$  vs SCE compared to  $-1.1\text{ V}$  vs SCE).<sup>8,10</sup> Additionally, covering a significant percentage of the sample itself with transparent epoxy resulted in photovoltages of  $-1.1\text{ V}$  vs SCE for  $\text{TiO}_2$ . Within the limit of completely insulating the  $\text{TiO}_2$  spot, the greater the percent coverage of the spot by epoxy, the more negative the photovoltage.

To test the overall measurement methodology, a repeating pattern composed of five different materials was generated on a single FTO substrate (as shown in Figure 5.2). Each material was printed with five thicknesses (as controlled by changing the total volume of metal solution deposited by the printer), and each material was printed five times at each thickness value. Figure 5.8 shows the measured photovoltages from this slide, and indicated three important characteristics. First, some variation is observed in the measured voltage as a function of spot thickness. Second, spots with nominally identical compositions gave the similar photovoltages. Third, one of the materials showed photocathodic behavior, three photoanodic, and one had no photoresponse at all. This was determined by the shift in the open-circuit voltage in the light compared to the dark.

The potential of the printed metal oxides spots in the dark vs SCE varied by several hundred mV (variation as large as +0.2 V to -0.3 V vs SCE was observed), and this variation introduced ambiguity in the photovoltage measurements. Blocking the light beam briefly and measuring the voltage shift from light to dark was used to verify the effect of illumination. The sign and degree of the voltage difference measured in the dark and under illumination could thus differentiate samples. Thus after the measurement of the photovoltage for each material, the light beam was briefly blocked ( $< 1$  sec) and the change in voltage is monitored. Figure 5.9 shows the measured photovoltages as well as both the direction and relative magnitude of the light-induced photovoltage change using this method. This additional step in the screening process determines that the photovoltage is in fact different than in the light.

Figure 5.10 shows a logarithmic dependence of the photovoltage on illumination intensity for mixed metal oxides samples, including TiO<sub>2</sub>. The slope of a linear fit of the photovoltage vs the logarithm of the illumination power varied between the mixed-metal oxide samples tested (in mV per decade):  $-76 \pm 12$  mV for 100% Ti (TiO<sub>2</sub>) and  $60 \pm 11$  mV for 70% Co–30% Zn. Other materials, such as 10% Al–10% Co–10% Sr–70% Ti, 50% Sr–50% Ti, and 30% Sr–30% Zn–40% Ti, showed a clear trend in photovoltage and we not strongly photoactive.

### 5.3.2.3. *Current Density vs Potential Behavior*

It is also possible to measure the current density vs applied potential ( $J$ - $E$ ) behavior of individual printed spots in a combinatorial fashion due to the electronic isolation of each spot. Figure 10 shows  $J$ - $E$  curves for samples of printed TiO<sub>2</sub> both in the dark and under illumination. The photocurrent showed a significant dependence on the amount of ink printed for the TiO<sub>2</sub>, with a maximum photocurrent for samples with an ink level of 46% of the maximum allowed by the QTR software. The photovoltages measured by scanning  $J$ - $E$  measurements correspond closely to those measured at open-circuit. No significant effect was observed as a function of position of the spot in a given column despite the varying resistivity of the connecting FTO “wire” (which varied from  $\sim 200$  to  $\sim 1000 \Omega$ ) due to the varying distance of the spot from the elastomeric connector.

## 5.4. DISCUSSION

While combinatorial synthesis and screening of novel mixed-metal oxide materials has been demonstrated previously,<sup>17,18</sup> the new methodology described here has

several important advantages. The first key advantage is the larger number of metal oxides that can be combined simultaneously during a single printing. The second is the additional information gleaned from a photovoltage rather than photocurrent measurement. The third is the additional flexibility in the types of photoelectrochemical measurements that can be made combinatorially and with very high throughput.

#### **5.4.1. Inkjet Printing of Aqueous Metal Oxide Precursors**

One important advantage of using the deposition method described herein is the very low cost for the entire printing system, which required no significant modification to the commercially available system (only replacing the ink cartridges and using the QTR software). Using the QTR software, the printer provides accurate and reproducible deposition of solution volumes, allowing simultaneous control of both spot composition and the total amount of material printed. This also eliminates the need to re-print multiple times to increase spot thickness, which requires precise alignment of the substrate each time. Furthermore, the printer's eight ink cartridges allow a tremendous number of materials to be printed without changing the solutions in the printer and re-printing, greatly decreasing the time required to print a library of mixtures consisting of three or more metals (compared to a system which dispenses only one metal solution at a time). By this method, 255 complex combinations of up to eight metals can be printed all at once. That eight solutions can be loaded simultaneously into the printer also minimizes the chances of cross-contamination due to repeatedly printing different solutions through the same printer nozzles.

Rather than producing a relatively smooth gradient of compositions as did Woodhouse et al.,<sup>17</sup> a quantized step size of 10% was chosen. This step size balanced the

need to fully explore the eight-dimensional compositional space available and still limited the number of materials to synthesize to a reasonable level. In this configuration, 78 FTO slides, with 255 unique materials each, are required to prepare every possible combination (using a concentration step size of 10%) of the eight metal solutions that can be loaded into the printer simultaneously. If a promising material was found, the composition could be further optimized to maximize the photoactivity.

Printing isolated spots of mixed-metal oxides, rather than overlapping gradients,<sup>17</sup> also provided several critical advantages in the measurement system used here. For photocurrent measurements, the relatively large spot-to-spot distance meant that the spatial resolution of the illumination source was not critical to the measurement, allowing the use of the focused beam of an arc lamp to provide intense white light excitation, rather than a CW laser for example. Use of white light from an arc lamp is extremely versatile: its broad spectrum has significant intensity from 200 nm to 2500 nm. The use of series of long-pass (or band-pass) optical filters in the beam path provides a simple low-cost method for ascertaining the wavelength dependence of the photoresponse of the metal oxides. From the onset wavelength of the photoresponse of the material, the approximate energy of the band gap can be determined.

#### **5.4.2. Photocurrent Measurements**

The ability to generate photocurrent with a high external quantum yield, or the fraction of electrons collected per incident photon, is an essential property of any efficient solar cell. However, as a criterion upon which to base a search for materials that can split water with visible light, the value of the photocurrent contains limited information. When screening novel materials, what does it mean if no photocurrent is observed? What

does it mean if photocurrent is observed? There are mechanisms by which photocurrent can be generated but not by the desired water-splitting reaction, and there are reasons that an otherwise nearly ideal material would not produce a significant photocurrent.

In a combinatorial screening system such as described here, a significant percentage of false positives are time consuming and inconvenient, in that they prompt more detailed investigation of a material that is ultimately unsatisfactory. A false positive could arise due to photocurrent flow from a reaction other than evolution of  $H_2$  and  $O_2$  from water. For instance, light-driven corrosion or dissolution would likely result in observable photocurrent through the external circuit, although such a material would plainly fail the requirement of photostability outlined above. One way to avoid this issue would be to illuminate all materials for an extended period before screening, such that any photo-driven side reactions would go to completion before screening that material. However, since each material passed a different amount of current, the time needed to stoichiometrically drive a corrosion or dissolution reaction to completion could vary by orders of magnitude for different materials, and could take up to several weeks of constant exposure! While not inconceivable, adding such a long pre-exposure step would greatly reduce the throughput rate of the screening step, not to mention the difficulties with illuminating a large number of samples simultaneously with high-intensity UV-containing light for an extended period of time. Several FTO slides with a variety of mixed metal oxides were exposed to sunlight while immersed in a solution of KOH and after the course of several weeks, the coloration of some spots was noticeably altered, indicating the composition of the material had changed.

Significant variations in photocurrent were observed for a number of materials over the course of the 5–20 second measurement (due to the changing photocurrents, measurements were repeated until the value stabilized, leading to longer measurement times per spot). These changes observed were most often decreases in photocurrent, although surprisingly the photocurrent of some spots increased over time. The changing photocurrents were attributed to photoelectrochemical degradation or selective dissolution, thereby changing the composition of the mixed metal oxide. While not proven, this is the most likely explanation for the observation of both increasing and decreasing photocurrents over time. It was not possible to reliably determine to what extent a specific material had decomposed, dissolved, or changed composition. The photocurrents passed were low enough that it would take a matter of weeks under constant high intensity illumination to completely consume the material. In any case, there was no evidence to suggest that the variation was due to instrumental fluctuations, and such large variation in photocurrent is indicative that the photocurrent is not due to catalytic evolution of H<sub>2</sub> and O<sub>2</sub> from water. Many materials, perhaps as large as ~ 20% of all materials tested, gave false positives by the photocurrent screening method. In fact, the large majority of the photocurrents shown in Figure 5.7 were ultimately deemed to be due to deleterious current-producing side reactions rather than water splitting based on the unstable magnitude of the measured photocurrent for these samples. However, conclusively determining the origin photocurrent is far too time-consuming to be compatible with the high-throughput combinatorial approach taken here.

In contrast to the relatively minor inconvenience of false positives, any false negatives are unacceptable. It is critical therefore that a good screening system must give

reliably accurate measurements so that materials are not passed over due to instrumental malfunctions. In addition to this, in an ideal screening methodology, materials that are “near misses” should also be noted. If a material was synthesized that satisfied (or very nearly did) the four requirements outlined above, but gave a poor photoresponse when measured, it would be discarded and never re-investigated. Also, if a material had a low photocurrent, no information would be learned about which requirement it failed to meet, or how close it was to meeting that particular requirement. Did the material fail to absorb a significant amount of light due a combination of a thin printed sample and a relatively low absorption coefficient? Did the material absorb light and produce electrons and holes at the required energy but electron transfer kinetics at the interface were very slow? Or perhaps the material was ideal in all ways except that the conduction band was just very slightly below the hydrogen potential or the valence band above the oxygen potential. Measurements of the photocurrent provide no information about this, meaning that nearly ideal materials would be passed over.

While the methodology is combinatorial in nature, it is clear that the materials chosen to be screened should be based on some knowledge, either theoretical or empirical, of what combinations are most promising. There are simply too many elements to choose from and too many combinations possible, no matter how fast, cheap, or simple the synthesis or screening method. It is therefore essential to not only screen for functioning materials, but to also learn something from those that do not work—especially considering the odds that most materials screened will not meet all four requirements simultaneously! Therefore a new methodology was developed to measure photovoltages combinatorially, which to our knowledge has not been reported previously.

### 5.4.3. Photovoltage Measurements

Compared to a photocurrent measurement, the photovoltage provides more than just a yes-or-no answer regarding its photocatalytic activity. The measured photovoltage measures the quasi-Fermi level of the material under illumination. The measurement does not depend on actually driving any reaction as it is an open-circuit measurement, and so any effects due to the kinetics of the water-splitting reaction can be neglected. Also, deleterious side reactions would not lead to false positives as such reactions, while generating photocurrent, certainly would not result, in and of themselves, in generation of photovoltage. Another advantage is that, because the measurement does not require individual spot-by-spot illumination, the photovoltage measurements can be performed significantly faster.

The most important advantage of measuring the photovoltage is that it reveals the quasi-Fermi level of the material under illumination. It is this value that must be more negative than the  $\text{H}_2/\text{H}_2\text{O}$  potential for a photoanode, or for a photocathode more positive than the  $\text{O}_2/\text{OH}^-$  potential. As such, it reveals not only if a material is thermodynamically capable of splitting water, but if not, how close it is. Thus even if the material is not capable of splitting water as is, meaningful information is still ascertained from a photovoltage measurement. For instance, if the material has band edges with sufficient energy to drive both half-reactions, but a catalyst is necessary for the reaction to occur at an appreciable rate, the material should still be considered noteworthy. Also, if, for instance, a photoanodic material had a conduction band edge energy just slightly lower than  $\text{H}_2/\text{H}_2\text{O}$  potential, that the material very nearly satisfied this requirement would be

noted; further fine-tuning of the material's composition could lead to a sufficient band edge position.

Photovoltage measurements also allow one to search for a complementary pair of photoanodes and photocathodes for water splitting. Rather than finding a single material to satisfy all four requirements outlined above, two light-absorbing materials could be used in conjunction. This changes two of the essential requirements: in two-material case the sum of the band-gaps of the materials must be 1.23 V, and the conduction band edge of the photoanode of the photoanode must be more negative than the  $\text{H}_2/\text{H}_2\text{O}$  potential while the valence band of the photocathode must be more positive than the  $\text{O}_2/\text{OH}^-$  potential. By using two separate materials, the restrictions on viable materials are notably relaxed. Monitoring only photocurrent, it is not possible to search individually for two materials that could drive each half-reaction when used in conjunction as neither material would be capable of splitting water when used with a metallic counter-electrode.

Because of the novelty of the photovoltage measurement system and the critical importance of avoiding false negatives when implementing it to screen full-scale for new materials, a number of proof-of-concept experiments were performed to test the system, using both an assortment of mixed metal oxides as well as the well-characterized photoanode,  $\text{TiO}_2$ . With this in mind, the dependence of the photovoltage on the light intensity was measured.

Using a kinetic model of interfacial electron transfer under illumination, the quasi-Fermi level of the material is expected to vary logarithmically with illumination intensity (by 59 mV per decade),<sup>12</sup> as was observed (see Figure 5.10). The observation

that the measured photovoltages follow a logarithmic dependence for each of the photoactive materials tested, and with slopes approximately equal to the theoretically predicted value of 59 mV per decade, is strong evidence that the measured photovoltage is indeed determined by the quasi-Fermi level under illumination. Additionally, the sign of the slope indicates that  $\text{TiO}_2$  is a photoanode (as expected), whereas the mixture of Co/Zn is photocathodic.

This means that while it is important to compare photovoltages at constant illumination for all samples, the logarithmic dependence ensures that the photovoltage varies by less than 100 mV per order of magnitude change in intensity.<sup>12</sup> Variations in illumination intensity from spot to spot of more than a factor of two are very unlikely, given the experimental setup (although the intensity of the arc lamp output is not homogenous across the area of the FTO slide). Furthermore, any photoanode that is within even 100–300 mV of the  $\text{H}_2/\text{H}_2\text{O}$  potential would prompt further investigation. Preliminary screening of some 250 mixed metal oxides revealed no materials with photovoltages within 0.5 V of the  $\text{H}_2/\text{H}_2\text{O}$  potential (except for  $\text{TiO}_2$ ), and so choosing a relatively low threshold photovoltage for screening materials may in fact be sufficiently selective. Without having already scanned a few thousand materials, it remains unclear how thresholds should be established for what is to be further investigated. Will 10% of materials give noteworthy photovoltages? Or will it only be more like 1%, or even 0.01%? Only after the photovoltage of a relatively large number of samples (e.g., a complete library of combinations of 8 metals) has been measured will it be clear what an appropriate threshold will be for selecting materials for further detailed investigation.

If only the photovoltage is measured, whether the material is a photoanode or photocathode response, or even photoactive at all, can in fact be ambiguous due to the fact that there are two redox couples in solution with which the material can interact. That a material is photoactive or not is in fact not always trivial to determine from the photovoltage alone because of the varying potential of different spots in the dark due to an ill-defined solution potential. What if the photovoltage was in fact no different than the voltage measured in the dark? A photocathode with a photovoltage of +0.2 V vs SCE would be considered a very good photocathode in the screening process, but if the potential was arbitrarily at that value due to variations in the poorly defined solution potential and not due to a photoelectrochemical effect at all, the screening method would return a false positive.

For a large negative voltage (e.g.,  $V_{oc} < -1.1$  V vs SCE), one might safely assume that the material is a good photoanode and that quasi-Fermi level is negative of the  $H_2/H_2O$  potential. Similarly, a large positive voltage (e.g.,  $V_{oc} > 0.2$  V vs SCE) would indicate a good photocathode, with the quasi-Fermi level positive the  $O_2/OH^-$  potential. Intermediate voltages are harder to interpret without further information. A material with a  $V_{oc} = 0$  vs SCE might be selected as a reasonable candidate for further investigation if it was a photocathode. In contrast, an anode with such a positive voltage would be considered a very poor material. Or, it might be that the voltage in the dark happened to be equal to 0 vs SCE! For such an ambiguous case, it is therefore critical to quickly and easily distinguish these two possibilities.

As mentioned above, the sign of the slope photovoltage vs the logarithm of illumination intensity does determine whether the material is photoanodic or

photocathodic. However, making measurements for a full series of light intensities for each material is too time-consuming for a high-throughput approach. However, the sign of the slope is what is essential here, not the exact value of the slope itself, and so the simplest possible comparison of light intensities can be made quickly and easily: light vs dark.

Figure 5.9 shows that the change in photovoltage after blocking the illumination source (or going from dark to light) is indicative of the photoelectrochemical nature of the material. A photoanode will produce a more negative voltage under illumination than in the dark, whereas a photocathode will produce a more positive one. Thus, a determination can be made quickly for each material by briefly blocking the light source with a shutter and fitting any subsequent change in voltage as a linear function (as a simple characterization rather than physical model for the decay time profile). A positive slope indicates a photoanode, whereas a negative indicates a photocathode, and no change in voltage at all suggests a material that is not photoactive. This then allows us to measure the photovoltage of the material, but also to determine whether the material is a photoanode or photocathode.

## **5.5. CONCLUSIONS**

We have demonstrated that quantitative mixtures of aqueous solutions of metal ions can be deposited on conductive glass substrates using a commercially available inkjet printer. Metal solutions are then pyrolyzed to form mixed metal oxides. By this method, vast number of combinations of up to eight different metals can be formed very easily and at low cost. We have also developed and demonstrated a novel screening

method to search for materials capable of driving fuel-forming photoelectrochemical reactions. The proof-of-concept experiments presented here illustrate the increased speed, flexibility, and ease of use compared to previously reported systems. Most importantly, the new methodology, in which the photovoltage of the material is determined, provides critical additional information not available from photocurrent-only measurements. The approach is furthermore easily adaptable to a full array of photoelectrochemical characterization, such as current-voltage behavior, and even the spectral response, flat-band determination by capacitance measurements (Mott-Schottky analysis), and measurement carrier diffusion lengths.

## **5.6. ACKNOWLEDGMENTS**

We gratefully acknowledge Dr. Michael Woodhouse and Prof. Bruce Parkinson at Colorado State University, and Dr. Bruce Brunshwig for numerous valuable discussions. We acknowledge the Department of Energy, Office of Basic Energy Sciences for support of this work.

**Table 5.1** Representative values of the measured and expected atomic percents of binary mixed metal oxides as measured by EDS using the INCA software. The expected value is given by the ratio of the volume of metal ion solution specified in the .quad file using the QTR software.

Measured		Expected		Error
%Fe	%Co	%Fe	%Co	
0.58	0.42	0.70	0.30	12%
0.51	0.49	0.60	0.40	9%
0.41	0.59	0.50	0.50	9%
0.32	0.68	0.40	0.60	8%
0.24	0.76	0.30	0.70	6%
0.15	0.85	0.20	0.80	4%
0.06	0.94	0.10	0.90	4%
%Co	%Ni	%Co	%Ni	Error
0.88	0.12	0.90	0.10	
0.81	0.19	0.80	0.20	1%
0.35	0.65	0.40	0.60	5%
%Cu	%Sr	%Cu	%Sr	Error
0.31	0.69	0.40	0.60	
0.23	0.77	0.30	0.70	7%
%Cu	%Cr	%Cu	%Cr	Error
0.37	0.63	0.30	0.70	
0.47	0.53	0.40	0.60	7%
0.56	0.44	0.50	0.50	7%
%Co	%Cu	%Co	%Cu	Error
0.41	0.59	0.40	0.60	
0.49	0.51	0.50	0.50	1%

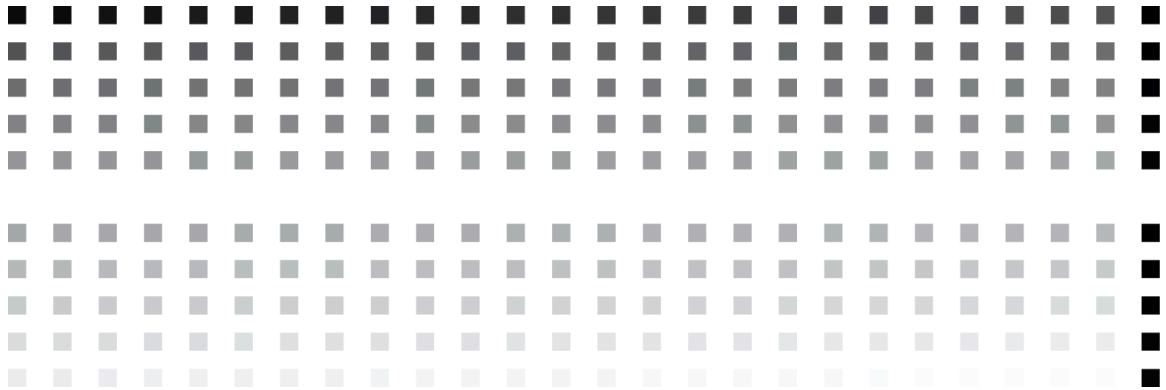
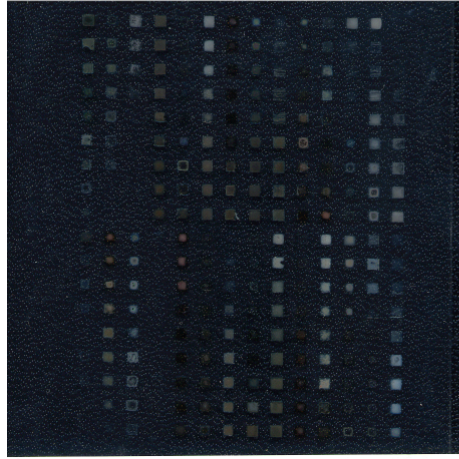
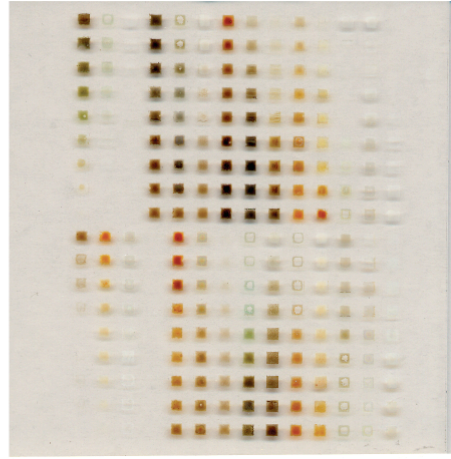


**Figure 5.1** The grayscale TIFF image printed using the QTR software to make quantitative mixture of 255 different mixed metal oxides on a single substrate. Rather than printing different images to generate different mixtures, the same TIFF file is used each time, but the QTR software uses a new .quad file to generate the varying compositions. The right-most column is composed of five controls—five well-characterized materials with known photovoltages for comparison.

**a)**



**b)**



**c)**

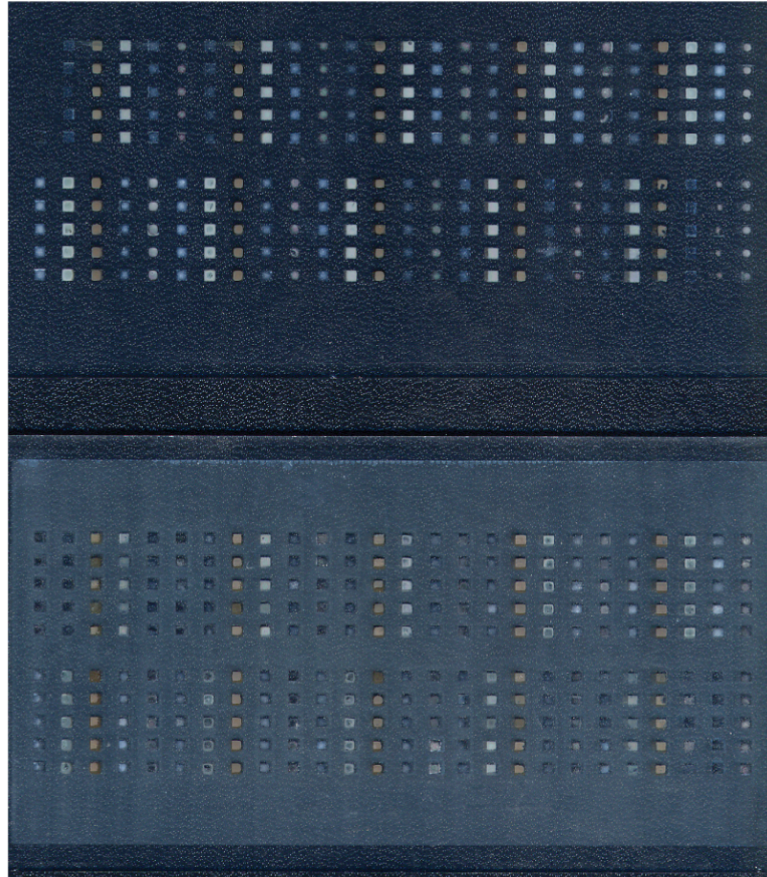


**Figure 5.2** Image of mixed metal oxide spots printed on an FTO substrate using an inkjet printer to make quantitative mixtures of aqueous metal solutions which are baked at 500 °C to form oxides. **(a)** and **(b)** Printed slides on a continuous FTO substrate, as used for the photocurrent measurement setup. Both (a) and (b) are of the same slide, with only a different background for improved contrast. **(c)** Image of the slide with a repeating pattern of five mixed metal oxides as described in the text. The upper image shows the slide after pyrolysis, and the bottom is shown after the FTO back-contact surface area was coated with epoxy.

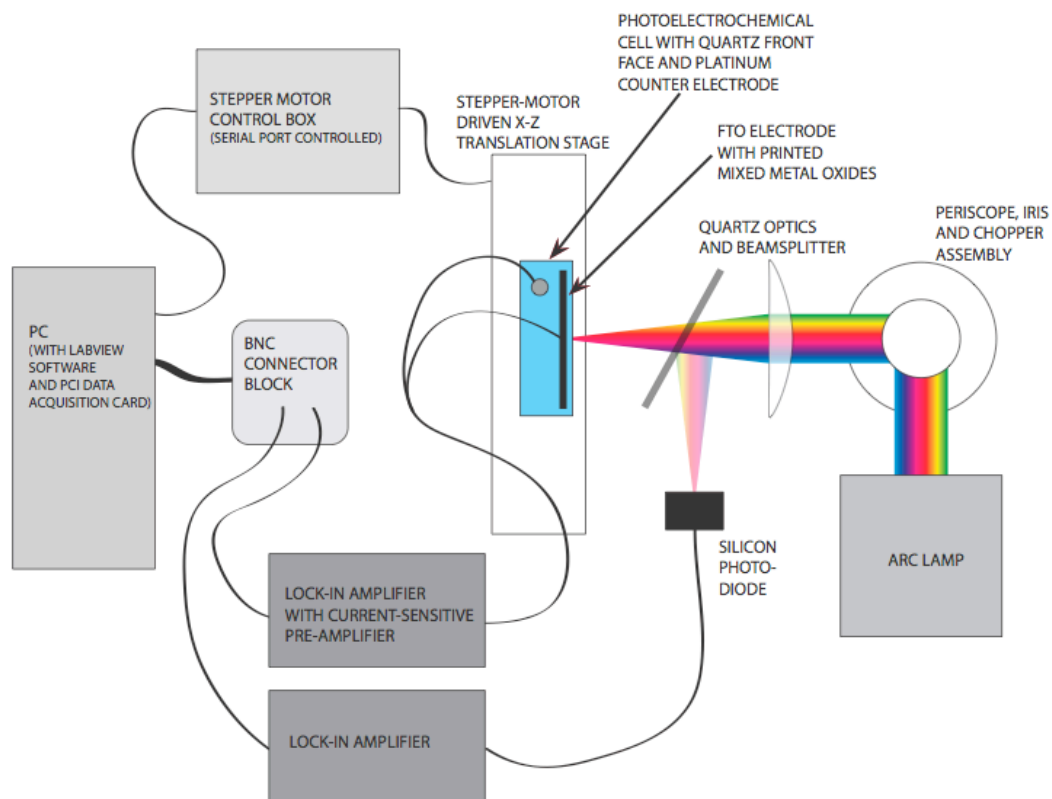


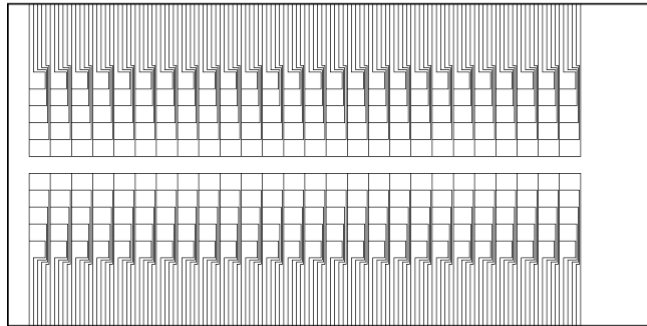
**Figure 5.3** Schematic of the setup for photocurrent measurements. A Xe arc lamp provides white light illumination, which is focused onto the substrate. A X-Z translation stage is used to move the entire electrochemical cell so as to illuminate each printed material on the slide in sequence. The photocurrent from the mixed metals oxides and from a reference Si diode are monitored using lock-in amplifiers and recorded on a PC.

a)



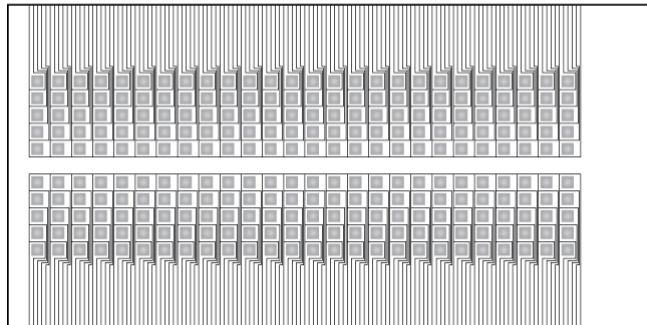
↓ STEP 1

b)



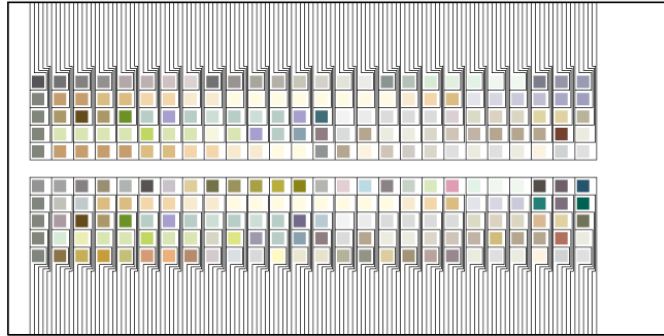
↓ STEP 2

c)



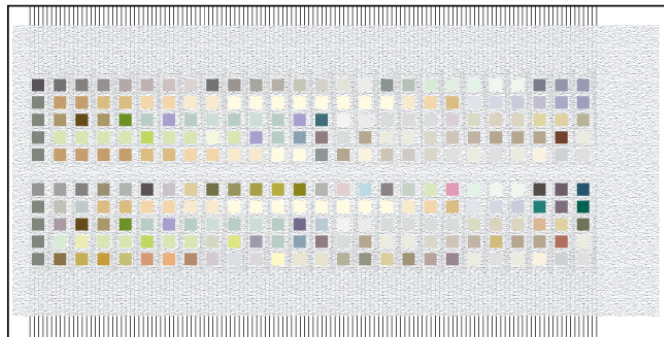
↓ STEP 3

d)



↓ STEP 4

e)



↓ STEP 5

f)

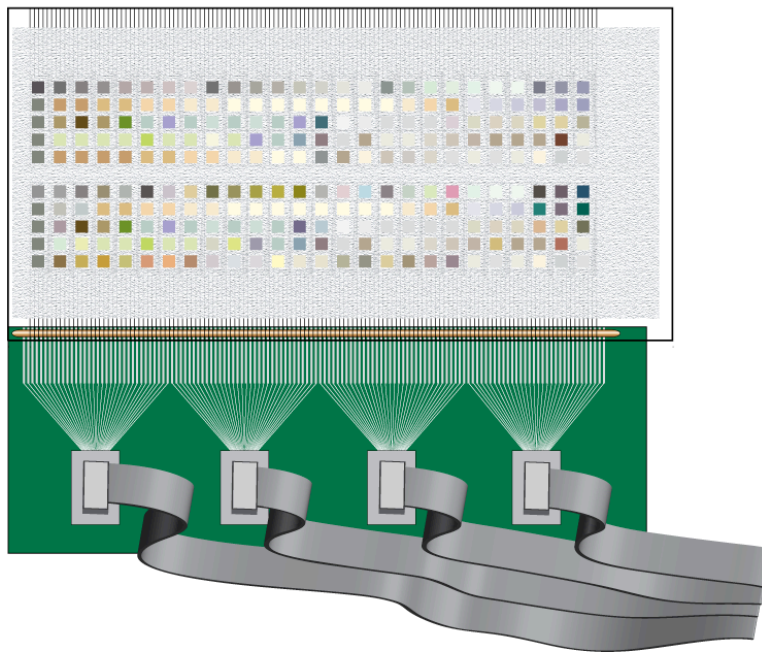


**Figure 5.4** Schematic of the process of preparing the substrate and making electrical contact to 130 individual materials on a single piece of FTO-coated glass. **a)** The substrate starts as sheet of uniformly coated FTO glass. In Step 1, it is laser etched with a spot size of 50  $\mu\text{m}$ . **b)** The etched FTO substrate, with 260 electronically isolated squares, with 130 contact pads along the two long sides of the substrate. In Step 2, the substrate is carefully cleaned and treated with siliconizing liquid for hydrophobicity and aqueous solutions of metals are printed using a commercial inkjet printer. **c)** After printing, the slide is dried at  $\sim 80\text{ }^\circ\text{C}$ . In Step 3, the substrate is baked at  $500\text{ }^\circ\text{C}$  for 3 hours and cooled overnight, pyrolyzing the metal salts. **d)** After baking, mixed metal oxides of varying coloration are generated. In Step 4, the substrate is screen printed with a screen-printable epoxy so as to passivate the surface area of the slide not covered by metal oxide spots, so as to reduce the interfacial capacitive charging as well as deleterious electron transfer reactions at the FTO-water interface. **e)** After curing the epoxy fully for maximum resistance to the 1.0 M KOH solution used in the photoelectrochemical cell, the slide is ready to be characterized. In Step 5, electrical contact is made to each of the 130 contact pads along the edge of the substrate using an elastomeric connector clamped between a custom-made PCB with corresponding contact pads. **f)** Two extra contact pads on the PCB on each end are used to ensure proper alignment of the substrate. Each contact pad on the PCB is routed to one of four ribbon cable connectors, which are subsequently connected to a second PCB (not shown).

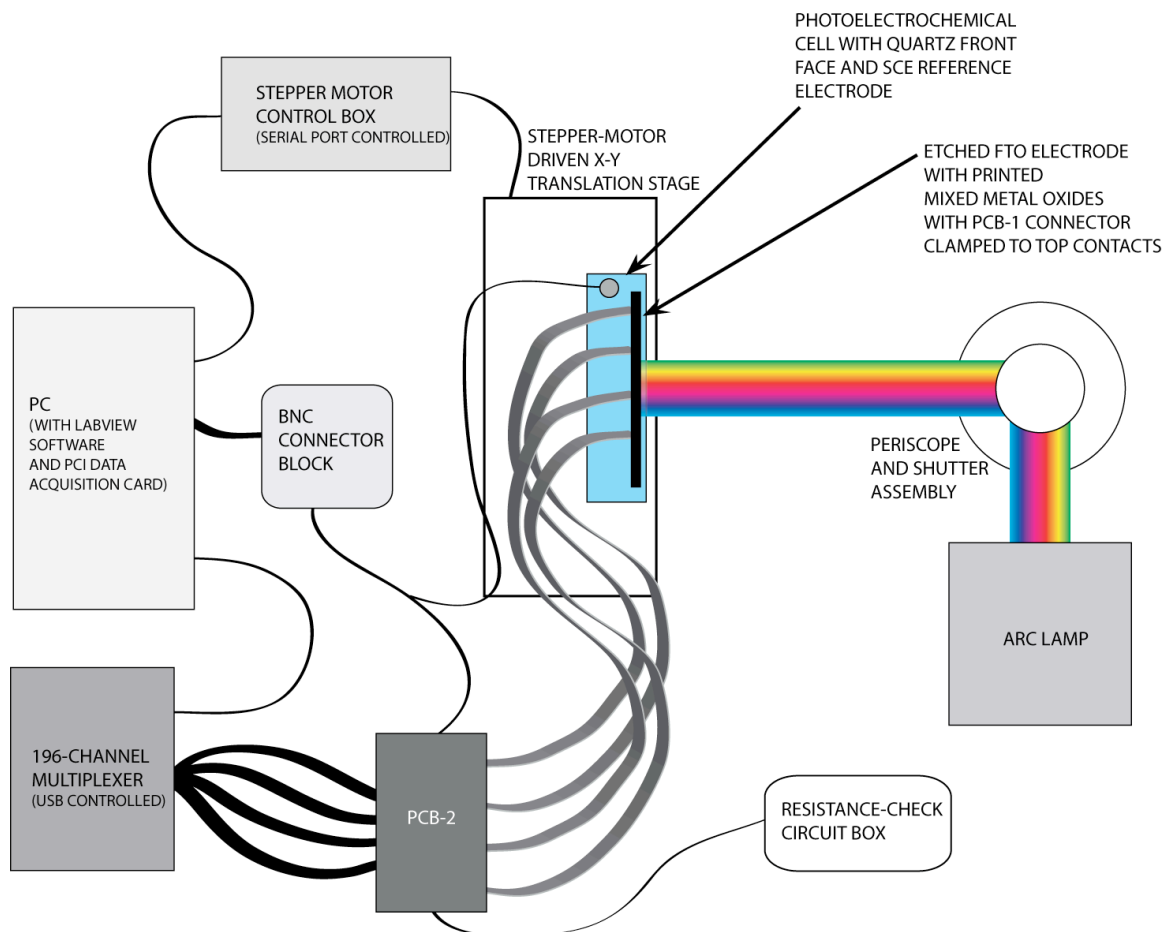
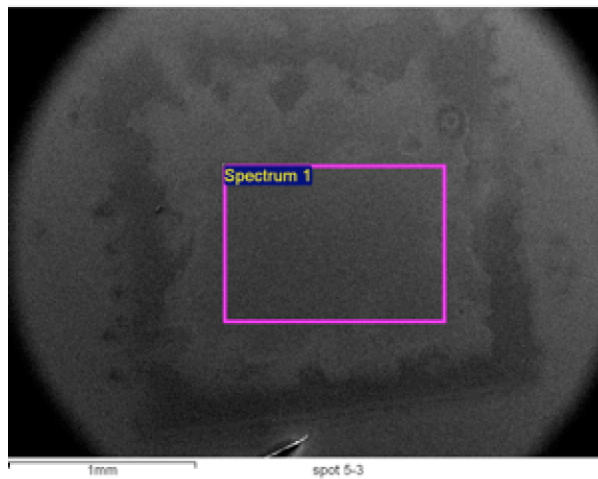


**Figure 5.5** Schematic of the experimental setup for combinatorial measurement of photovoltages of mixed metal oxides. The loosely focused output of a Xe arc lamp illuminates 10–15 printed spots at once. A motorized translation stage is used to keep the spots being measured in the region of maximum intensity as the materials on the slide are scanned from right to left. Each spot is electronically addressed individually via PCB-1, which is clamped to the etched FTO substrate. Four 34-wire ribbon cables are routed to PCB-2, which is interfaced with a computer-controlled 196-channel multiplexer.

a)



b)

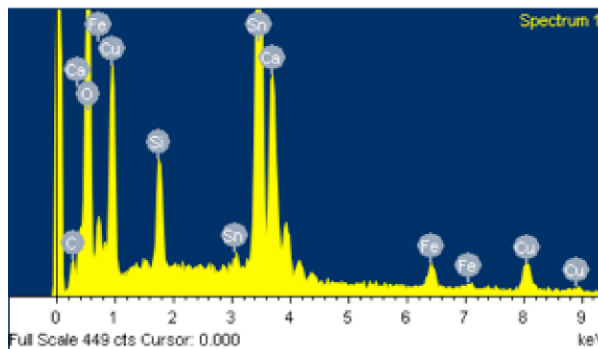


**Figure 5.6** SEM image (a) of a typical mixed metal oxide spot, and the elemental analysis results provided by the EDS analysis software. (b) The SEM image does indicate some non-uniformity and perhaps some evidence of pooling of the aqueous solution due to surface tension while drying. Elements found in the FTO glass (such as Si, O, Sn, and Ca) are observed, along with impurities such as C. The composition of this spot was nominally 30% Fe with 70% Cu (measured to be 28% Fe and 72% Cu).



**Figure 5.7** False color images of photocurrent of a slide of binary mixed metal oxides. **a)** Three-dimensional plot showing the physical position of each compound on the FTO substrate (X- and Z-coordinates correspond to the row and column of the spot) and the photocurrent measured for each. Positive values indicate a cathodic photocurrent. Column 15 and row 19 have nothing printed on them, and the bare FTO served as a control. **b)** Top-down view of the same data with the composition of each spot superimposed on a false-color image indicating its photocurrent. In this view, the materials that gave anodic currents are more clearly visible (light blue spots—in particular in rows 10–13, column 11).

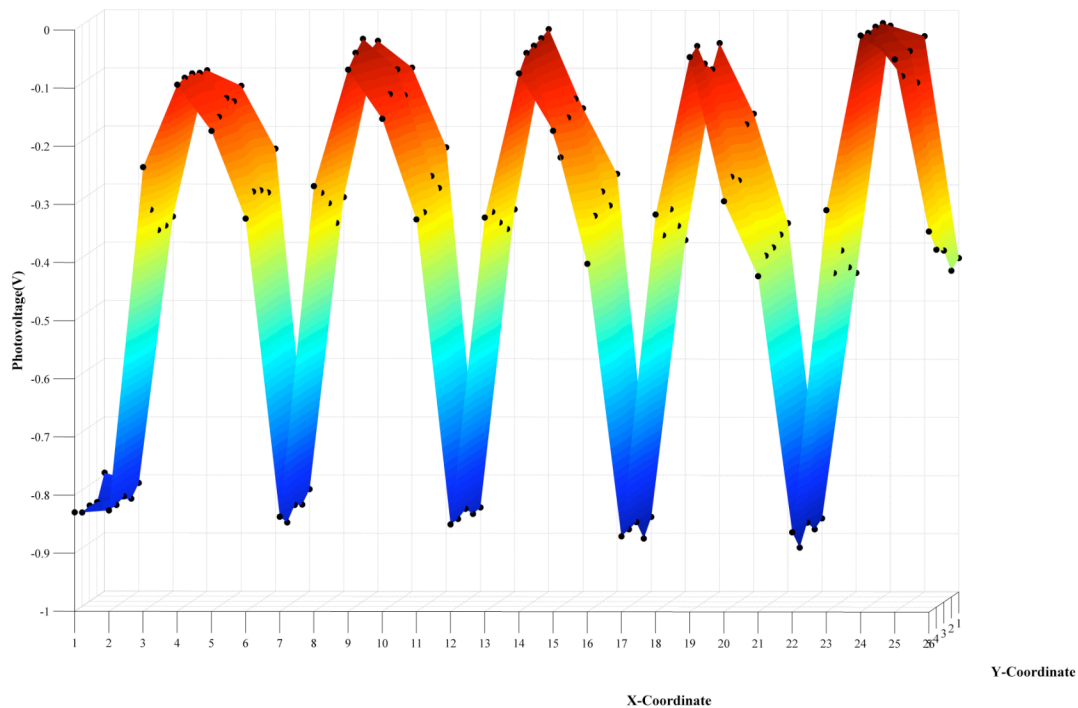


**Figure 5.8** Photovoltages for a control-sample of mixed metal oxides as a function of position on the FTO substrate. A photograph of the substrate itself is shown in Figure 5.2. A repeating pattern of five mixed-metal oxides is printed from left to right (with one extra column of  $\text{TiO}_2$  at x-coordinate equal to one), with each series of five (i.e., x-coordinates 2–6, 7–7, 12–16, etc.), the volume of aqueous metal solution inkjet printed was varied (from 30 to 62% of the maximum possible). Photovoltages were only weakly dependent the relative thickness of the printed oxide.

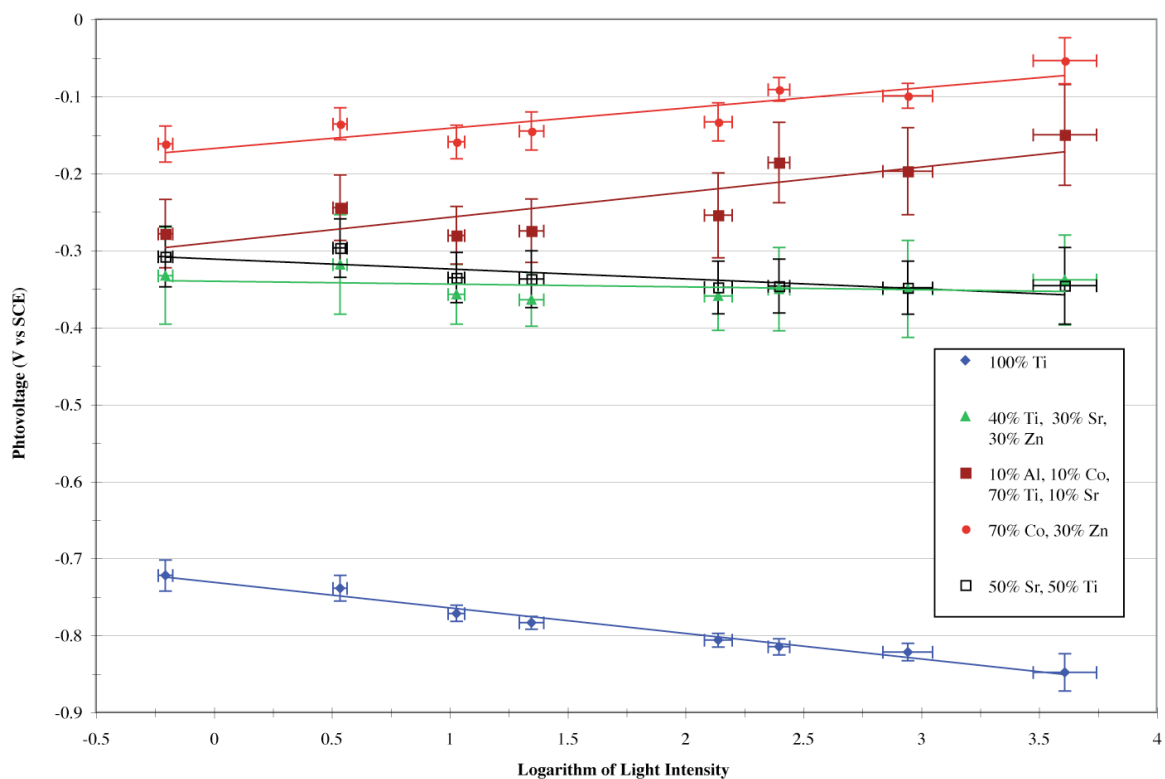


**Figure 5.9** Linear fits of the measured photovoltage vs the logarithm of the light intensity. The slope of a fit varied between the mixed-metal oxide samples tested (in mV per decade):  $-76 \pm 12$  mV for 100% Ti ( $\text{TiO}_2$ ) and  $60 \pm 11$  mV for 70% Co–30% Zn. Other materials, such as 10% Al–10% Co–10% Sr–70% Ti, 50% Sr–50% Ti, and 30% Sr–30% Zn–40% Ti, showed significant dependence on intensity. The sign of the slope indicates that  $\text{TiO}_2$  is a photoanode (as expected), whereas the combination of 70% Co–30% Zn is photocathodic.

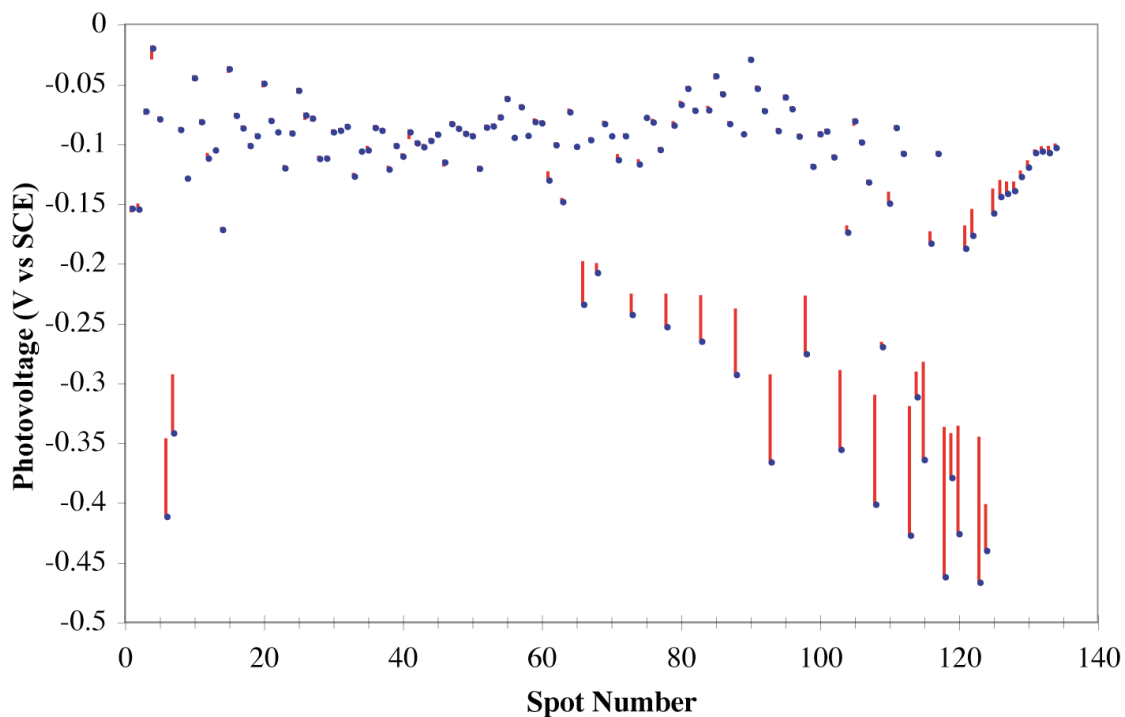


**Figure 5.10** Plot of the photovoltage for assorted binary mixed-metal oxides. The photovoltage is shown as a blue circle. The red line associated with each point represents the sign and magnitude of the slope of the decaying voltage after the light was blocked. A photoanodic material is thus indicated by a red line *above* the blue marker, as the photovoltage rises to be more positive in the dark, whereas photocathodes would have a line *below* the marker, as the voltage drops to be more negative in the dark. On this particular slide, although the large majority showed no photoactivity whatsoever, most of those that did were photoanodic. There is one material, composed of 100% copper (spot #4, top left corner), with a negative slope, indicating a photocathode, as has been reported previously for

copper oxide.<sup>17</sup> The photoanodic materials on the right-hand side of the plot, as well as spots #6 and #7 on the left, all contain zinc with varying levels of some other metal, including Sr, Ni, Cr, and Ti. Although the voltages are only moderately negative, this measurement clearly indicates that Zn leads to photoanodic behavior, which may have not been observed by only measuring the photocurrent. Also note the variation of some 150 mV observed for materials with no photoactivity.

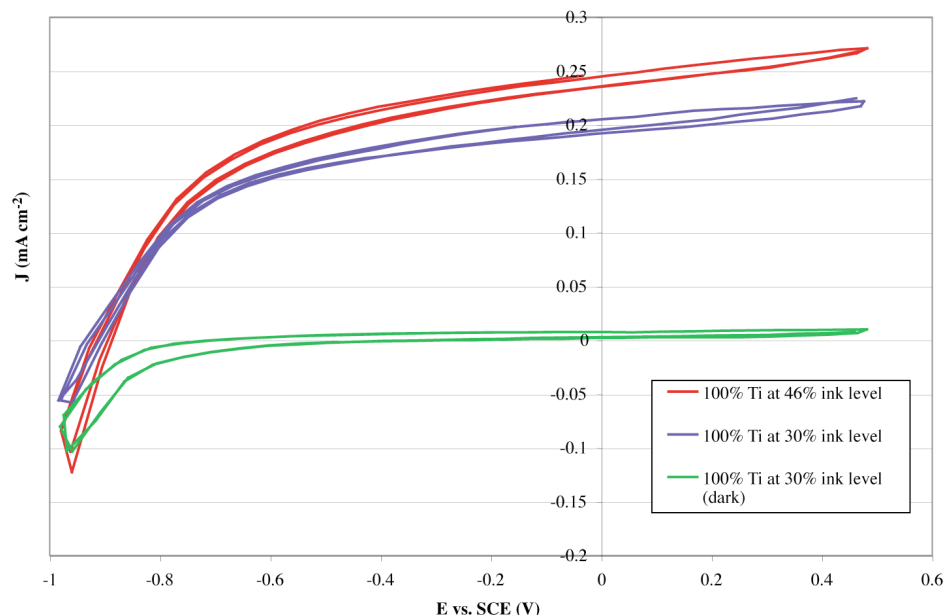


**Figure 5.11**  $J$ - $E$  Curves of inkjet printed  $\text{TiO}_2$  on an etched FTO substrate. Measured open-circuit voltages are the same within the experimental error as measured by scanning  $J$ - $E$  curves as well as open-circuit (although the  $J$ - $E$  curves show non-negligible hysteresis). These measurements illustrate the flexibility of electronically isolating each material on the substrate and also indicate that volume of solution printed does affect the measured photocurrent significantly, but that the photovoltage is relatively unchanged. This provides another example of the advantage of assessing materials based on photovoltage: while the short-circuit current is in general a linear function of illumination intensity and light-harvesting ability of the material, the photovoltage has a much less sensitive logarithmic dependence. This means that day-to-day variability in light intensity or a given material's optimal deposition thickness will have a negligible effect on the screening results.

**REFERENCES**

- (1) Fujishima, A.; Honda, K. *Nature* **1972**, *238*, 37.
- (2) Lewis, N. S. *Science* **2007**, *315*, 798.
- (3) Crabtree, G. W.; Lewis, N. S. *Phys. Today* **2007**, *60*, 37.
- (4) Lewis, N. S.; Nocera, D. G. *Proc. Natl. Acad. Sci. U. S. A.* **2006**, *103*, 15729.
- (5) Beyond Petroleum, *BP Statistical Review Historical Data*.  
<http://www.bp.com/multipleimagesection.do?categoryId=9017892&contentId=7033503>  
(7-22-07).
- (6) Department of Energy, Energy Information Administration. *Electric Power Annual 2005* **2006**.
- (7) Tan, M. X.; Laibinis, P. E.; Nguyen, S. T.; Kesselman, J. M.; Stanton, C. E.; Lewis, N. S. Principles and Applications of Semiconductor Photoelectrochemistry. In *Progress in Inorganic Chemistry, Vol 41* **1994**, 21.
- (8) Harris, L. A.; Wilson, R. H. *Annu. Rev. Mater. Sci.* **1978**, *8*, 99.
- (9) Rajeshwar, K.; Singh, P.; Dubow, J. *Electrochim. Acta* **1978**, *23*, 1117.
- (10) Bolts, J. M.; Wrighton, M. S. *J. Phys. Chem.* **1976**, *80*, 2641.
- (11) Kung, H. H.; Jarrett, H. S.; Sleight, A. W.; Ferretti, A. *J. Appl. Phys.* **1977**, *48*, 2463.
- (12) Kumar, A.; Santangelo, P. G.; Lewis, N. S. *J. Phys. Chem.* **1992**, *96*, 834.
- (13) Heller, A. *Accounts Chem. Res.* **1981**, *14*, 154.

- (14) Zou, Z. G.; Ye, J. H.; Sayama, K.; Arakawa, H. *Nature* **2001**, *414*, 625.
- (15) Webb, L. J.; Michalak, D. J.; Biteen, J. S.; Brunschwig, B. S.; Chan, A. S. Y.; Knapp, D. W.; Meyer, H. M.; Nemanick, E. J.; Traub, M. C.; Lewis, N. S. *J. Phys. Chem. B* **2006**, *110*, 23450.
- (16) Hurley, P. T.; Nemanick, E. J.; Brunschwig, B. S.; Lewis, N. S. *J. Am. Chem. Soc.* **2006**, *128*, 9990.
- (17) Woodhouse, M.; Herman, G. S.; Parkinson, B. A. *Chem. Mat.* **2005**, *17*, 4318.
- (18) Arai, T.; Konishi, Y.; Iwasaki, Y.; Sugihara, H.; Sayama, K. *J. Comb. Chem.* **2007**, *9*, 574.